Experimental visualization of the near-boundary hydrodynamics about fish-like swimming bodies

by

Alexandra Hughes Techet

S.M., Oceanographic Engineering, MIT/WHOI (1998)
B.S.E., Mechanical and Aerospace Engineering, Princeton University (1995)

Submitted to the department of
Applied Ocean Physics and Engineering, WHOI
and the
Department of Ocean Engineering, MIT
in partial fulfillment of the requirements for the degree of
DOCTOR OF PHILOSOPHY IN OCEANOGRAPHIC ENGINEERING
at the
MASSACHUSETTS INSTITUTE OF TECHNOLOGY
and the
WOODS HOLE OCEANOGRAPHIC INSTITUTION

June 2001

Author .....
Department of Ocean Engineering MIT/WHOI
May 7, 2001

Certified by. .....
Michael S. Triantafyllou
Professor, MIT
Thesis Supervisor

Certified by... .....
Wade R. McGillis
Associate Scientist, WHOI
Thesis Supervisor

Accepted by ....
Michael S. Triantafyllou
Chairman, Joint Committee for Oceanographic Engineering
MIT/WHOI

Experimental visualization of the near-boundary hydrodynamics about fish-like swimming bodies

by

Alexandra Hughes Techet

Submitted to the department of
Applied Ocean Physics and Engineering, WHOI
and the
Department of Ocean Engineering, MIT
on May 7, 2001, in partial fulfillment of the
requirements for the degree of
DOCTOR OF PHILOSOPHY IN OCEANOGRAPHIC ENGINEERING

Abstract

This thesis takes a look at the near boundary flow about fish-like swimming bodies. Experiments were performed up to Reynolds number 10^6 using laser Doppler velocimetry and particle imaging techniques. The turbulence in the boundary layer of a waving mat and swimming robotic fish were investigated. How the undulating motion of the boundary controls both the turbulence production and the boundary layer development is of great interest.

Unsteady motions have been shown effective in controlling flow. Tokumaru and Dimotakis (1991) demonstrated the control of vortex shedding, and thus the drag on a bluff body, through rotary oscillation of the body at certain frequencies. Similar results of flow control have been seen in fish-like swimming motions. Taneda and Tomonari (1974) illustrated that, for phase speeds greater than free stream velocity, traveling wave motion of a boundary tends to retard separation and reduce near-wall turbulence.

In order to perform experiments on a two-dimensional waving plate, an apparatus was designed to be used in the MIT Propeller tunnel, a recirculating water tunnel. It is an eight-link piston driven mechanism that is attached to a neoprene mat in order to create a traveling wave motion down the mat. A correlation between this problem and that of a swimming fish is addressed herein, using visualization results obtained from a study of the MIT RoboTuna. The study of the MIT RoboTuna and a two-dimensional representation of the backbone of the robotic swimming fish was performed to further asses the implications of such motion on drag reduction. PIV experiments with the MIT RoboTuna indicate a laminarisation of the near boundary

flow for swimming cases compared with non-swimming cases along the robot body. Laser Doppler Velocimetry (LDV) and PIV experiments were performed. LDV results show the reduction of turbulence intensity, near the waving boundary, for increasing phase speed up to 1.2 m/s after which the intensities begin to increase again through $C_p = 2.0$ where numerical simulations by Zhang (2000) showed separation reappearing on the back of the crests. Velocity profiles who an acceleration of the fluid beyond the inflow speed at the crest region increases with increased phase speed and no separation was present in the trough for the moving wall. The experimental techniques used are also discussed as they are applied in these experiments.

Thesis Supervisor: Michael S. Triantafyllou
Title: Professor, MIT

Thesis Supervisor: Wade R. McGillis
Title: Associate Scientist, WHOI

Acknowledgments

Throughout my adventures at MIT I have been fortunate to have been supported generously by several outside agencies. First was the support of the Office of Naval Research in the form of the NDSEG Fellowship. This support was pivotal in allowing me the experimental freedom to pursue my research interests from the beginning. The Link Foundation's fellowship in Ocean Engineering and Instrumentation supported me for the second to final year of work and for that I am grateful.

Regardless of funding I would not have had these exciting opportunities were it not for my advisor, Professor Michael Triantafyllou. His support and guidance over the last six years have been invaluable. I would also like to extend my thanks to the other members of my thesis committee: Prof. Dick Yue and Dr. Franz Hover of MIT, Dr. Wade McGillis from WHOI, and Prof. George Karniadakis from Brown Univ., for all their time and constructive suggestions.

The MIT/WHOI joint program offers many exciting opportunities to students and I am glad to have had the opportunity to participate in the program. Through WHOI Joint Program support and the Abkowitz International fellowships I have had the good fortune of traveling to conferences in fun places: Brest, France; San Francisco, CA; Santa Barbara, CA and Washington DC. Through these opportunities I have mad many valuable contacts and learned much about current research in fluid mechanics.

Without facilities and equipment I would have no data. Thus I would be remiss for not thanking Prof. Jake Kerwin for allowing me the use of the Propeller Tunnel. Dr. Todd Taylor and Randy Fairman for all their helpful suggestions and occasional man-power. In addition, Dan Sura and the other UROPS along the way, especially Karl McLetchie, Jonah Elgart, Jeff LeBlanc, and Malima Wolf who at some point inevitably had to fix something I broke. I would also like to thank the Towtank staff, past and present for all their helpful suggestions and for attempting to expand my musical horizons – I do not miss Slayer hour.

In addition there are several people who have been there through it all. Six years

ago when I started there were about 30 of us in 13.021 – today as few as three of us still remain. To Kelli Hendrickson, thank you for all the good advice and friendship – I could not find a better officemate. To Rich Kimball, well lets just say I wouldn't have made it this far without your knowledge of the Prop. Tunnel. I appreciate the time and effort Rich donated to help me set-up the waving plate. As for others who started with us but have long since graduated, Britt and Jaye thank you for all of your support and friendship and best of luck with your new family.

Many thanks go to Sean McKenna for his most excellent PIV code and our many fruitful discussions about the nuances of data processing, but most especially for his friendship throughout. I owe much of my continued sanity to my brother Andrew who revives my social life every now and then when I forget to play. I will miss him when he moves back south. Lastly I thank my parents for being so supportive through the years – this adventure was only possible as a result of the foundations you helped me build.

Contents

List of Figures

Chapter 1

Introduction

This thesis takes an experimental look at the relationship between a fish-like swimming boundary and the surrounding flow. The undulating motion, similar to the backbone undulation of swimming fish, is an increasing amplitude traveling sinusoid wave. The objective of this work is to elucidate the hydrodynamic features of the near boundary flow over fish-like swimming bodies using laser Doppler velocimetry (LDV) and particle image velocimetry (PIV). How the undulating motion of the boundary affects the near body turbulence production is of great interest. The main focus of the thesis is the near boundary flow about a two-dimensional waving mat in a recirculating water tunnel. A correlation between this problem and that of a swimming fish is also addressed, using visualization results obtained from a study of the MIT *RoboTuna* in a towing tank.

Data from the robotic fish and waving plate shows turbulence reduction caused by fish-like swimming motion. In the RoboTuna, velocity profiles for non-swimming case have the characteristic shape of a turbulent profile; but for the swimming case

have largely laminarized. Laser Doppler velocimetry and particle image velocimetry on the waving plate show similar results at Reynolds numbers up to 10^6. The waving plate apparatus, designed, constructed and tested, allows the exploration of higher speeds to assess Reynolds number effects.

1.1 Motivation

Over millions of years, aquatic creatures have evolved to optimize their propulsive mechanisms in order to survive in their specific environments. Fish, especially, seem to have perfected swimming, maneuvering and accelerating and are capable of propelling themselves over great distances quickly and gracefully, without apparent fatigue. The physics behind their seemingly effortless, efficient motion is not quite clear, leading researchers to study the swimming and maneuvering of fish. In order to do so, scientists have moved to study the muscles ([25], [26]), the fluid dynamics of live swimming fish [8] and more recently scientists have captured these movements in robotic machines such as the MIT *RoboTuna* developed by [11]. A good review of current research into fish swimming is given by [55].

To better understand the impressive swimming ability of these live and man-made creatures, the fish-fluid interactions need to be investigated further. Previously researchers have shown the ability of the caudal fin of a fish to produce a jet-like wake similar to that of a flapping foil (figure 1-1). However this phenomenon does not completely explain the high propulsive efficiencies of the swimming fish.

Like the fish body motion, a wave traveling down a flat plate produces an un-

Figure 1-1: Dye visualization of the MIT *RoboTuna*wake showing a reverse Kármán wake pattern. (from [53])

dulating motion that will affect the fluid near the plate boundary and also the vortex shedding mechanisms. The evolution of turbulence is especially interesting as such boundary motion has been shown to result in suppression of turbulent structures [65, 48] and separation. The swimming plate offers a controlled experimental setting to further study the effects of an undulating motion on a boundary layer and the opportunity to draw a parallel with the hydrodynamics of swimming fish.

Taneda and Tomonari investigated the flow around a flexible waving mat, revealing a unique effect as the wave phase speed increased beyond the free stream velocity [48]. It was observed that the flow began to relaminarize at the crests, and then eventually over the entire mat (troughs and crests), as the phase speed approached and then exceeded the velocity of the free stream. Their efforts did not exceed a Reynolds numbers up to $7x10^5$ in air. This thesis looks to extend these ideas to higher Reynolds numbers on the order of 10^6 in water. The waving plate problem is an interesting parallel to the swimming fish, since the backbone motion of several fish species is essentially that of a traveling wave.

Experimental results revealing the swimming hydrodynamics of live fish can be

difficult to obtain in laboratory environments. As a result, Barrett constructed a robotic underwater flexible hull vehicle in the shape of a tuna with a lunate tail capable of swimming in a straight line on a towing carriage, and on which drag force and energy analysis could be performed [11]. It was shown experimentally that over narrow ranges of various swimming parameters, the robot could achieve extremely high efficiencies, seemingly higher than those of conventional marine propulsors, and in addition, could experience lower drag than a rigid-body hull [12].

Over the past two decades, improved flow visualization techniques have aided investigations into the swimming of live fish. Anderson studied the Giant Danio in a still water tank using DPIV and high speed camera imaging in Kalliroscopic fluid [8]. These studies yielded valuable information into the wake features of the fish, but due to the processing techniques and equipment used, offered little information on the boundary layer features of the swimming fish. Advances in technologies now allow us a closer look at what is going on.

To further investigate this analogy a detailed look at the flow very near the boundary of the *RoboTuna* is performed through digital particle image velocimetry (DPIV) at the MIT Towing Tank facility. Tests on the *RoboTuna* are performed in the MIT Towing Tank which is 30 meters in length, 2.4 meters wide and on average 1.3 meters deep. This tank houses two separate carriage systems: one of which controls the *RoboTuna.* The swimming case, targeted specifically, coincides with Barrett's power measurement findings of best "self-propelled" swimming. The parameters for this case are deemed to be the "best" by a genetic algorithm also discussed in Barrett's thesis [12]. Through DPIV and particle tracking, the flow in the boundary layer, into

the equilibrium range of scales, can be resolved.

Tests on the waving plate are performed in the MIT Propeller Tunnel which has a cross section of 20 in. x 20 in. and a test section 44 in. long. Flow speed is variable up to 6 m/s. The waving plate mechanism, designed specifically for these experiments, is discussed in detail in chapter 5. A CAD representation of the waving plate assembled in the hydrodynamics tunnel is seen in figure 1-2. Flow visualization of the boundary layer around the swimming plate is performed at various Reynolds numbers up to 10^6 using both Laser Doppler Velocimetry (LDV) and Particle Image Velocimetry (PIV).

1.2 Chapter Preview

This thesis will discuss the basic theories of hydrodynamics relative to this problem as well as a discussion of the experimental techniques and design tasks involved with gathering and processing the requisite data. Each chapter focuses on a specific subset of knowledge.

Chapter 2 includes background on the two problems to be discussed within. First an overview of research directed at fish swimming and robotic biomimetics and second, a review of both boundary layer theory and flow control mechanisms. Next, chapter 3 will introduce the experimental methods use to acquire the flow field data. Particle image velocimetry is introduced and discussed briefly with comparisons to alternate techniques. The implementation of PIV for the purpose of this study is discussed at length. Both experimental setups, for the *RoboTuna* and the waving

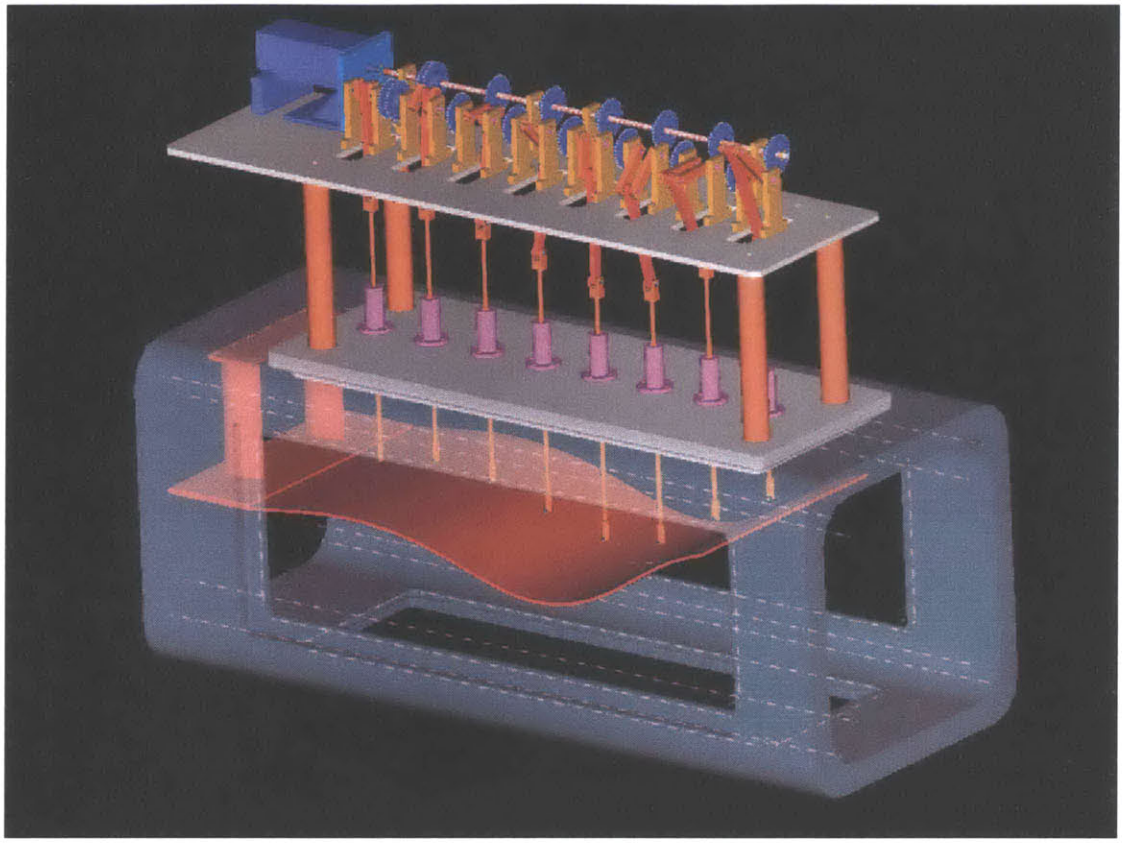

Figure 1-2: Three-dimensional rendering of the waving plate design. The mechanism to move the mat is located on top of the tunnel section with the eight pistons entering the test setion throught the top window. The mat is shown through the tunnel section. Flow is from left to right.

plate PIV tests are described in their respective chapters, 4 and 7. Chapter 4 will present the experimental results from the *RoboTuna*. The experimental setup and *RoboTuna* mechanism are discussed briefly. Near body PIV of the *RoboTuna* is discussed for the swimming parameters investigated.

The waving plate apparatus is discussed from a design point of view in chapter 5; the operating parameters and physical specifications are outlined. Detailed photographs aid the reader in visualizing the complex setup of the apparatus within the Propeller Tunnel. Chapter 6 discusses the Laser Doppler Velocimetry results

and chapter 7 introduces the results from the waving plate DPIV experiments. The similarities between the case for the robotic swimming fish and the waving mat are discussed. The implication of increasing wave (phase) speed with relation to the free-stream mean flow is investigated. Comparisons of the experimental data to direct numerical simulations [65] and the works of Taneda and Tomonari [48] and Kendall [29] are also presented.

Discussions of future applications and further areas of study are presented in chapter 8. Chapter 9 concludes with a summary of the findings and contributions of the thesis.

Chapter 2

Flow Control Through Unsteady Motion

Flow control is a rich subject that has direct implications for the problem of fish-swimming and underwater vehicle propulsion. Especially of interest to scientists is flow control for the purpose of drag reduction and vehicle propulsion. Experiments with both passive and active control devices have been performed to determine their effects on drag reduction, and alternate propulsion mechanisms have been designed which employ unsteady moving, "flapping" foils instead of propellers to manipulate what would otherwise be drag wakes into jet wakes for vehicle propulsion.

This chapter presents some of the previous research on vorticity control and progresses into work on flow control near solid boundaries. It serves as an introduction to the research on swimming bodies under investigation in this thesis.

2.1 Vorticity Control

Vorticity control has been found to be a very effective means to control the overall flow. As reviewed in Rockwell [42] and Triantafyllou *et al.* [55], applications include rotating bluff bodies, unsteadily moving airfoils, unsteady forcing of the flow with discrete or distributed actuators to enhance viscous mixing, as well as flexible surface vehicles.

Experimental and simulation results demonstrate the ability of flexible-hull vehicles to achieve high maneuverability and turbulence reduction through flow control [64], [65]. The formation and manipulation of body-generated vorticity requires careful motion control. The form and structure of the body actuators, as well as the low-level and high-level control methodology, are paramount to effective flow control. Completed work on identifying the principal flow control patterns, as well as on-going work studying how these patterns could be detected through body-based pressure transducers, and the use of closed loop feedback is outlined below.

Body flexing, such as the swimming motion of a fish body, causes under proper conditions turbulence reduction. Numerical data, experimental data on the MIT robotic mechanism and data from live fish confirm the reduction in turbulence intensity in the boundary layer of actively swimming bodies. Numerical simulations also show the ability of a two-dimensional undulating boundary to reduce turbulence [65].

Through flow control over the entire vehicle by the appropriate body motion, flexible-hull vehicles achieve substantially improved fast-starting and maneuvering as compared with rigid hull bodies. Observations from live fish, recording high transient

performance, reinforce this reasoning.

The complexity of control, both open-loop and closed-loop, may be considerable, since effective control might require that several actuators must be controlled simultaneously. Thus the identification of the basic principles behind the mechanisms responsible for the efficient formation of large transient forces, and for avoiding the formation of separation wakes, is paramount for effective control.

Since potential flow in the absence of separation and shear layer shedding is a reversible process, one naturally must focus on the generation and control of vorticity as the prime mechanism for maneuvering. Inviscid formulations which account properly for the shedding of vorticity have been found to be very close to experimentally obtained results on the formation of large-scale vortices in unsteadily oscillating bodies [63]. Direct numerical simulations (DNS) are preferable since they allow the study of viscosity-dominated phenomena as well, such as the axial drag on streamlined bodies; the well-known difficulties with high Reynolds number simulation, necessitate the use of either inviscid methods with proper shedding formulation, or the use of another method, Large-eddy simulation (LES). DNS calculations of fish-like swimming up to Reynolds number of about 10,000 have produced high quality flow data ([34], [30]). Experiments with flexible-hull vessels and direct flow measurements on live fish are a reliable way to obtain data on maneuvering flexible bodies and to corroborate analytical predictions.

In the last sixty years an attempt to quantify the assumptions about swimming fish performance has been made, both through experimental observations and measurements and detailed approximate analytic or numerical methods. Yet, the physics

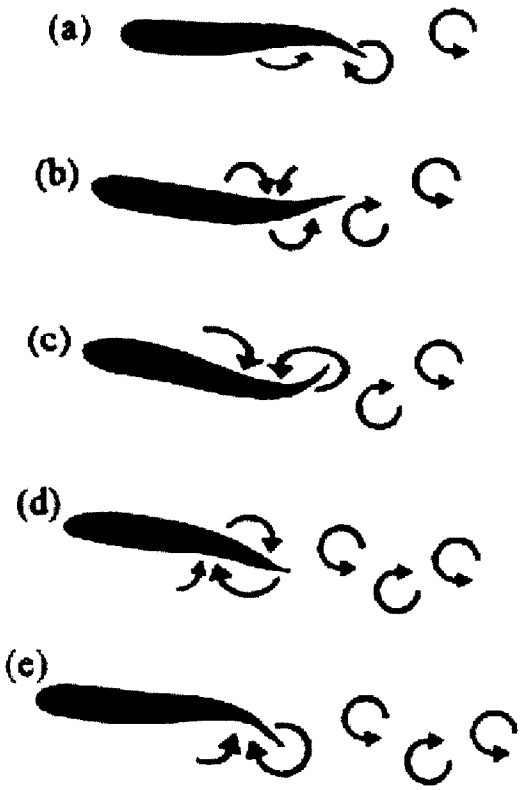

Figure 2-1: Vorticity manipulation by a straight-swimming fish from [8]. The alternately signed vortices form a jet wake which propels the fish through the water.

behind why fish are able to achieve such high efficiency, speed, and maneuverability remains a mystery. As a fish tail oscillates, it produces a thrust jet by the repositioning of shed vorticity into an unsteady staggered array which resembles a reverse Kármán vortex street. Figure 2-1 shows the stages of vorticity shedding in straight swimming fish from [8].

Fish can use this thrust generation to control their movements to swim straight, accelerate and maneuver quickly. The flow about a fish is manipulated through the body motion as well as the tail motion. The effect of the traveling wave motion of the fish backbone warrants investigation separate from studies of flapping foil motion.

Understanding of flow control and boundary layer concepts is crucial to beginning this journey. With enhanced studies of the contribution of the various components of fish swimming, the design of surface and underwater vessels, AUV's, and maneuvering control can be improved upon. Modelling devices after evolved biological creatures is the foundation of a growing area of engineering known as *biomimetics.*

The study of live fish swimming can be very instructive in exploring mechanisms of unsteady flow control since fish have evolved over millions of years to optimize their locomotive abilities. A good survey of fish observations and theories of fish swimming and turning can be found in Weihs [60], Lighthill [33] and Videler [58]. Domenici & Blake [18] review the literature on observed fast-starting kinematics of live fish, reporting for fast fish, such as the pike (*Esox lucius*), maximum accelerations in excess of 150 m/s^2. The body of the maneuvering fish is bent into either a C-shape or an S-shape and then rapidly unwound in a traveling wave fashion.

Experimental studies have shown the importance of vorticity control in fast-starting and maneuvering. Ahlborn *et al* [5], [4] study the double flip motion of an unsteadily moving fin, simulating the motion of the tail of a fish. The double flip consists of motion to one side, causing the shedding of a vortex, followed by a reverse-direction motion, shedding a vortex of the opposite sign. The two vortices join to form a pair of thrust-producing vortices. The lag between the formation of the two vortices is a prime parameter, because it controls the growth of the thrust-producing eddies.

In a series of publications, Anderson [8], Triantafyllou *et al.* [52], and Wolfgang *et al.* [63] show experimental and simulation results of the flow around a maneu-

vering Giant Danio and compare them to numerical predictions. Figure 2-2 shows results from flow visualization simulations around a live Giant Danio performing a C-maneuver (from [63]).

At the beginning of the turning maneuver, as the formation of a "C" shape is complete, the flow around the fish organizes into two almost circular flow features, one centered near the tail and one near the head (see figure 2-3 for an illustration). These two flow features can be described as two body-bound vortices of opposite sign. The three-dimensional structure of these bound vortices shows a remarkable persistence over a major part of the body height, despite the low-aspect ratio form of the body. The obvious need for vortex connectivity induces strong three-dimensionality only at the extremes of the body depth.

The ultimate result of the C-shape maneuver is a vortex pair, forming a local jet flow. The direction of the jet is as expected from momentum principles to affect a turn. The generation of the vortex pair is due to a great extent to the body motion and flexing. The tail fin plays a significant role in repositioning the body formed vorticity, through its suction force and the generation of additional trailing edge vorticity. Timing of tail and body motion is crucial to coordinate the process of vortex formation and to avoid uncontrolled vortex formation and separation flow. The process of rapid generation of a strong vortex pair through combination of body flexing and tail manipulation, and the absence of separation drag help to explain the outstanding agility of fish.

While the undulating motion of a swimming fish causes unsteady flow around the body, Ffowcs-Williams & Zhao [20] and Tokomaru & Dimotakis [50] also have shown

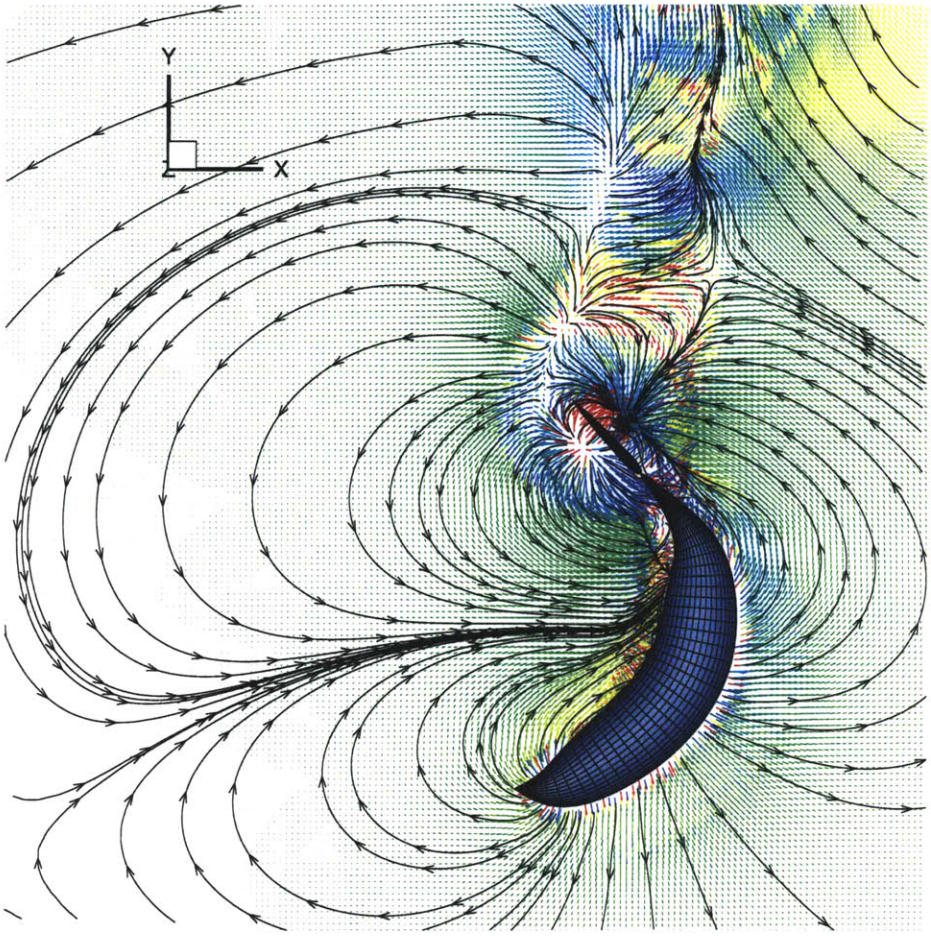

Figure 2-2: Motion of a giant Danio during a typical turning maneuver. The figure is a numerical prediction of the maneuver from [63].

that is possible to obtain efficient flow control through the unsteady motion of a body in fluid. Unsteady motion of airfoils can produce propulsive thrust efficiently ([52] and [9]) and can recapture energy contained in the eddies of an oncoming flow using vorticity control [23].

Rotary oscillating cylinders are another prime example of flow control through unsteady motion. Work by Tokumaru and Dimotakis [50] and also Taneda and Tomonari [47] has shown that an oscillatory rotation applied to a circular cylinder at certain frequencies can lead to a significantly reduced drag wake and even supress

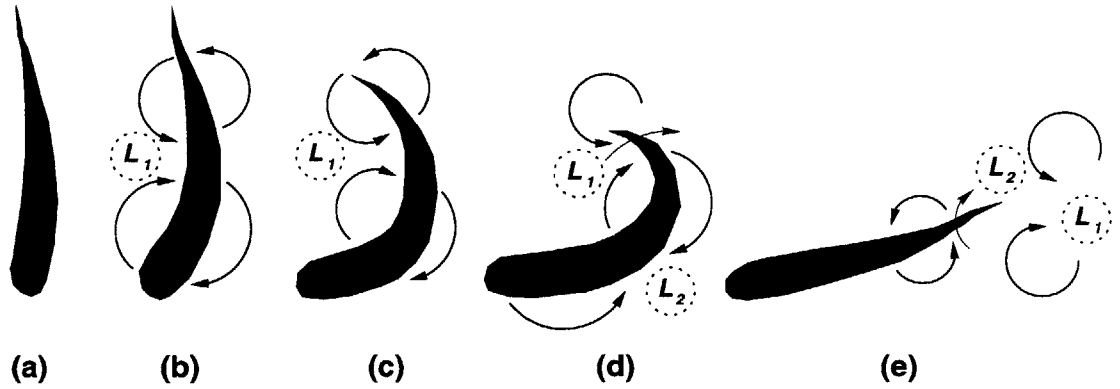

Figure 2-3: The vorticiy patterns throughout a C-maneuver from start (at left) to finish (right) as deduced through PIV and numerical simulations.

vortex shedding all together. Figure 2-4 shows the drastic reduction in drag coefficient as the rotary frequency increases. Figure 2-5 shows dye visualization of the flow past a rotary oscillating cylinder done by [50]. In the top image is a typical Kármán wake, with the vortices spaced much further apart than those in the lower image where the cylinder is rotating. In the rotating case the frequency of rotation effects the shedding frequency and also decreases the drag coefficient significantly.

In a similar unsteady problem of circular jet flow formation through a piston, Gharib *et al* [21]and Rosenfeld *et al* [43] found that the leading vortex ring has reached its maximum circulation when the non-dimensional "formation time" is around 4. The formation time is equal to Ut/D, where U is the mean speed of the piston, t the time of formation and D the diameter of the ring. There is also strong similarity with the Strouhal number of jets produced by oscillating foils, where vortical dynamics in the wake are optimal when $fA/U \approx 0.30$, where f, A, and U are respectively the frequency of foil oscillation, the trailing edge transverse excursion of the foil, and the forward speed of the foil [54], [51].

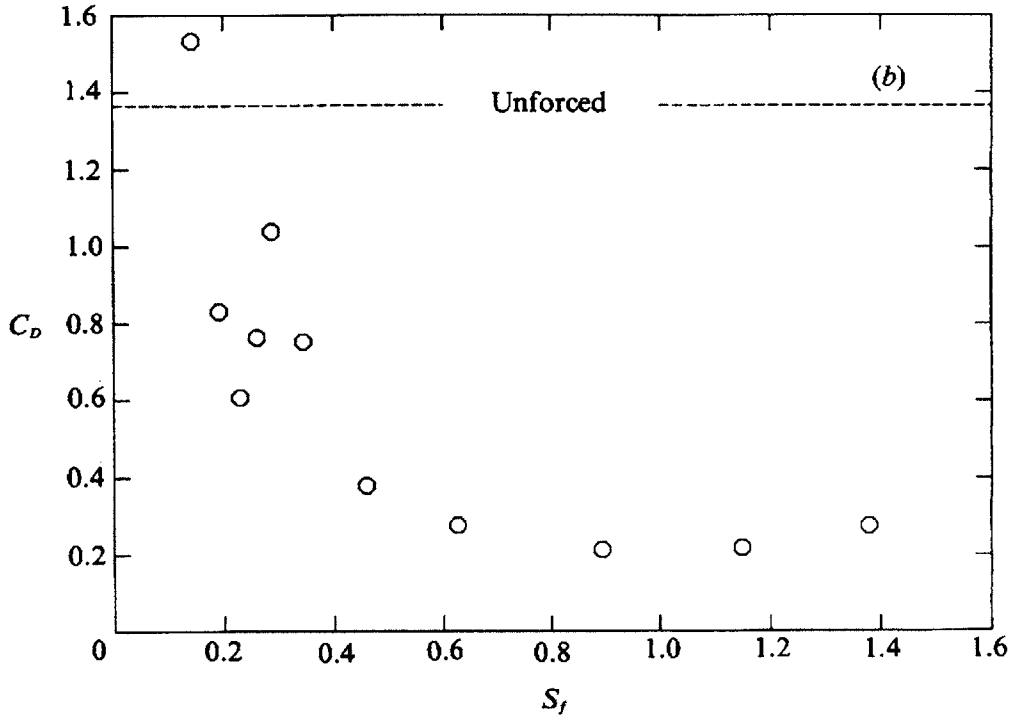

Figure 2-4: Drag coefficient for the rotary oscillating cylinder. The drag is reduced significantly from the unforced value around $C_D = 1.4$. Taken from [50]

The principles of rapid maneuvering have been implemented in biomimetically designed flexible vehicles [31]. The principal goal is to execute, with the minimum possible complexity, the required flexing to achieve super-maneuverability. The implementation of surface-mounted pressure transducers is an important step in achieving real-time closed-loop feedback control, which is essential when external flow disturbances interfere with the vorticity control required for rapid turning. Vortices can be identified and tracked through multiple pressure measurements, due to their unique signature consisting of a substantial bell-shaped pressure drop.

In all, the idea of using unsteady motion to manipulate flow about a body in order to produce thrust or reduce drag is exciting. In the case of the swimming fish, the

exact source of the high swimming efficiencies have been debated (see discussion in [7]). While it is clear that the undulating body motion combined with the tail fin acts to produce the thrust jet to propel a fish forward, it is not yet clear exactly how the body motion effects the flow very near a fish or a traveling wave wall. Does this swimming motion reduce friction drag or turbulence production in a effort to further aid the swimming process? Or is it another mechanism all together?

The next section focuses on the effects of these motions on near boundary flow including a discussion of the basics of flow over boundaries, including flat-plate boundary layer theory which is useful for comparison and further discussion.

2.2 Near Boundary Flow control

Flow control for thrust production and drag wake reduction has been discussed, but what are the implications of these unseatdy motions on the near boundary flow. Near boundary flow has been of great interest to scientists for many years. Attempts to control boundary layer growth and to relaminarize turbulent boundary layers have been done using a myriad of techniques. From blowing and suction (adding and subtracting momentum from the boundary layer) to electro-magnetic control to passive riblets, there has been a lot of effort invested into controlling near boundary flow and reducing skin friction drag. An in-depth review of both passive and active control techniques, which have been investigated for use in skin friction reduction, if given by [17].

The idea that unsteady body motions could also result in the manipulation of very

near body flow finds a prime example in the case of the undulating body boundary, similar in motion to the swimming fish body motion. Taneda and Tomonari [48] performed an experimental investigation into the effects of swimming motion on the boundary layer in both a wind tunnel and water tunnel. Here they implemented a swimming mat in lieu of a fish. The waving plate studied was a rubber mat supported on ribs and driven by multiple cams on a common camshaft. By altering the size of the cams along the span and driving them with a common camshaft, a traveling wave of variable amplitude was sent down the length of the mat. Visualization studies were performed using electrolytic precipitation methods and aluminum flake techniques. Also data was obtained from hot-wire anemometers and pressure transducers showing turbulence intermittency for cases of the waving plate with phase speed greater than free stream.

In their studies, Taneda and Tomonari noted that when the wave speed, C_p, is smaller than the uniform inflow, U_o, the boundary layer separates at the back of the final crest and the separated vortices are transported backwards with speed C_p(see Figure 2-6); whereas for C_p larger than U_o, the boundary layer separation does not occur over the entire span of the rubber mat. Through velocity and wall stress measurements, it was shown that the swimming motion accelerates the fluid in the direction of the wave and the mean velocity increases with wave velocity. Taneda and Tomonari observe turbulence intermittancy and boundary layer laminarization, reducing wall stress reduce when the mat underwent swimming motions.

In numerical simulations of periodic traveling waves, Zhang [65] showed that the mean velocity profiles show an increase in energy with increased wave speed with the

mean profile fuller for higher C_p/U_o. He also showed that, for higher C_p/U_o, turbulence intensities are highest near wall whereas for lower C_p/U_othey are greater away from wall. These experimental and numerical results have interesting implications for the problem of fish swimming as the body motion is that of a traveling wave for some swimming species.

This unsteady traveling wave motion of the body creates alternating boundary curvature along the body length. The introduction of curvature, convex or concave, has been shown to significantly alter flow characteristics from that of flow over a flat plate. There has been considerable work done to investigate the flow over convex surfaces, some research into concave surfaces, and investigations into non-moving rippled beds.

Next we will look at work related to stationary sections of wall curvature as a foundation for future discussion. Some of the first discussions on this topic date back to 1930 by Prandtl. Much of the work has focused on flow over convex curvature, though several experiments give insight into the flow over concave curvature as well.

In general, the normal momentum exchange over convex surfaces is suppressed by normal pressure gradients which are generated by the centrifugal force. Measurements of turbulent boundary layers by [46] for flow over convex surfaces indicated that the Reynolds stress was decreased, and disappears in the outer half of the boundary layer, for a convex wall.

Gillis and Johnson [22] and Alving *et al.* [6] observed a reduction in turbulent mixing length in the presence of surface curvature. The turbulent shear stress in the outer layer decreased to nearly zero and an 'active' shear stress internal layer was

formed. Gillis and Johnson report that the stabilizing effects of a convex curvature act to significantly reduce the turbulence length scales and to lessen the effects of upstream conditions on the flow after the section of curvature. Once reduced the flow regenerates very slowly. At some point through the convex bend the flow profile tends to laminar or transitional whereas it is previously turbulent in shape. The active shear layer becomes smaller than δ. Baskaran *et al.* observed that the vertical intensity ($\overline{v'^2}$) decreased more rapidly than streamwise turbulence intensity [15] .

Research into simple concave curvature effects is less prolific than that for convex curvature, however several revealing experiments have been performed. In one such study, Görtler [24] observed a series of alternating rolling structures for certain cases of flow over concave surfaces [24]. These roller structures are most often associated with rotating fluids and the class of Taylor-Görtler instabilities.

In the case of the traveling wavy wall problem, classic flat plate turbulent boundary layer theory (discussed in the next section) can no longer be applied for large C_p/U_o since we cannot assume that the surface tangential pressure gradient can be found from the far field velocity. Neither is it valid to apply the assumptions that the pressure is constant across the boundary layer. For large phase speed and wave slopes, the normal pressure gradient is large near the wave crest and troughs.

For stationary curvature, non-moving walls, flow over a convex curvature is stable whereas flow over a concave surface is not. Thus it is not hard to imagine that the turbulence intensity would increase where concave curvature is present and decrease in the presence of a convex surface. For the problem of the waving mat, the surface is no longer static and it becomes much simpler to look at this from a moving reference

frame as if the surface is sliding out from under the observer.

In this moving reference frame, the sliding velocity of the mat is represented by V_m and the velocity of the fluid a small distance, δ, away from the mat is V_δ. For the waving plate problem this sliding speed is the phase speed of the traveling wave. The stability criterion change from the static case. For large phase speeds the centrifugal force, proportional to the square of the velocity along a streamline divided by the radius of mat curvature, is quite large in comparison to the case with static curvature.

Referring to the above discussion of Taylor-Görtler vortices, we can look at these stability criterion for our sliding surface. Figure 2-7 illustrates the Taylor-Görtler stability criteria for the sliding boundary where curvature, both convex and concave, is present. On the left you see flow over the convex surface and at right the concave surface. For the convex case we have stability when $V_\delta > V_m$ and instability for $V_\delta < V_m$; for concave curvature this is reversed.

While [46] found these vortices in their experiments of flow over concave curvature, [14] found no sign of Taylor Görtler vortices in their convex flow conditions. [40] and [27] also performed experiments on convex and concave surface curvature noting that the influence of concave curvature is distinct from the effects of convex curvature, and that flow responds more rapidly to convex curvature and more slowly to concave curvature. Similar findings were reported by Webster, DeGraff, Eaton [59].

For cases where the curvature is more complex, for example alternately concave and convex, Bandyopadhyay and Ahmed [10] observed a lower value of skin friction for the case of flat wall to concave to convex to flat wall compared to the case from flat

to convex to concave back to flat. In the regions of concave curvature the outer-layer turbulence intensity was amplified whereas in the convex regions it was suppressed. Tsuji and Morikawa [56] report the disappearance of the log region in the case where an alternating pressure gradient is applied on a flat wall, after the first switch between adverse and favorable. An internal layer formed in the second oscillation to an adverse pressure gradient.

While the curvature changes the flow significantly compared to a flat wall, it is useful to understand the concepts related to laminar and turbulent flat-plate boundary layers in order to draw conclusions and comparisons. Next I take a short deviation to introduce the equation associated with flow over a flat plate. While these equations are not directly applicable to the problem of the waving plate, the flat plate boundary layer profiles can serve as *guideline* for this investigation.

2.3 Equations of Motion for Near-Wall Flow

The Navier-Stokes equations

$$\frac{\partial \mathbf{u}}{\partial t} + \mathbf{u} \cdot \nabla \mathbf{u} = \frac{1}{R_e} \nabla^2 \mathbf{u} - \nabla p, \tag{2.1}$$

and continuity equation

$$\nabla \cdot \mathbf{u} = 0, \tag{2.2}$$

can be used to generally describe the fluid flow where the vector $\mathbf{u}$ is the velocities u, v, and w in their respective x, y, and z directions, $R_e = uL/\nu$ is the Reynolds

number, ν is the kinematic viscosity, and p is the dynamic pressure.

Total stress on a fluid particle can be represented by the stress tensor

$$\sigma_{ij} = -p\delta_{ij} + 2\mu\left(e_{ij} - \frac{1}{3}\triangle\delta_{ij}\right) \tag{2.3}$$

where

$$e_{ij} = \frac{1}{2}\left(\frac{\partial u_i}{\partial x_j} + \frac{\partial u_j}{\partial x_i}\right) \tag{2.4}$$

and

$$\triangle = e_{ii} = 0 \tag{2.5}$$

by continuity. These relations for the stress tensor are substituted into the momentum equation

$$\rho\frac{Du_i}{Dt} = \rho F_i + \frac{\partial \sigma_{ij}}{\partial x_j} \tag{2.6}$$

resulting in the familiar Navier Stokes Equations

$$\rho\frac{Du_i}{Dt} = \rho F_i - \frac{\partial p}{\partial x_j}\delta_{ij} - \mu\left(\frac{\partial u_i}{\partial x_j} + \frac{\partial u_j}{\partial x_i}\right). \tag{2.7}$$

This can be broken down into average and fluctuating components of velocity, pressure and force, time averages and simplified to arrive at the Reynolds Averaged Navier-Stokes equations. References to these derivations can be found in [45] and [61].

2.3.1 Flat Plate Turbulent Boundary Layers

Following from the Reynolds averaged Navier Stokes Equations we arrive at a relation for the local mean stress near the wall

$$\overline{\tau_w}(x) = \mu\frac{\partial\overline{u}}{\partial y} - \rho\overline{u'v'} \tag{2.8}$$

which remains practically constant in the near wall region. The first term on the right hand side represents the contribution to the shearing stress by viscous dissipation and the second term is due to dissipation through turbulent fluctuations.

From here we can separate near wall flow into an inner and an outer region. This inner region is the one of interest to us here since it can lead us to the wall shearing stress and it in turn can also be divided into a viscous sublayer, very near to the wall where the effects of viscosity dominate, and an inertial sublayer where the viscous effects dwindle and velocity fluctuations prevail.

In flat plate boundary layer theory several relations for the flow in these two regions have been well described through scaling laws. Taking equation 2.8 and dividing through by ρ we can define a velocity scale, u_*, as

$$u_*^2 \equiv \frac{\overline{\tau_w}(x)}{\rho} = \nu\frac{\partial\overline{u}}{\partial y} - \overline{u'v'}. \tag{2.9}$$

This quantity is referred to as the frictional velocity. Dimensional analysis using this newly defined velocity scale will lead us to two non-dimensional variables, or

wall-coordinates, one for length and one for velocity,

$$u^+ \equiv \frac{\overline{u}}{u_*} \; and \; y^+ \equiv \frac{u_* y}{\nu}, \tag{2.10}$$

that will be useful in describing the near wall flow.

Assuming a wall in the absence of roughness, we can look at the shear stress in the viscous sublayer being highly dominated by the viscosity, μ, and much less so by the turbulent fluctuations in velocity which disappear at the wall. Thus

$$\left| \nu \frac{\partial \overline{u}}{\partial y} \right| >> \left| \overline{u'v'} \right| \tag{2.11}$$

and

$$\nu \frac{\partial \overline{u}}{\partial y} = \frac{\overline{\tau_w}}{\rho}. \tag{2.12}$$

Using equation 2.12 we can divides through by ν and integrate over y from 0 to y leaving us with the relation

$$\overline{u} = \frac{\overline{\tau_w} y}{\mu} \tag{2.13}$$

in which the frictional velocity, as defined in equation 2.9, can be substituted revealing the familiar result, given in wall coordinates,

$$u^+ = y^+ \tag{2.14}$$

that can be used to describe the flow very close to a flat wall.

Moving out of the viscous sub-layer, we enter the inertial sub-layer in which viscous

effects no longer dominate and the Reynolds stress takes over. Using Prandtl's mixing length hypothesis we can obtain an expression for the velocity in the intertial sublayer. Prandtl devised that the turbulent mixing viscosity can be defined as a length scale squared times the magnitude of the mean velocity gradient normal to the wall:

$$\nu_T \equiv l^2 \left| \frac{\partial \overline{u}}{\partial y} \right|. \tag{2.15}$$

Near the wall this length scale is $l = \kappa y$ where κ is the universal constant and $\kappa = 0.04$. Equating the stress term, $\overline{u'v'}$, to the mixing diffusivity, ν_T, times the normal gradient of $\overline{u}$ we can derive the relation for velocity in the inertial region

$$u_*^2 = -\overline{u'v'} = \nu_T \frac{\partial \overline{u}}{\partial y} = l^2 \left| \frac{\partial \overline{u}}{\partial y} \right| \frac{\partial \overline{u}}{\partial y}. \tag{2.16}$$

Recalling from above, $l = \kappa y$ we arrive at the following

$$\kappa y \frac{\partial \overline{u}}{\partial y} = u_* \tag{2.17}$$

which can be non-dimensionalized and integrated over y^+ to yield the familiar expression for the velocity in the inertial sublayer

$$u^+ = \frac{1}{\kappa} ln y^+ + C \tag{2.18}$$

which is known as the log-law, with $1/\kappa = 2.5$ and constant $C = 5$ [49].

2.4 Summary

The problems of fish swimming and traveling wave motion are flow control problems that can be enriched by comparing the data to existing results of similar steady and unsteady problems and by drawing upon existing theories. This thesis looks to elucidate the effects of unsteady motion on the near boundary flow near swimming bodies at higher Reynolds numbers than have previously been investigated. How the turbulence intensities change with frequency of motion and how the shear stress changes, both indicate how the drag on the body will change as a result of this unsteady motion.

This is also an experimental investigation warranting a close look at experimental techniques. The following chapter presents various flow visualization techniques and focuses more in depth on the techniques used in this thesis. The *specific* setup for each set of experiments are discussed within their respective chapters.

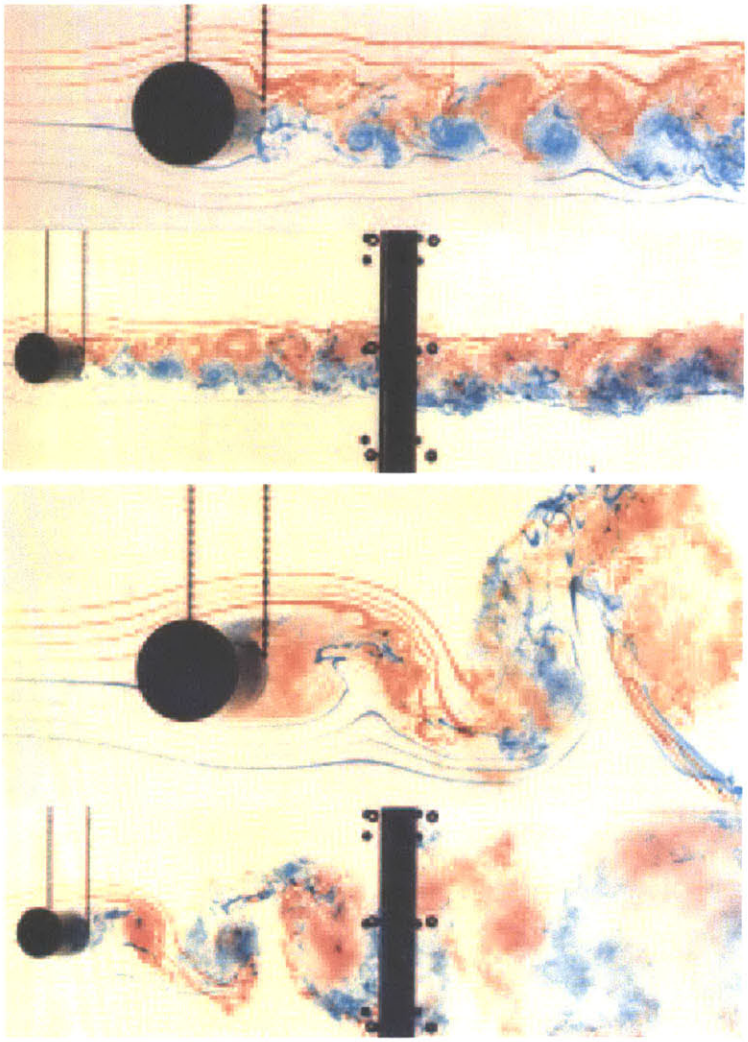

Figure 2-5: Dye visualization of the flow past a rotary oscillating cylinder from [50]. The top image is a stationary cylinder whereas the bottom image is of the rotary oscillating cylinder. The lower images shows the reduction in the width of the drag wake.

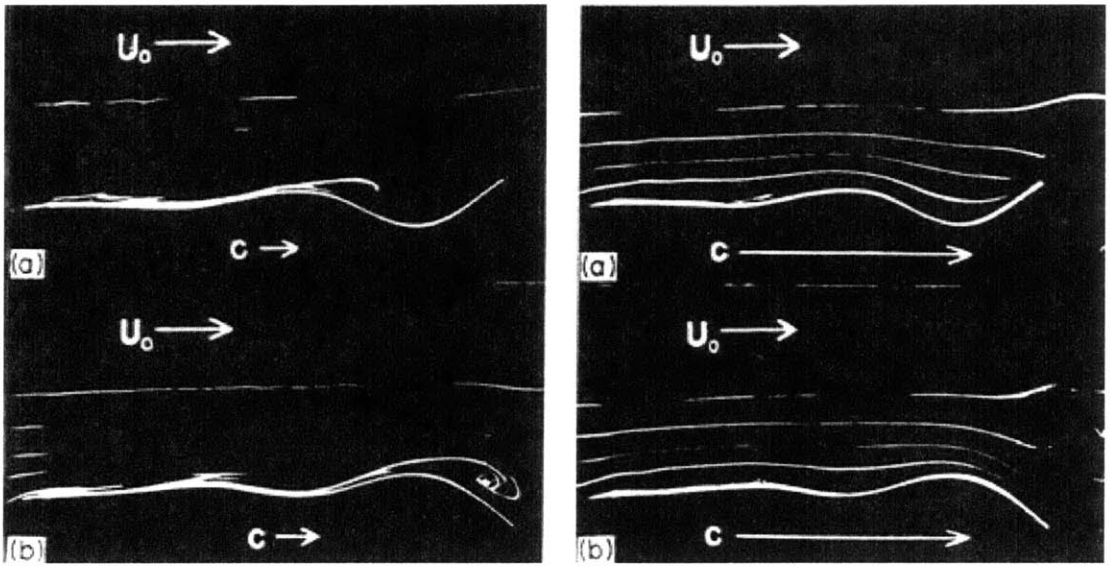

Figure 2-6: Streaklines from the flow over a swimming plate. The images on the left show streaklines for the case where $U_o > C_p$and the images at right are for $C_p > U_o$. From [48]

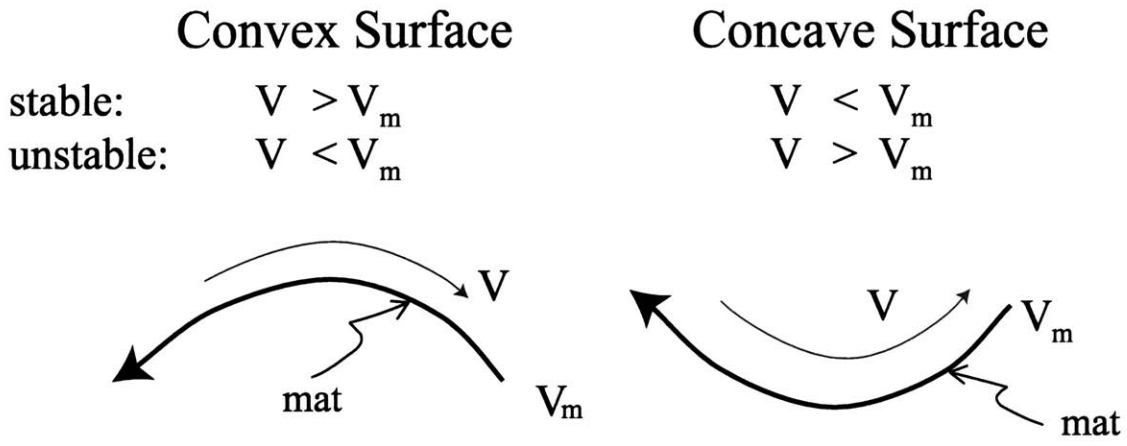

Figure 2-7: Taylor-Görtler instability criterion for the sliding mat.

Chapter 3

Flow Visualization and Measurement

The experimental study of fluid flow has a rich history. Since ancient times the experimental study of fluids has been at the forefront of science. At one point in history the study of fluid phenomena was divided into two separate subjects: hydrodynamics and hydraulics; the former based purely on theoretical, mathematical analysis and the latter based solely on experimentation, disregarding the theory all together. While the division of theories and experiments is still present today, the need to compare theoretical results with accurate experimental data has been realized. This interest has opened the door to a wide array of flow measurement and visualization techniques.

Early studies of flow were done using various dye tracers to observe the flow structures. Such techniques are invaluable in many cases of laminar flow and even when observing the larger scale features of some turbulent flows. However due to the speed at which most dyes diffuse, it is difficult to catch the finer scales present in

higher Reynolds number flows. More recently, techniques have evolved to visualize the smaller scale features present in turbulent flows. Such observations require a finer resolution. Therefore various point measurement techniques and particle imaging methods have been developed. The widespread availability and lower costs of lasers has proved extremely useful in such studies.

These modern flow visualization techniques will hopefully lead researchers to a clearer understanding of perhaps the greatest mystery on fluid dynamics: turbulence. Despite years of investigation, neither a clear definition nor a clear picture of turbulence exists today. In all the efforts to better understand turbulence we have only succeeded in describing its characteristic properties–fluctuating, disorderly, random, three-dimensional, etc... Flow visualization can yield insight into this perplexing problem, but first the techniques presently available need evaluation as to the applicability of each method to the phenomenon being studied.

Through many experimental studies the usefulness of whole-field velocity measurements for gaining a clearer picture of the average flow quantities has been demonstrated. However it is important to asses the applicability of these techniques to turbulent flow field measurements. What are reasonable expectations for the spatial and temporal resolution of a turbulent flow field: how small do we need to measure to better understand the flow or to compare with popular CFD schemes such as LES and DNS. This chapter aims to shed some light on these issues and look at these methods of flow measurements, their benefits and limitations. One specific example of turbulent flow measurements within a flat plate boundary layer will be analyzed to illustrate the range of scales possible to measure using PIV.

3.1 Qualitative Flow Visualization Techniques

An early subset of flow visualization techniques were mainly qualitative in nature. These visualization methods yielded insight into the features of the flow and the patterns made by disturbances introduced into the flow field. However very little quantitative data could be extracted from these pictures. Much of what we understand about fluid flow results from the physical observations of fluid: watching the water swirl behind a child's hand as they play in a swimming pool, or standing on a pier and watching the eddies form from a piling in a strong current, or determining how to cross over a powerboat's wake when water-skiing. Few of these things require more than the human eye to discern what is happening on a large scale. However techniques exist to help scientists better understand these and other fluid effects in laboratory settings.

Most simply is the addition of a tracer particles, or dye, into the fluid revealing the flow path and behavior. Both still cameras and video cameras can be used to capture snapshots or sequences of images that display the flow's features. Substances as unlikely as milk, aluminum flakes, and hydrogen bubbles have been used in such studies in the past and still today. These techniques yield similarly useful images of larger scale flow structures at low-to-moderate Reynolds numbers. An elegant example of the Kármán street behind a cylinder at Reynolds number of 140 is taken from the cover of Van Dyke [57] and shown in figure 3-1.

With the random fluctuations in turbulent flows and the many spatial scales present, the need for whole field flow mapping becomes evident. Here researchers

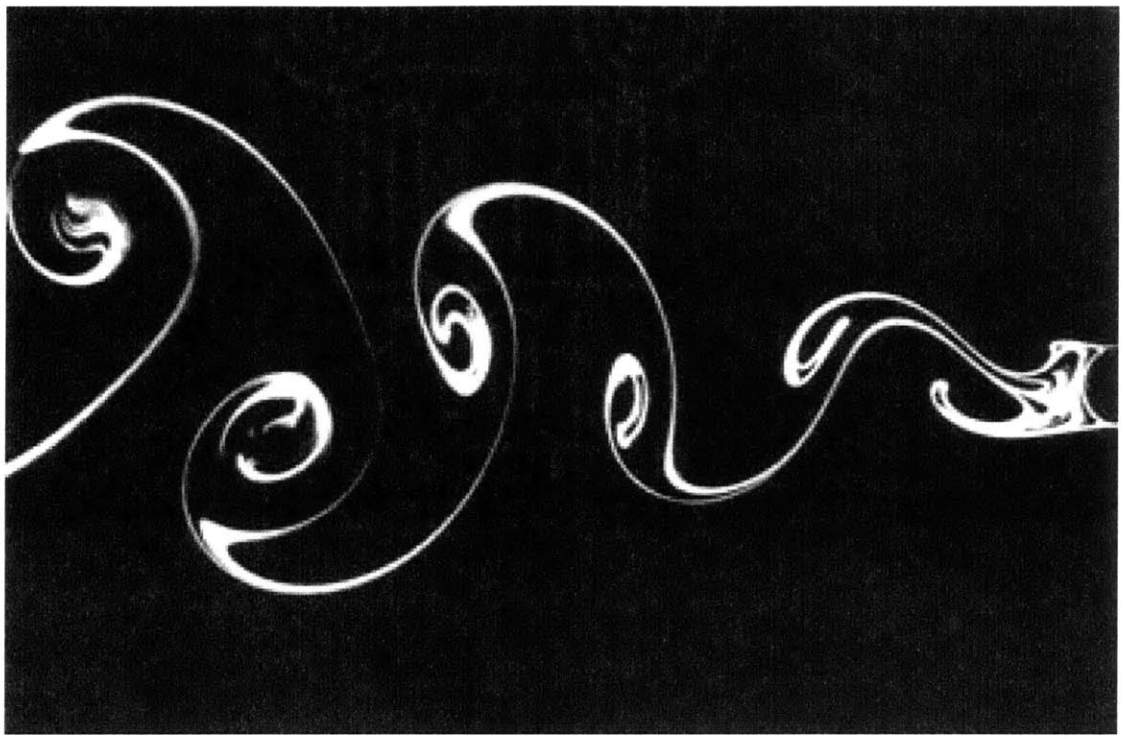

Figure 3-1: Kármán vortex street elegantly captured through flow visualization. Photograph by S. Taneda, from [57].

have used many different particle techniques to better understand the flow field. First uses of particles recorded with long exposures the streaks made as the particles moved with the flow. The exposure time was known and the length of the streaks measured to yield the velocity at with the particles are moving. This particle streak velocimetry (PSV) is the basis for today's PIV techniques.

3.2 Quantitative Visualization

Recently, techniques have evolved to visualize the smaller scale features present in turbulent flows. Such observations require a finer resolution. Therefore various *quantitative* point measurement techniques and particle imaging methods have evolved.

The advent of lasers has proved extremely useful in such studies [1, 2].

Initial attempts at flow field mapping were done using time intensive techniques such as Hotwire Annemometry (HWA) (see [16]), Laser Doppler anemometry (LDA) and Laser Doppler Velocimetry (LDV). These non-invasive point measurements yield very good temporal resolution; however being point measurement techniques, they lack in spatial resolution. Unlike other particle methods, DPIV and particle tracking velocimetry (PTV) allow the measurement of an entire instantaneous two-dimensional velocity field and the corresponding vorticity.

Hot wire anemometry was first introduced into fluid mechanics in 1914 by L. V. King [32] (Lemonis & Dracos 1996). King derived the relationship between the anemometer bridge voltage and the fluid velocity as

$$E^2 = A + BU^n \tag{3.1}$$

where n is determined experimentally and is usually taken to be about 0.5. This and the relationship to find the pitch and yaw angles of the flow with respect to the probe are derived for ideal probe geometries and heat transfer properties. Thus their use in the *real* world lead to significant errors and limitations. Especially important in HWA is the fluxuations in the temperature of the ambient flow. These fluxuations can be read incorrectly by the probes as velocity variations.

Assuming constant temperatures multi-hotwire probes or pulsed hot wire systems have been developed and successfully employed in fluids research. However several constraints are placed on such equipment. For example, in multi-wire probes the

diameter, d, of the sensing array limits the smallest measurable scale in the flow. In between points of measurements a linear velocity profile is assumed. For the example of a vortex, if it is too small or centered at one probe the linear profile assumption is not valid and leads to increased error. The only way to completely correct this in applications to turbulent flow is to decrease the probe sensing diameter such that it is smaller than the Kolmogorov microscale, η. Today this still exceeds manufacturer's capabilities since probes are $\approx 1\ \mu m$ the average four wire array is no less than 0.4 mm in diameter. In the case of boundary layers, η can be 0.2 mm or less making the smallest scales invisible to the probe.

To measure vorticity more than one probe should be placed in close proximity to the others, three or more prove useful in computing the vorticity derivatives. Since the essential processes of enstrophy production and viscous dissipation scale with the Taylor microscale, λ, [49], it is thought that the loss of information due to lack resolution will be limited if the spacing between the probes in an array are between three to seven Kolmogorov scales and three to five Taylor microscales [32]. In addition, the calibration of the hotwire probes is quite complex, though modern probes are factory calibrated and do not drift as significantly as older models.

While HWA or CTA is an intrusive method of flow measurement, laser based techniques offer similar frequency resolution but non-intrusive alternatives to wire probes. LDV relies on the laser beam from a continuous wave laser, often guided through a fibre-optic cable, bouncing off particles seeded in the flow. LDV does not want a high density of particles like PIV, as will be discussed in the next section, and like CTA, is only capable of measuring the velocity components at one point in space

yet has significant temporal resolution.

LDV systems comprising of an argon-ion laser use the two color beam emitting from the laser head. One color is used for the u-component and the other is oriented 90° to measure the v-component. With the inclusion of a fiber-optic probe the two perpendicular measurement axes can be oriented in any direction. For tests at the MIT propeller tunnel the two beams measure u- and v- velocity in the tunnel reference frame, horizontal and vertical respectively. Processing systems, like the one from DANTEC used at the Propeller tunnel, allow the acquisition of one component or both components of velocity. When both components are acquired for the purpose of calculating turbulence statistic, they must both be valid in order to assure accurate statistics. If one component is deemed invalid by the processor neither is recorded. Depending on seeding densities, LDV can acquire up to 180 Hz, much higher than PIV.

The evolution of videographic equipment, digital computers and high power pulsed lasers has brought Particle Image Velocimetry, PIV to the forefront of fluid mechanic experimentation and visualization. A comprehensive review of PIV and particle imaging techniques is given by Adrian [1], [2]. The digital implementation of PIV is outlined by Willert and Gharib [62].

PIV is the measurement of the instantaneous whole-field velocity components and the respective vorticity field, by comparing snapshots of particle laden flow at two instances close in time. The movement of the particles from image to image yields the velocity vectors associated with the flow. In general PIV track groups, patterns, of particles in an image using digital FFT and cross-correlation routines, while particle

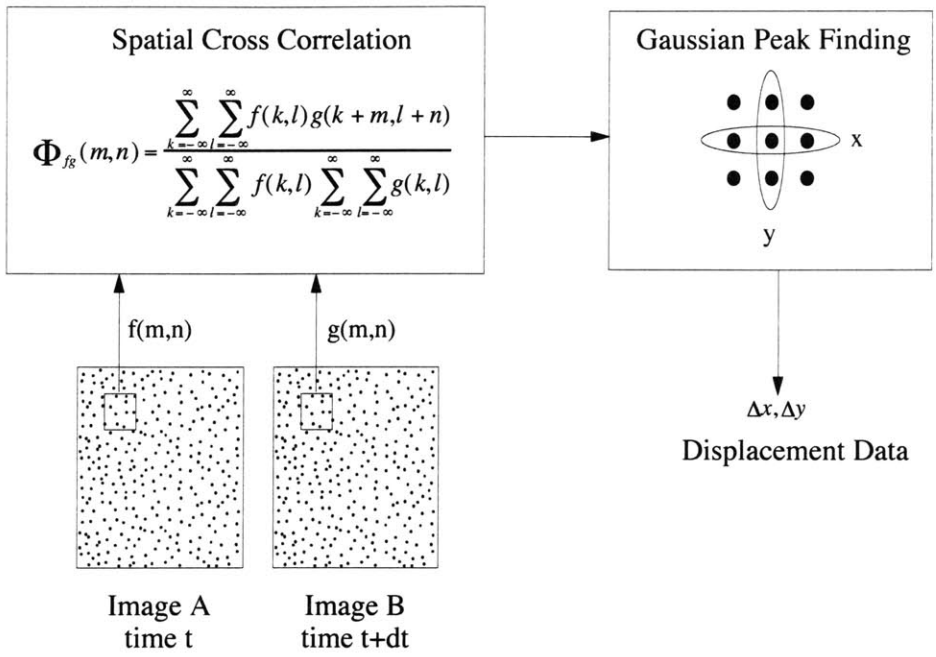

Figure 3-2: DPIV Algorithm

tracking velocimetry (PTV) tracks each particle.

In most PIV setups a single two-dimensional plane is illuminated using a laser beam that is focused and fanned to form a thin plane sheet of light. Certain low-cost PIV applications use Halogen lamp sources or small diodes to illuminate the flow, whereas other setups use high powered pulsed ND:Yag lasers capable of vaporizing air. The fluid is seeded with neutrally buoyant fluorescent particles (diameter $\approx$ 40 to 70 μm depending on the size of flow field under interrogation) which reflect wavelengths in the range of 560-580 nm. Willert and Gharib [62] found that 10 to 20 particles per interrogation window were sufficient to ensure good correlations. Camera positioning must ensure that the particle images are approximately 2-3 pixels in size, since most algorithms cannot resolve sub-pixel images.

A diagram of the algorithm is shown in Figure 3-2. Image data from two successive

video frames are collected and stored digitally in levels of grayscale. In each of the frames we examine small interrogation windows at the same spatial position and the data, $f(m,n)$ and $g(m,n)$ are used to calculate the cross-correlation function,

$$\Phi_{fg} = f(m,n) \circ g(m,n) = \sum_{k=-N/2}^{N/2-1} \sum_{l=-N/2}^{N/2-1} f(k,l)g(k+m,l+n) \tag{3.2}$$

where m, n refer to the individual pixels and N is the size of the interrogation window in pixels. This cross-correlation measures how closely the two images match.

A strong narrow peak in the correlation function provides the average displacement of the sampled group of particles. The correlation peak is located with sub–pixel accuracy using a Gaussian curve fit to the data around the maximum correlation value in both image directions independently. The Gaussian fit takes the form

$$p(\zeta) = c_1 e^{-\frac{(\zeta - c_2)^2}{c_3}}. \tag{3.3}$$

The correlation maximum and four additional data points, as indicated in figure 3-2 by the encircled points in the peak finder box, are used to complete the model. This model works best when the peak is broad and particle images are larger than a few pixels in size.

The effect of the DPIV windowing process is that of a spatial low-pass filter. Using the analysis in Willert and Gharib [62], a 40% attenuation of features on the order of 64 pixels is observed when a 32 $\times$ 32 window is used in the processing. The attenuation is limited to less than 10% for features nearing 160 pixels in size.

Similarly, for a 16 $\times$ 16 processing window, features on the order of 32 pixels are attenuated by approximately 35%, and a 10% attenuation is realized for features near 75 pixels in size. We estimate a mean relative RMS error of 5–6% for particle displacements in the range of 0–9 pixels; absolute errors ranged from 0.01 pixels to 0.15 pixels. Increased seeding densities beyond 20 particles per 32 $\times$ 32 window show no significant improvement in uncertainty. A typical relative RMS error for moderate pixel excursions (greater than 1 pixel) is of the order of 5%. In terms of velocity this results in typical absolute error of 0.2 cm/s for a time step of 20 ms, resulting in a relative velocity error of 7.5%.

High resolution, black and white CCD video cameras are most often employed in PIV applications. Standard CCD camera resolution ranges from 240 x 480 to 1134 x 480. Higher resolution cross correlation cameras specifically designed with PIV in mind can yield from 1K x 1K up to 4K x 4K images. Other video issues involve the saturation time of the CCD chips, the transfer time between the pixels and the computer memory, the squareness of the pixels, whether or not the camera is interlaced, and the limitations of the video card used to digitize the images.

For example the Texas Instruments RS170 (analog) CCD camera used in the MIT Towing Tank records the flow with a maximum pixel resolution of 1134 x 480 pixels at a standard frame rate of 30 Hz. Dual field exposure renders full vertical resolution with no interlace. The video from the CCD camera is stored real-time by a MuTech Frame grabber into 128 Mb Ram on a 133 MHz Pentium Processor PC. Present capabilities allow us to capture the full 1134 x 480 image with the MuTech board, however originally the board only allowed capture at 640 x480. The system used in

the waving plate experiments discussed in chapters 6 and 7, centers around a Pulinix TM1040 1K x 1K Progressive Scan camera and CORECO digital frame grabber which can aquire images at 30Hz into 300 MB of computer memory on a Pentium II 600 MHz PC.

Processing and storage of the image pairs is also an interesting problem. Several different processing algorithms are being used today, more robust codes allow for processing in both the frequency domain (by FFT) and in the spatial domain by direct spatial cross correlation. Both methods have advantages and disadvantages.

The FFT requires that the sub-image array size be a power of two, however computationally it is a much faster method than the spatial cross-correlation (13 times faster as reported by [37, 39]). Despite its slower speed, the spatial method allows for more accuracy. In the spatial mode a much larger region must be searched when calculating the correlation, this avoids any confusion that might arise in the FFT method if particles move in or out of the single search window. Dynamic search algorithms and hybrid FFT/spatial codes allow great flexibility in processing [39].

Temporal resolution of DPIV is dictated by the frame rate of the camera, which is typically 30 Hz, and since we need two images to perform DPIV calculations, the system effectively operates at 15 Hz. This allows us to observe features that fluctuate on the order of 15 Hz or slower, but not faster.

As for spatial resolution, DPIV is limited by two main factors–the window size and the step size. In order to resolve the desired length scales these windows must be adjusted accordingly. For both the Dabiri and Gharib code and the McKenna code ([37] and [38]), the attenuation of features on the order of less than twice the window

size were seen to be attenuated. As for step size, caution should be taken to maintain a step size larger than the mean particle separation. The smallest scales resolvable are those on the order of twice the step size, by the Nyquist criterion. Error analysis of PIV is further discussed in Adrian [3], Huang *et al.* [28], and McKenna [39].

3.2.1 DPIV Spatial resolution

The spatial resolution of a given flow field can be determined by looking at the PIV processing algorithm and the hardware used to record the data. For the experimental equipment used in the tow tank we can estimate the spatial resolution of our DPIV setup simply as follows.

In general it is necessary to know the resolution at which the images are digitized, the squareness ratio of the pixels stored by the video board, the size of the sampling window and window step size used in processing. If we are imaging an area that is X mm by Y mm into 1134 x 480 pixels, then we know the number of pixels per cm in each image. For the EPIX video board, which digitizes at 768 x 480, the squareness ratio, SR, is 1.16667, however for the MuTech board digitizing at 1134 x 480 the SR is more like 1.57. For simplicity we can use a SR $\approx$ 1.0 and the average of the two length conversions (pix/mm) to *estimate* the spatial resolution. However, in processing the data the squareness ratio and the horizontal length conversion are used.

For an image with real dimensions: 97.5 mm x 65.0 mm and pixel dimensions: 1134 x 480, the length conversion on the horizontal direction is 11.6 pix/mm and 7.4 pix/mm in the vertical direction. The average length conversion is 9.5 pix/mm.

Using a typical window size of 32 x 32 and a step size of 8 pixels in both directions, we can presume that features smaller than 64 pixels (or 6.7 mm in real space) in size will be attenuated approximately 40% . Attenuation decreases with feature size to about 10 % for features on the order of 160 pixels or 16.8 mm.

The minimum wavelength resolvable is determined by the step size. Nyquist criterion states that the smallest resolvable scale is twice that of the step size. For a step size of 8 pixels we have 0.842 mm between velocity vectors. Thus the minimum wavelength is $\lambda = 1.684mm$, which in turn implies that we can resolve wavenumber, $k = 2\pi/\lambda$, up to 3.73 $1/mm$. Assuming the flow seeding is sufficient (10-20 particle per window) we can obtain higher spatial resolution by decreasing the window size to 16 x 16.

For the same image above, using a 16 x 16 window and a step size of 4 pixels, we can obtain a finer resolution. It is important to note here that the minimum step size is determined by the mean particle separation. If the step size is smaller than this separation, no new particles will enter the area of interest and thus no new data will result. Here we are limited again in how small a feature we can resolve. Assuming the step size is sufficient however, the maximum wave number resolvable is $k = 7.46\ 1/mm$.

Using the discussion in Tennekes and Lumley [49] we can estimate whether or not the maximum wavenumber resolvable using DPIV corresponds to turbulence in the equilibrium range. Looking at a turbulent boundary layer we can give a scale relation for the length and velocity scales as follows

$$\frac{l}{L} = \frac{\delta}{L} \approx \frac{u}{U_o} \tag{3.4}$$

where δ is the boundary layer thickness and L is the reference length for the mean flow (in a flat plate boundary layer this is the plate length), u is the velocity scale within the boundary layer and U_o is the free stream velocity. In the equilibrium range of turbulent flow Kolmogorov's Equilibrium theory states that the rate of production of turbulent energy is equal to the dissipation rate, $P = \varepsilon$. Assuming that the smaller scale motions are independent of the large scale turbulence of the mean flow and are dictated by the kinematic viscosity, ν, and the rate of production of energy by large scale turbulence, or the dissipation, ε, we can define the Kolmogorov length and velocity scales as

$$\eta \equiv (\nu^3/\varepsilon)^{1/4} \; and \; \upsilon \equiv (\nu\varepsilon)^{1/4}. \tag{3.5}$$

Since the energy dissipation is dictated by the large scale motions it can be written in terms of the large scale velocity within the boundary layer, u, and the boundary layer thickness, δ, such that $\varepsilon \approx u^3/\delta$ (Taylor, 1935). Combining the relation for the energy dissipation rate with equations 3.5 we get a relationship between the small and large length scales: η and δ,

$$\frac{\eta}{\delta} \approx \frac{1}{\delta}\left(\frac{\nu^3}{u^3}\delta\right)^{1/4} = R_\delta^{-3/4}. \tag{3.6}$$

Next, it is important to look at the energy spectra for the equilibrium range and

for the large scale motions. The spectrum in the equilibrium range is determined by

$$\frac{E(k)}{\nu^{5/4}\varepsilon^{1/4}} = \frac{E(k)}{v^2\eta} = f(k\eta) = \alpha(k\eta)^{-5/3}. \tag{3.7}$$

where α is a constant. Similarly, the large scale energy spectrum is written as

$$\frac{E(k)}{\varepsilon^{3/2}S^{-5/2}} = \frac{E(k)}{u^2\delta} = F(k\delta) = \alpha(k\delta)^{-5/3}, \tag{3.8}$$

where $S = u/\delta$ and $\varepsilon = u^3/\delta$. Note that the two energy spectra scale as the product of a wavenumber with the length scale to the $-5/3$ power. Figure 3-3 shows the plot of the energy spectrum non-dimensionalized by the larger scale, δ (or in this plot ℓ).

Note that the equilibrium wavenumbers are determined by the range in which the spectrum follow the $-5/3$ power curve, and are thus determined by the the dashed lines on either side. The upper cutoff is $(k\eta) = 0.55$ and the lower cutoff is $(k\delta) = 1.88$. Take, as an example, a free stream velocity of 0.6 m/s at $x = 1m$ down the plate, and using the expected δ for a turbulent boundary layer and $R_\delta = U_o\delta/\nu$. Here we see that the highest wavenumber in the equilibrium range is near 29.51 $1/mm$ and the lowest near 0.069 $1/mm$. Comparing with the results found for the resolution of DPIV with a 32 x 32 pixel window, we see that $k_{low} < k_{DPIV} < k_{max}$. Thus it is shown that we can resolve scales within the equilibrium range.

In practice, spatial resolution is effected by experimental conditions and may not be resolved as well as predicted in theory. The spatial resolution, inline with the inflow, of the actual data sets can be gleaned from the power spectral density of the velocity in the longitudinal (streamwise) direction. The spectrum can be obtained

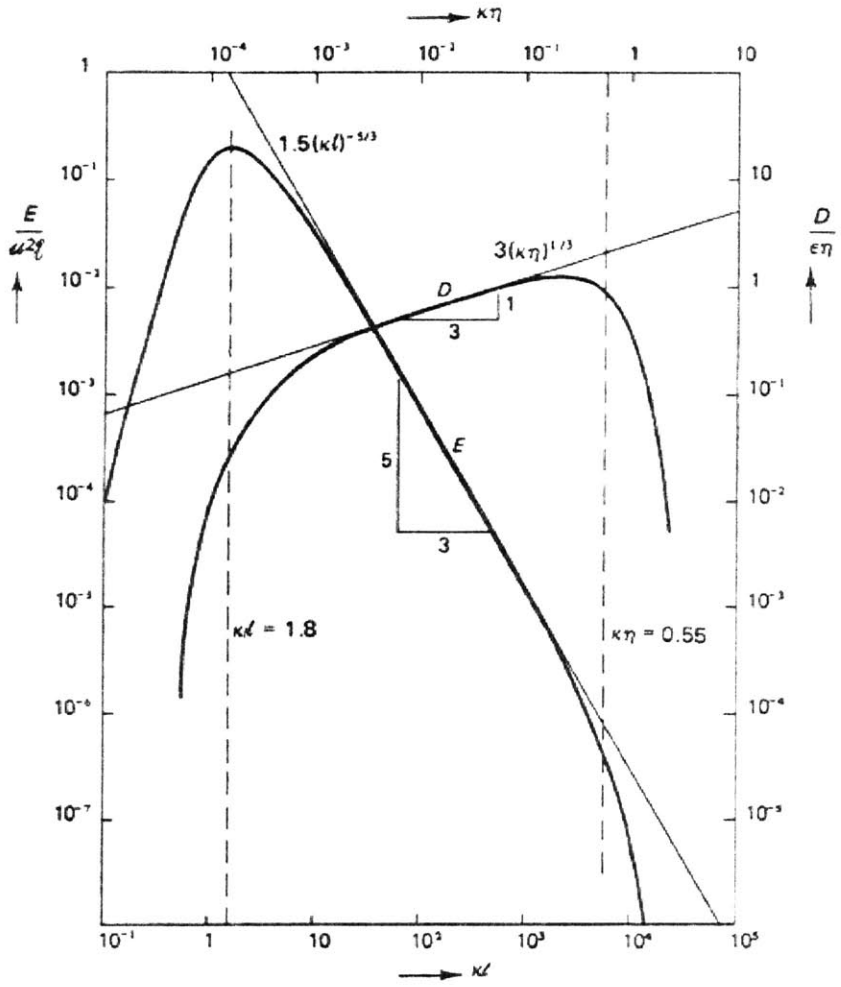

Figure 3-3: Energy spectrum (from Tennekes and Lumley 1972)

for several heights from the wall. Figure 3-4 shows the energy spectrum three points from the boundary. These plots are shown for the four different wave phase speeds, $\zeta = 0.3$, 0.6, 1.0 and 1.2. The upper end of the wavenumber spectrum falls off the $-5/3$ line around $k = 3.1\ 1/mm$. Thus the resolvable wavelength is 25% larger than predicted.

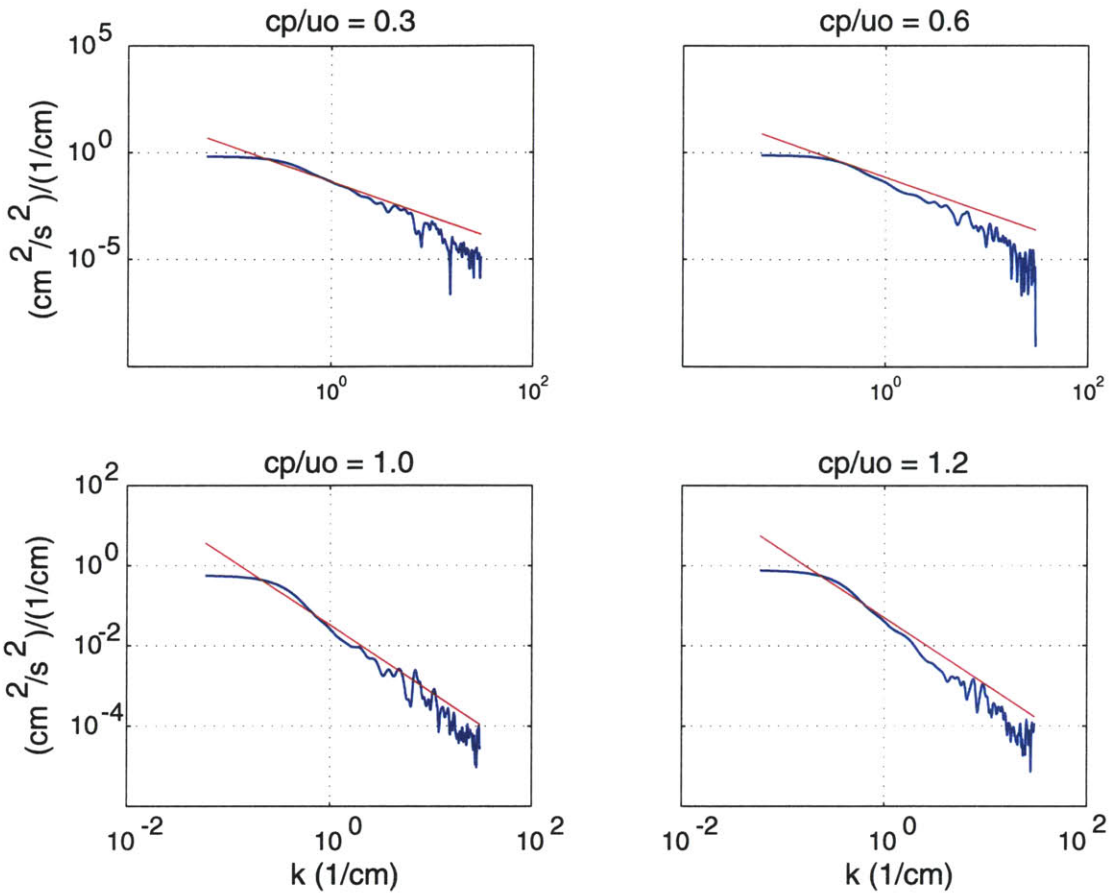

Figure 3-4: Power Spectral Density for the swimming mat PIV data sets. The box size in processing is 32 x 32 *pix* with 16 pixel step.

3.2.2 Particle Tracking Velocimetry

Particle tracking velocimetry (PTV) is similar to PIV in application, however PTV resolves the displacement of each particle in an image pair instead the displacement of a cluster of particles as in PIV. Most PTV algorithms use PIV as a first-pass coarse grid analysis of the images before actually determining the actual motion of the particles. Once the coarse PIV is analyzed the PTV algorithm uses this information to guide its way through the tracking process. Particle tracking yields a vector for almost every particle in the image, however these particles are rarely spaced uniformly

throughout yielding an unstructured velocity field. Difficulties arise in flows with strong gradients and swirls, since PTV uses the mean PIV as an estimation. It tends to work best where the flow is nearly parallel within a small interrogation region, but algorithms are being investigated to improve PTV even in swirling flows. Methods have been developed using Gaussian convolutions to smooth a PTV field and still improve the spatial resolution by 2-3 times in both direction [41].

Techniques have been developed to convert the unstructured PTV data into a smoothed regularly gridded data set. An example of such a technique can be found in [41]. In this example PTV yields many more vectors that PIV would have hoewever they are scattered within the region of interest. A gaussian smoothing algorithm is applied to the data set resulting in a well ordered velocity vector field with 2.5 times the resolution of the original data set.

Super resolution PIV and particle tracking techniques can prove useful in conjunction with basic PIV algorithms in limited regions where the gradients are too large to be resolved by the correlation interrogations [41]. Thus one could conceivably target regions in which the gradient is too large to be determined using the fixed resolution algorithm and re-analyzing with a super-resolution algorithm. This is similar to adaptive- and multi-grid methods used in numerical analysis. Such techniques also prove useful in increasing the capabilities of digital PIV to that of cinemagraphic PIV without the hassle of spending hours in a dark room.

As PIV gives researchers the added benefit of increased spatial resolution and whole-field 2D measurements without hours of painful point measurements, we cannot discount many of the well-established techniques such as CTA and LDV. A comparison

of LDV, PIV and DNS simulations is given in a study of turbulent channel flow by [35]. It can be seen that an ensemble of 11 PIV data sets closely compares with LDA and DNS data. The data is remarkably close for each technique illustrating the inherent benefits of PIV data for comparison with and verification of numerical results.

3.2.3 Particle Tracking Velocimetry in the boundary layer

Particle tracking velocimetry (PTV) as developed by Luthi [36] was designed specifically to process the sparsely seeded images in the *RoboTuna*near boundary visualization experiments. The code allows several methods for processing the data depending upon the seeding and image quality. For the experiments with the MIT *RoboTuna* it was often difficult to obtain consistent and sufficiently dense seeding to apply standard PIV techniques, thus an alternate technique was needed.

Initially a 'pattern matching' algorithm creates centers of matched neighboring particles which then act as starting points for the successive strategies. From here either a 'classic' PTV method or the 'divergence method' can be used depending upon the image pair. Finally the user has the option to manually perform PTV by using the mouse to choose matching particles. The code also is capable of identifying the body boundary and eliminating the portion of each image which not of interest to the user. This allows the particle locations to be determined as a function of their distance from the body boundary.

The particle locations were determined in several steps. First the images were

filtered by finding the image intensity gradient to reveal the boundary of each particle. Taking the gradient of the image also reduced the body boundary to its most simple form, its outline. The gradient algorithm determines whether each pixel is brighter or dimmer than its eight surrounding neighbors. If the pixel value of the said particle is less than all of its surrounding neighbors it is set to zero (or false). Else if it is greater than at least one neighbor the gradient is set to the value of the highest gradient determined. This reduces the calculations to comparisons and subtractions only, eliminating the need for a 3x3 convolution matrix which requires more costly multiplications and additions.

Now the image is converted to a binary array and thresholded such that true pixel values are defined above a threshold level of $0.1 * (gradient_{max} - gradient_{min})$. The images then must be filtered to eliminate any noise. This is done by a simple 'game of life' algorithm. First all missing corners are filled. Here each particle which is set to *false* is examined to determine whether it has at least three *true* neighbors. If so then it is reset to *true*. Next the image is filtered such that if *true* particle does not have at least two adjacent *true* neighbors then it is reset to *false* thus eliminating any noise.

Once the images are thresholded and the particles and body boundary are extracted then the velocity vectors can be determined by the following algorithms. First four initial centers of matched particles are determined. These centers act as starting points for successive, faster matching schemes.

For each particle six potential matches (in the second image) are located such that these particles are no more than three average particle distances apart (the average

particle distance is determined from the number of particles per image area). From here the potential matches are compared to the matches from the particle's neighbors in the initial image. The better the match the higher the probability that its neighbor will have a match in the same direction. These matched particles are used as guides for the subsequent matching schemes.

Once the *seed* matches are determined, there are now two options to employ. First is a *classical* method and second a *divergence* method; these two methods are described briefly below, further detail can be found in [36].

The "classical" method extends the matched seed particles in several sweeps by always using the previous matches to guide the algorithm. The size and shape of the search window is defined by the average particle distance, the search angle, and a minor and major radius. The major and minor radii depend on the maximum acceptable accelerations and decelerations of particles as well as the average particle distance. Thus it has difficulties at centers of high gradients and where there are very low seeding densities. In contrast, the "divergence" method uses a least squares approximation to find the trajectory of the particle given the motion of the neighboring particles. Three triangular regions are created using the particle of interest and four neighbors. A linear approximation for the flux through each of these regions is calculated, next $\nabla \cdot V = 0$ is solved leading to an over constrained system which can be solved with the least squares method.

The particle tracking code requires the user to choose which method is used from the outset and falters in regions of high seeding density. However in the data obtained on the RoboTuna, this was not a problem since seeding was sparse.

3.3 Multi-Grid Methods for DPIV in High Gradient Flows

Basic PIV techniques are known to have difficulties in flows with steep velocity gradients. Unfortunately the near-boundary case is one of these flows with steep flow gradient. Thus alternative processing techniques need investigation. One such techniques which has been used successfully in computational fluid dynamics is multi-grid processing. Since PIV is unable to determine the flow is a particle moves out of the interrogation window, it is necessary to use a sufficiently large window to capture the flow motion accurately. However if the box size is so large as to encompass an entire region with either a high gradient, or a small recirculation region, then the smaller scale features of the flow are lost to the "big-picture". This is especially important in near wall flows where the boundary layer may be only a small number of pixels thick. Such high gradient shear flows could benefit from adaptive PIV processing techniques to better resolve the flow field.

Scarano and Reithmuller [44] explore an iterative multi-grid approach to PIV. Their technique allows the processing code to iterate through a range of box and step sizes based on a threshold divergence and deviation from the mean and RMS velocities. Their test case, a backwards facing step, clearly illustrates the usefulness of such a technique.

For the flow over a blunt trailing edge airfoil, Fairman [19] used a simple iterative technique to better resolve the boundary layer near the foil at a mean inflow speed of $7m/s$. The high freestream flow speed dominated the processing and tended to bias

the vectors within the boundary layer towards higher speeds when a 64 x 64 pixel window was used. However the 32x32 window was too small to capture the freestream particle motion at that high speed. The image pairs were all processed twice, once with the smaller box size and once with a larger box size. These vector fields were compared using a threshold criterion to determine when (how far away from the foil) the data used would switch from the 32 box to the 64 box. These data sets were compared with both numerical RANS code and LDV data, yielding encouraging results. Obviously this is a very basic implementation of multi-grid methods for PIV, but has opened a doorway for further dedicated investigation of such techniques for bounded flows or high-shear flows.

3.4 Summary

For the purpose of this thesis the two techniques most heavily relied upon were LDV and PIV. The specific experimental arrangements and equipment are discussed in their respective chapters. Experiments in chapter 4 on the *RoboTuna* were performed using the PIV/PTV hybrid code [36] in the MIT towing tank. The final portion of the thesis looks at the work from the two-dimensional waving plate. Chapter 6 presents data obtained using phase averaged LDV results for the waving plate problem and chapter 7 discusses the methods and the results obtained for the PIV experiments with the waving plate.

Chapter 4

Near Boundary Flow Observations Of Robotic Swimming Fish

The unsteady problem of fish swimming has become a topic of great interest to engineers on the quest for faster, more efficient underwater vehicles. With their efficient propulsive capabilities, fish serve as an example of an alternative propulsive mechanism. Biomimetic robots like the MIT *RoboTuna* are valuable in this effort to understand these phenomema. Along with the force measurements and qualitative dye visualizations, quantitative flow measurement is necessary to unveiling the hydrodynamics mechanisms for achieving such propulsive efficiencies. Herein, the near boundary flow about a swimming robotic fish is studied using particle image velocimetry (PIV) and particle tracking velocimetry (PTV). A small area, 2 cm x 3 cm, near the boundary of the fish is recorded and analyzed to obtain instantaneous velocity fields and ensemble averaged (phase-matched) boundary layer velocity profiles.

The swimming motion of the robot is that of a traveling wave with wavelength, λ,

and varying amplitude. Swimming parameters, such as Strouhal number and phase speed of the body wave, can be varied to achieve different swimming configurations. Visualizations at different streamwise body locations are investigated for Reynolds number 800,000. Figure 4-1 captures the *RoboTuna* swimming through the horizontal light sheet during PIV testing; this photograph was taken through the side window of the tank. The light sheet can be seen intersecting the fish along the lateral, or mid-, line and the camera would be positioned to observe the flow field from above.

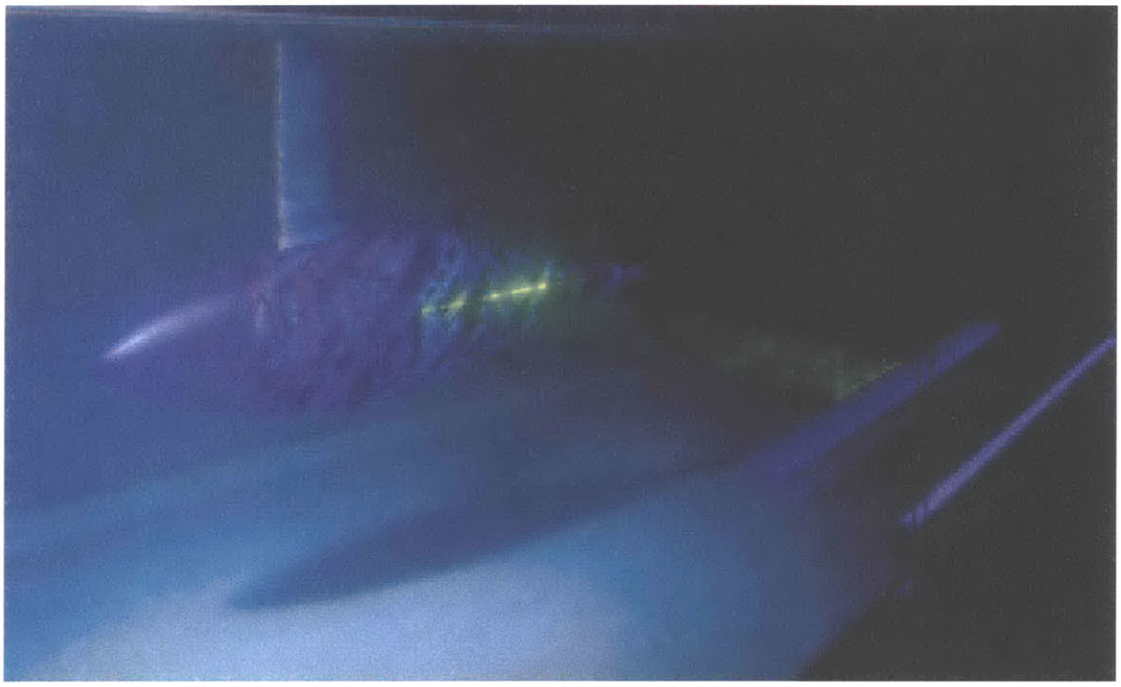

Figure 4-1: Photograph of the RoboTuna swimming through a horizontal laser sheet positioned at the lateral line (Courtesy of T. Blake).

4.1 The MIT RoboTuna: An Overview

The *RoboTuna* resides in the MIT Ocean Engineering Testing Tank, which has dimensions 35 m long, 2 m wide, and 1.25 m deep, and is modelled after the *tunnus tynnus*

(bluefin tuna). It is 1.25 meters from nose to tail and is attached to a towing carriage by a streamlined mast. The robot is submerged such that it swims in the towtank at mid-depth to avoid interactions with both free-surface and bottom. Details of the *RoboTuna's* eight link, pulley and tendon construction can be found in [13].

The lateral motion of the swimming robot's body is given by

$$y(x,t) = a(x)sin(kx - \omega t), \tag{4.1}$$

where x is measured from the second link aft to the tail, $k = 2\pi/\lambda$ is the wavenumber, and $a(x)$ is the amplitude envelope given by

$$a(x) = c_1 x + c_2 x^2. \tag{4.2}$$

The ideal operating parameters, including c_1 and c_2, were determined by a genetic algorithm [12]. For the *swimming* configurations presented here, the phase speed of the traveling wave, $c_p = \omega/k$, is greater than the forward speed.

The carriage operated at a towing speed of 0.7 m/s which ammounts to a Renolds number, based on the robot length, of 800,000. The first case is a non-swimming (straight drag) case and the second case a swimming configuration. The swimming shape is dictated by several kinematic parameters: Strouhal number, wavelength and tail amplitude and phase with respect to the swimming motion. The Strouhal number for the swimming case is 0.182, the wavelength is 1.27 body lengths ($\lambda = 1.65m$), and the maximum amplitude at the tail is 9.96 cm. These parameters are those

programmed into the robot control algorithm, however are not precisely the values maintained by the robot in reality, as there is significant compliance in the tendons within the robot.

4.2 Experimental Setup for RoboTuna Experiments

To further investigate the analogy between undulating boundaries and turbulence suppression, a detailed flow visualization study of the flow very near the boundary of the *RoboTuna* is performed. Experiments are conducted in the towing tank at a Reynolds number of 800,000. Flow is tripped to tubulence at the aft edge of the nose cone due to a gap between the nose cone and the lycra and foam structure of the flexible body. This tripping was unavoidable due to the robot design and not necessarily consistent with live fish, which swim mostly in a laminar regime, as discussed by [7].

For this set of tests, the flow measurements are taken by a camera fixed on the carriage at four stations along the body, all aft of the streamlined mast which connects the robot to the carriage. A schematic of the experimental setup can be seen in figure 4-2. The laser used for PIV is mounted external tot he towing tank and the light sheet is steered in through the side window by a series of optics and turning mirrors. The CCD camera is attached to the carriage at a fixed point along the body.

The camera is a black and white CCD video camera from Texas Instruments, model MULTICAM MC1134P, with a maximum pixel resolution of 752 x 480 pixels operating at a standard frame rate of 30 Hz. A zoom lens is employed on the camera

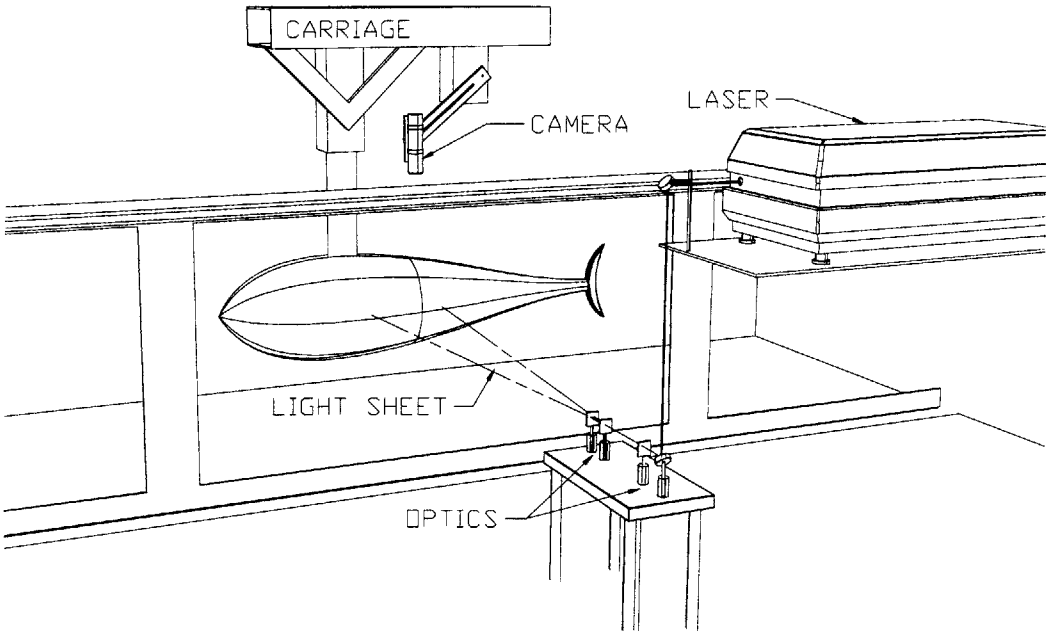

Figure 4-2: Experimental setup for *RoboTuna* experiments. Note the camera is mounted on the carriage partially submerged below the water surface to avoid optical distortions. The laser is fixed at one point along the tank.

to assure a small field of view, 2.0 cm x 3.0 cm, near the body boundary. The camera is encased in a watertight housing and partially submerged, looking down on the laser sheet, to avoid any distortion in the images due to surface ripples. An EPIX frame grabber digitizes the images in real-time into the memory of a Pentium 133 MHz PC.

The digitized images are processed using both a spatial-cross-correlation DPIV method [37] and a particle tracking code [36]. Particle tracking was essential to the processing of the data near the fish boundary (within 0-10 mm) since the seeding was often sparse and non-uniform in this near body region. The particle tracking velocimetry (PTV) code allows several methods for processing the data depending upon the seeding and image quality.

Both a fully automated PTV algorithm and a manual point-and-click option are available. The manual mode allows the user to zoom in on an image and determine the particle match by eye; the location of the particle center has already determined by the code. Throughout the flow field the manual and automated methods yielded nearly identical results; however there were several cases where the images were not sufficiently seeded to allow the PTV code to work efficiently and the manual method was employed.

The code also is capable of identifying the body boundary and eliminating the portion of each image which not of interest to the user. This allows the particle locations to be determined as a function of their distance from the body boundary and confines the algorithm to interrogate the image only in the flow region, thus reducing the processing time.

PTV allowed for better resolution of the boundary layer about the robotic fish, down into the viscous sub-layer. Image sequences are obtained at several streamwise stations along the body, all aft of the support mast. The stations are 54.2, 65.7, 73.7, and 78.7 *cm* aft of the nose of the robot for positions one through four respectively (see figure 4-3). All data was acquired at the centerline (mid-height) of the fish.

4.3 Results from DPIV on RoboTuna

Figure 4-4 presents a typical 2 *cm* x 3 *cm* image and vector field for the straight drag configuration at position one. The top figure shows the digitized image and below is the vector field calculated by the PTV code from the top image and its pair (not

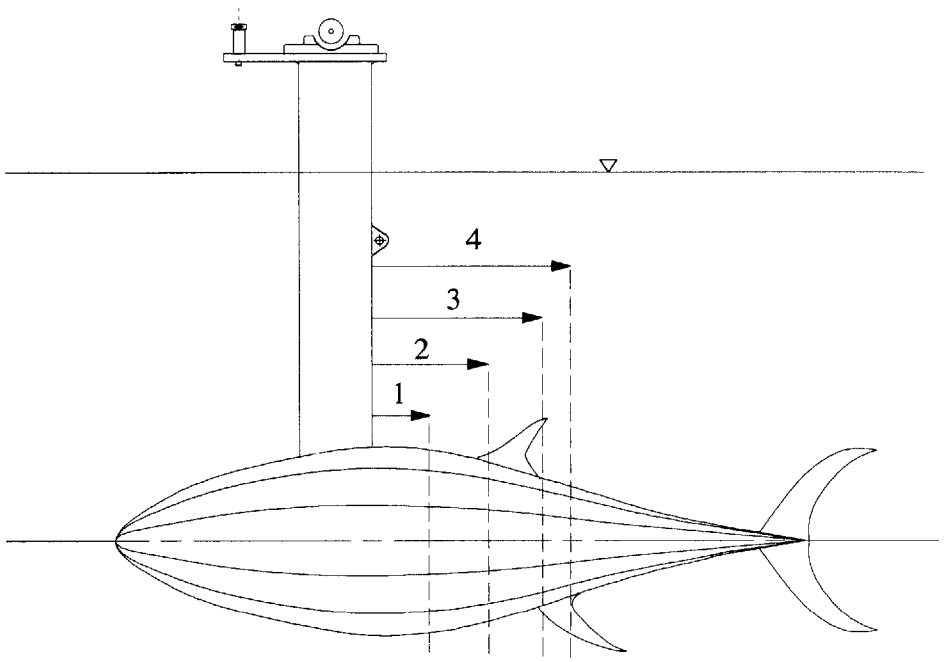

Figure 4-3: Four spanwise positions where visualization is performed. Position #1 is 54.2 *cm* aft of the nose, position #2 is 65.7 *cm* aft, position #3 is 72.7 *cm* aft, and position #4 is 78.7 *cm* aft of the nose.

shown). The edge of the fish body is seen in the lower portion of the top image, the brighter spots on the body are due to the multi-colored fluorescent lycra skin on the fish. The straight line in the vector field is a reference to the edge of the fish body. Note that the coordinates in the top frame are in "image" coordinates with (0,0) at the top left corner whereas the coordinates are switched in the vector plot to better indicate the vector location with respect to the body.

The non-swimming case at Reynolds number 800,000 reveals boundary layer profiles at the four data stations which appear turbulent when plotted against flat plate boundary layer theory. Figure 4-5 plots the average boundary layer profile data for the non-swimming case at each position. At the forward two points (positions #1 and #2) the body of the fish has not begun to taper greatly. The frictional velocity,

used to non-dimensionalize the data, is found from the slope of the velocity very near the wall. Again we mention that the use of flat plate boundary layer theory is merely suggestive and used to guide our study.

For the swimming case presented here, the fish is moving forward at $U = 0.7m/s$, and swimming with a wavelength, λ, of 1.41 m frequency of 0.5668 rad/s, and Strouhal number of 0.182. The ratio of the phase speed of the traveling wave, $c_p = \omega/k$ to the free stream velocity, U_o, is greater than unity: $c_p/U_o = 1.14$. The body of the fish traverses perpendicular to the flow through one cycle from mid-stroke (zero position) to a *trough* (negative tail position) back to mid-stroke, on to the *crest* (positive tail position) and finally back to center. This motion is dictated by the amplitude envelope, a(x), and the swimming wavelength, λ and frequency, ω.

Figure 4-6 illustrates the profiles for the swimming fish. Here is is shown that the swimming motion acts to extend the laminar region beyond that of the non-swimming boundary layer. The three plots represent three phases of the tail swimming motion. From top to bottom are mid-stroke going away from the laser sheet, into a *trough*, just past the trough, and just before reaching the crest.

Figure 4-7 shows two phase averaged data sets, one for the swimming case and one for the non-swimming case. The two profiles are non-dimensionalized by the frictional velocity found from the slope of the velocity near the wall. The data here is phase averaged over 5 runs. The swimming case clearly extends the laminar region compared to the non-swimming fish indicating laminarisation of the boundary region. The curvature of the fish body at this position, position four, is slight in the case of the non-swimming fish.

Figure 4-8 shows the boundary layer profiles one point in the swimming cycle at the fourth position along the fish as shown in figure 4-3. In this plot, data from both an upstroke (compression) and downstroke (dilation) are shown. As a reference, the Blasius solution for flow over a flat plate is also shown by the straight line. The effect of the tail motion on the shape of the boundary layer profiles is evident.

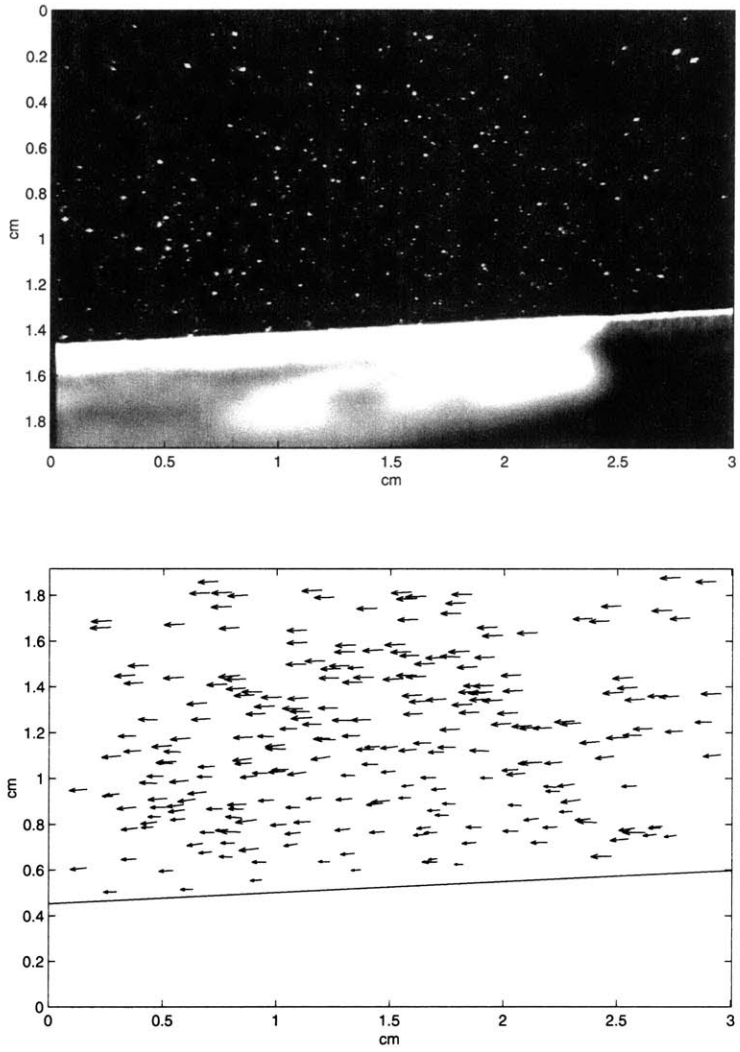

Figure 4-4: Top figure shows typical particle field captured near the edge of the fish body. The lower image displays the PTV velocity field, the straight line represents the location of the body boundary.

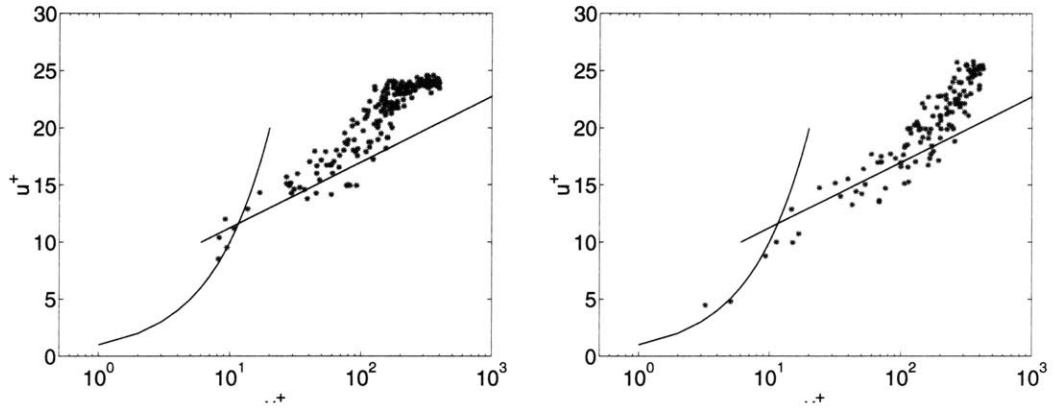

a. Position #1

b. Position #2

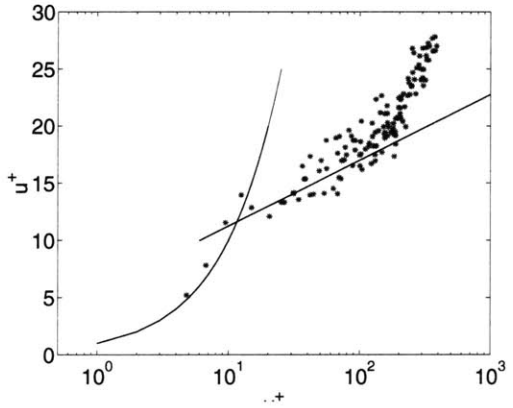

c. Position #3

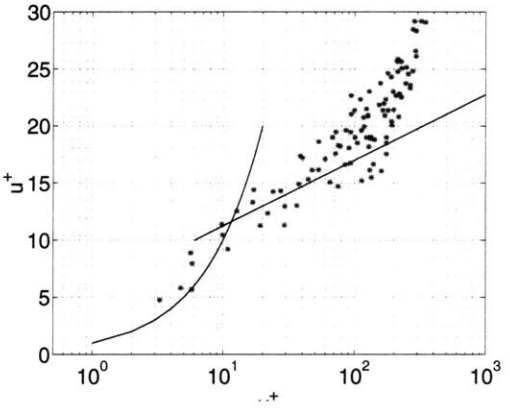

d. Position #4

Figure 4-5: Boundary layer profiles from the non-swimming (straight drag) case at the four positions (along the fish. '-' = theoretical boundary layer profile, $u^+ = y^+$ (lower curve) and $u^+ = 2.5ln\ y^+ + 5$ (upper curve). '*' is the experimental data. $R_L = 800,000$.

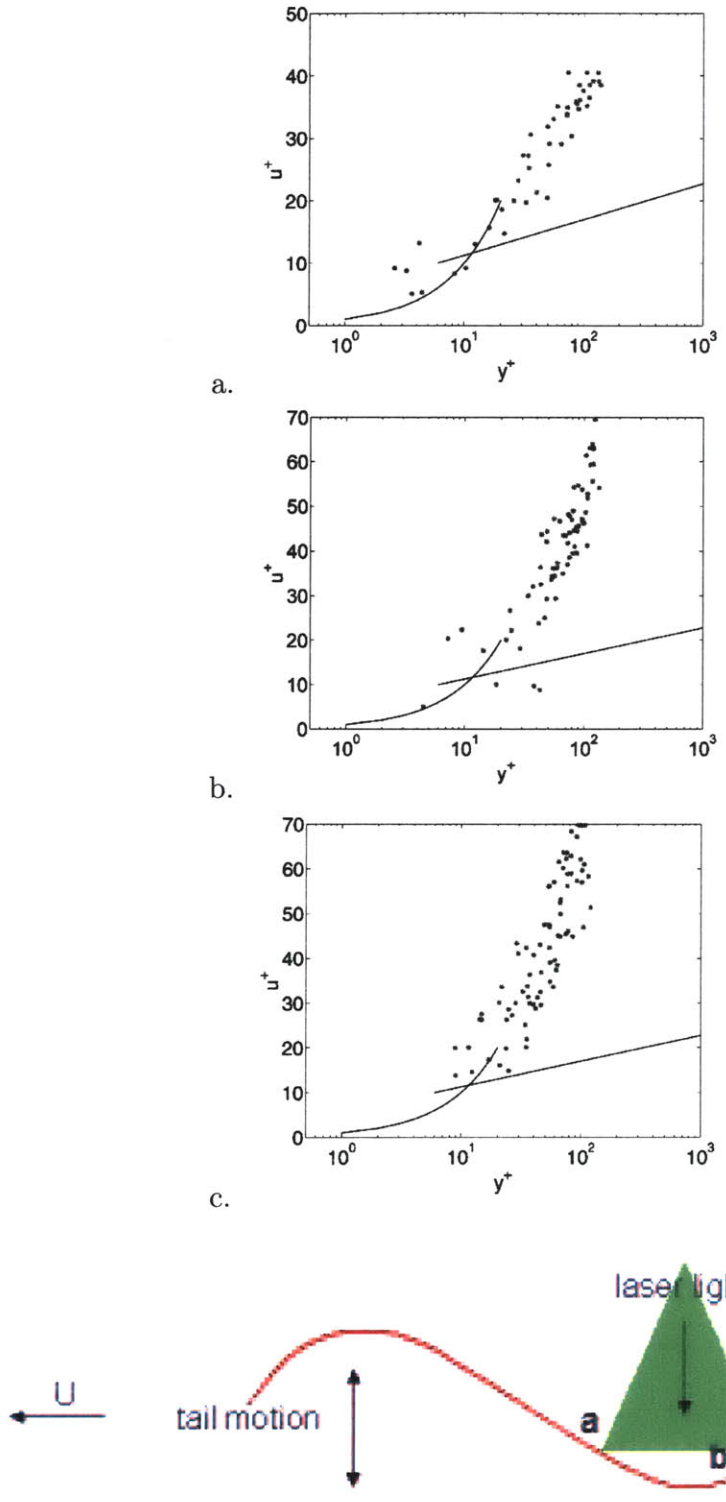

Figure 4-6: Boundary layer profiles for the swimming *RoboTuna* obtained from PTV data at position #4 at three different phases. $R_L = 800,000$.

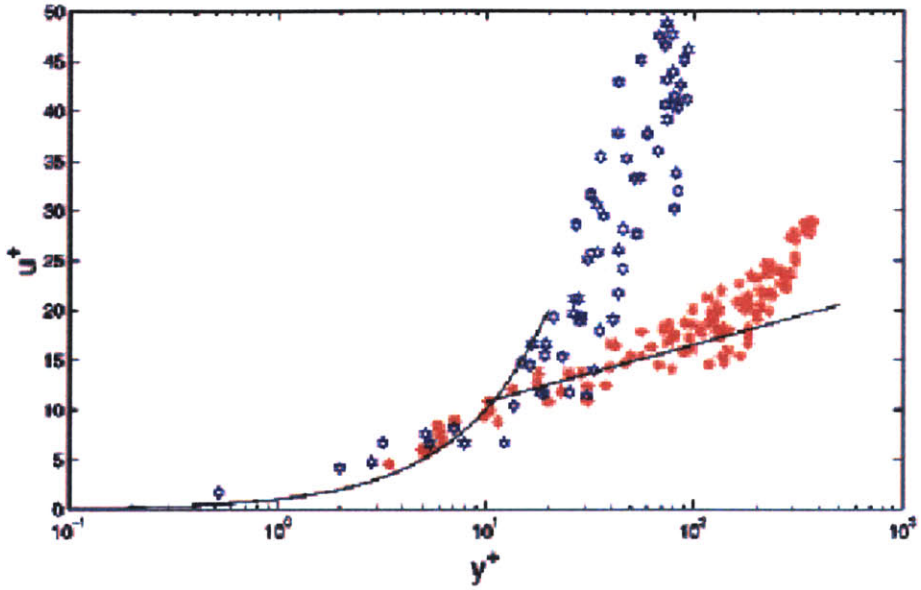

Figure 4-7: Comparison of two boundary layer profiles from the PIV tests about the *RoboTuna*. The red data represents the non-swimming case and the blue the swimming case. The data is non-dimensionalized by the frictional velocity found from the slope of the velocity near the wall. The data here is phase averaged over 5 runs.

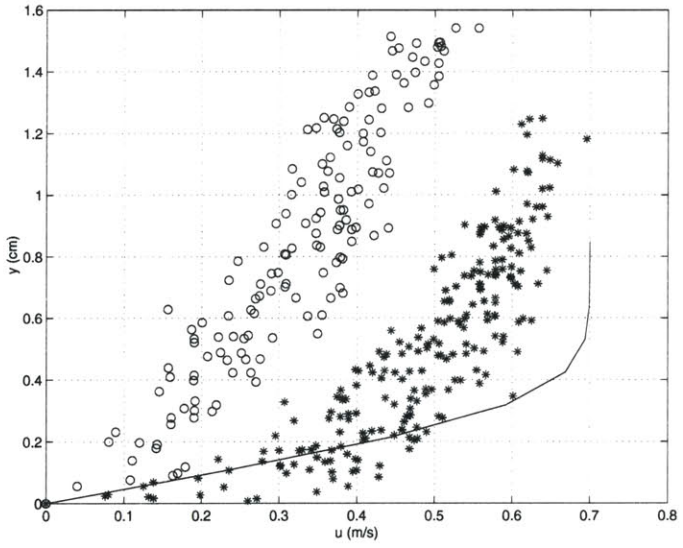

Figure 4-8: Boundary layer profiles for the swimming *RoboTuna* obtained from PTV data at position #4. The curve shown corresponds to the Blasius solution for flow over a flat plate. 'o' is the experimental data for the fish tail moving towards a trough (dilation) and '*' is data obtained when the tail is moving up towards a crest (compression). $R_L = 800,000$.

4.4 Discussion

Several reasons for the apparent drag reduction of the robotic fish have been presented (Barrett, *et al.* 1999, Wolfgang, *et al.* 1999). This study begins a look into the idea of boundary layer manipulation as a mechanism for drag reduction. Boundary layer turbulence suppression was observed by [48] for flow over an undulating boundary where the traveling wave speed was greater than the oncoming flow speed. Here, while a traveling wave is sent down the body, the swimming of a three dimensional body, versus a waving flat plate, can yield similar yet slightly different results.

It is important to keep in mind that this problem, while similar to that of a waving two dimensional plate, is complex in nature. Both the swimming motion of the body and the flapping effects of the tail are essential to the propulsion of the fish. The tail fin motion acts to suction the flow towards the tail which in turn must affect the boundary layer. The visualization performed in these tests were far enough forward on the fish body that the cross section had not begun to taper significantly, but three-dimensional effects can also play a role as the flow nears the region where the tail necks to a small cross-section just before the tail, the caudal peduncle.

Further investigation of the boundary layer is needed to better understand the complex flow phenomenon around the fish. Experiments along the entire moving section of the robotic body are needed to fully understand the implications of the swimming motion.

Chapter 5

Design of a Waving Plate Apparatus

In order to study the near-body hydrodynamics around a waving plate, an apparatus was designed and built to be used in the hydrodynamics tunnel at MIT. The apparatus is an eight link piston-driven system, similar in concept to a straight-eight car engine. The machined parts were all made by the MIT Central Machine Shop or me. Much effort went into the construction and this chapter can merely relay the specifications and design features of the apparatus.

5.1 Design

The waving plate is a reinforced neoprene mat actuated by eight pistons to move in the shape of a traveling wave with increasing amplitude. Flow is studied only on one side of the mat, which is opposite to the side where the pistons connect on the top of

the mat. Using the MIT *RoboTuna* [12] and the waving plate in [29] as a guide, two separate backbone shapes were chosen for the waving plate motion. The first shape was capable of amplitudes on the order of the MIT *RoboTuna*. However, since the mat is positioned in the water tunnel closer to the top wall than the bottom, as we are most interested in the flow on the side without the pistons attached, such larger amplitudes caused the mat to billow and flutter due to the constriction of the flow when the trailing edge was at its maximum amplitude of +4", or closest to the wall.

The amplitude of this motion was dictated by

$$A(x) = 0.1 * x, \tag{5.1}$$

where x is distance from the leading edge of the flexible mat. The pistons are spaced five inches apart with the first piston at $x = 5$" and the last piston at $x = 40$". It would be wise to mention here that the leading edge of the neoprene was 5 *inches* aft of the actual leading edge of the support section (this will be addressed below in the discussion of the mat design).

The second mat shape was more similar to [29] with an amplitude

$$A(x) = 0.75/12 * x. \tag{5.2}$$

This smaller amplitude alleviated the flow constriction near the top of the tunnel and resulted in a smooth mat motion. This is the shape that was ultimately chosen for the experiments discussed herein.

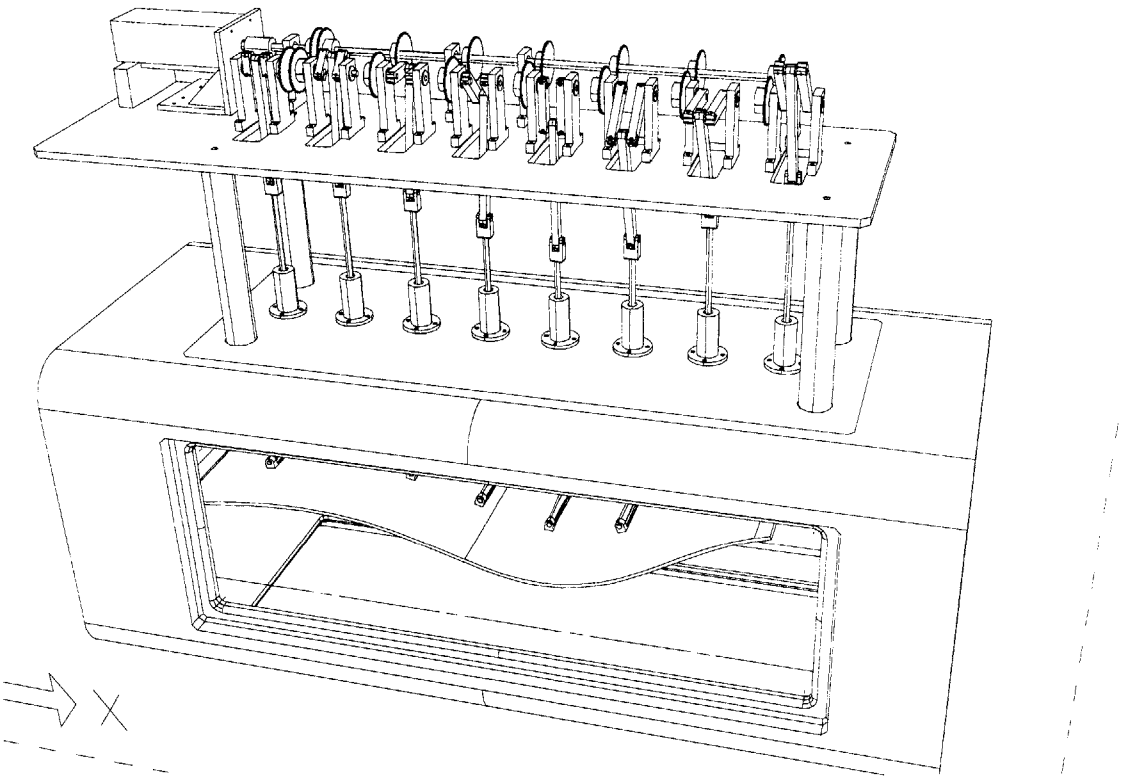

Figure 5-1: Three-dimensional isometric view, created in SDRC I-DEAS MS 7, of the waving plate apparatus within the MIT hydrodynamics tunnel test section. The drive mechanism is elevated 13 inches above the top of the test section and the neoprene mat is inisde the test section centered just above the mid-height of the tunnel.

Mechanical design of the apparatus took into consideration the experimental setups built by Taneda [48] and Kendall [29] but took a slightly different approach the waving plate mechanism. Solid modeling of the waving plate apparatus was done with SDRC I-DEAS before any machining took place in order to assure proper assembly. An isometric three-dimensional view of the mechanism as it fits inside the test section of the hydrodynamics tunnel is shown in figure 5-1. This model illustrates the crank-piston assembly that drives the waving mat.

The eight pistons are actuated by a simple mechanical system driven by a single motor connected to a solid drive shaft. The half-inch diameter drive shaft is attached through a flexible coupling to a 1/3 *hp* DC motor. The Bodine Model 42A7BEPM-5H permanent magnet DC motor is capable of maximum torque loads up to 87 $lb-in$ and speeds up to 140 *rpm*. The motor is controlled by a Bodine DC motor controller. The exact speed of the motor is replicated by dialing in a potentiometer and measuring the voltage with a voltmeter. The speed is repeatable within 0.5 percent.

Along the drive shaft are eight 0.25 *in* pitch sprockets which link the drive shaft to the crank arms that actuate the pistons. Each set of crank arms is individually driven by a 0.25 *in* pitch sprocket of the same diameter on the drive shaft and connected to the drive sprockets with 0.25-pitch metal chain, similar in style to standard bicycle chain. A close-up of the drive train is shown in figure 5-2.

The drive mechanism sits atop an aluminum plate supported over the tunnel window by four aluminum legs. These legs are approximately 13 inches tall and hollow with a wall thickness near 0.0625 *inch*. A threaded rod is screwed into the window plate and placed through the leg. Next the top plate is lowered into place and a lock-washer and bolt are used to sandwich the legs between the upper plate and the window plate. This clock-cage construction is very rigid and also allows for quick disassembly if necessary.

From the top of the pistons, a linkage arm connects to the crank mechanism which controls the mat motion. The link arms are fitted with a needle roller bearing at one end which rolls directly on a 3/8" shaft suspended between the ends of the two crank arms. The length of the crank arms dictate the height of the piston motion, whereas

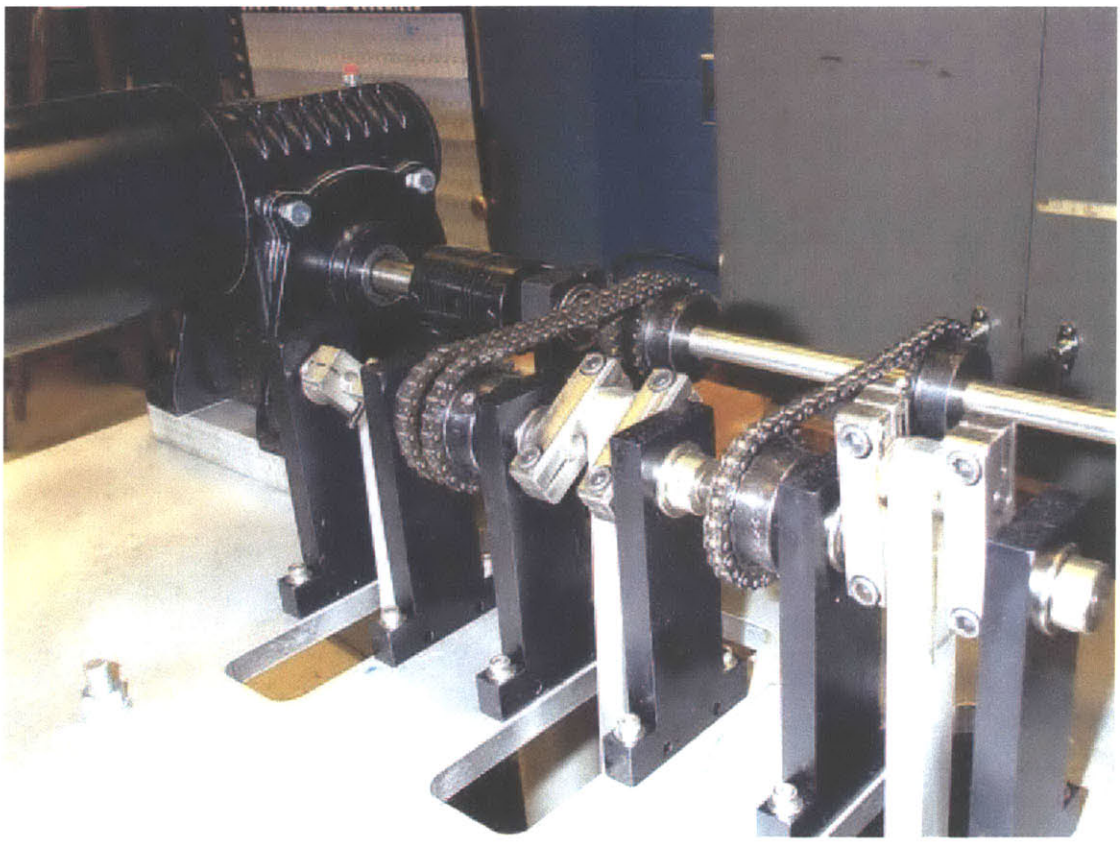

Figure 5-2: Close-up photograph of the drive mechanism. At left is the 1/3 HP DC motor connected to the $1/2 - inch$ drive shaft by a flexane coupling. Each set of crank arms is connected to the drive shaft through a chain-link around equal diameter sprockets.

all of the linkage arms are identical in length. At each end of the crank arms is a $3/8$ *inch* hole and a narrow slot. Through the side of the arm is bolted a $1/4 - 20$ cap screw that is used to tighten the grip on the circular shafts that support the crank arm. A drawing for the first set of crank arms is shown in figure 5-3. The second set of arms follows the same pattern however the lengths, A, B, and C are different since a different amplitude envelope was used. Also for the crank arms used in the actual experiments, the bolt inserted to tighten the arms on the shafts was increased

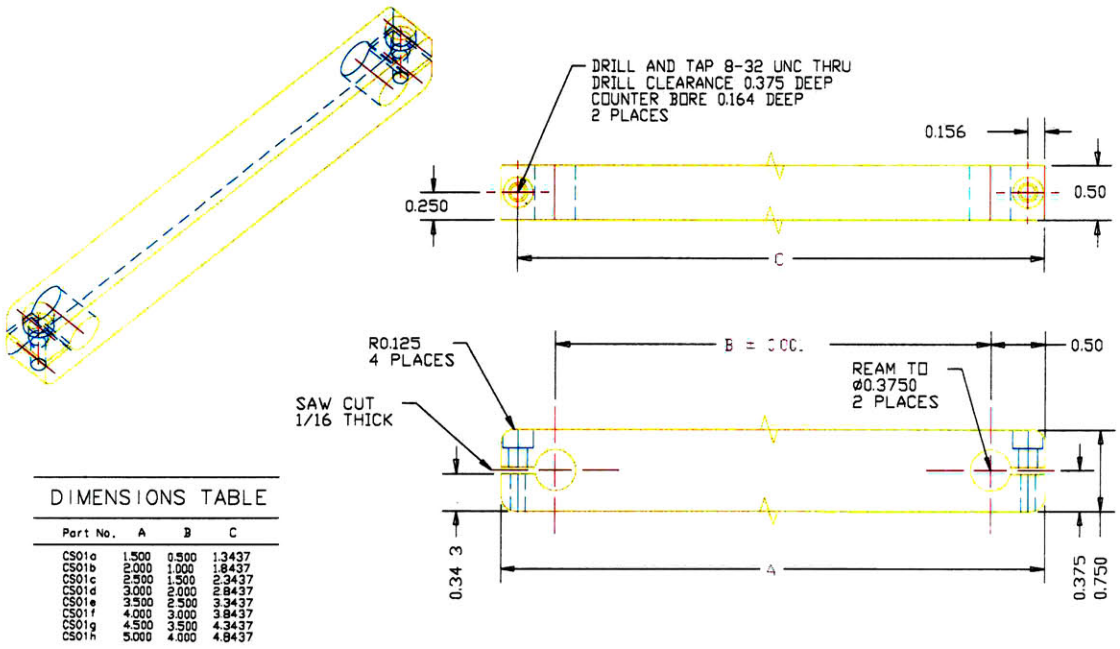

DIMENSIONS TABLE

Part No.	A	B	C
CS01a	1.500	0.500	1.3437
CS01b	2.000	1.000	1.8437
CS01c	2.500	1.500	2.3437
CS01d	3.000	2.000	2.8437
CS01e	3.500	2.500	3.3437
CS01f	4.000	3.000	3.8437
CS01g	4.500	3.500	4.3437
CS01h	5.000	4.000	4.8437

Figure 5-3: Drawing for the crank arm design. Each pair of arms was machined in the same pattern only varying the length of the arm, or more specifically the distance from the center of each hole was larger for each set of pistons from leading edge to trailing edge.

to 1/4-20 in order to gain increased leverage – this required the arms to be redrilled to accommodate the larger bolt.

At the sprocket end of the crank arms another 3/8" shaft is fitted to rotate in ABEC-3 bearings mounted in 4"-high shaft supports. One of the arms is connected to the 0.25-pitch (2" diameter) crank sprockets linked by chain to the drive shaft sprockets. The drive sprockets are the same diameter as the crank sprockets however different sprockets could be attached to change the available torque or speed range of the system, if necessary. The opposite crank arm is supported in a second bearing and capped with a shaft collar to prevent the support shaft from slipping. Details of the linkage system are shown in figure 5-4.

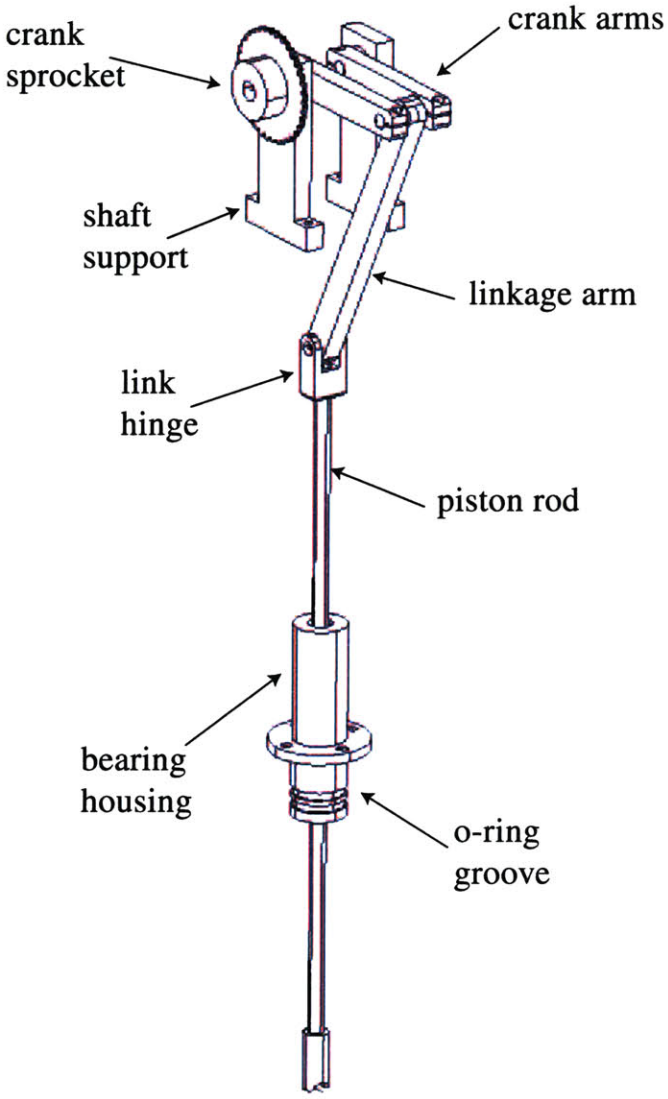

Figure 5-4: Piston linkage mechanism from top to bottom: vertical stand-offs support the pair of crank arms; at the top of the crank arms a shaft connects one side to the crank sprocket, the other end of the arms connect to the linkage arm; at the lower end of the linkage arm at hinge joint is attached, connecting the link-arm and the piston rod; the piston rod travels through the two linear bearings seated inside of the bearing mount shown halfway along the piston rod; the bottom of the rod is connected to the neoprene mat.

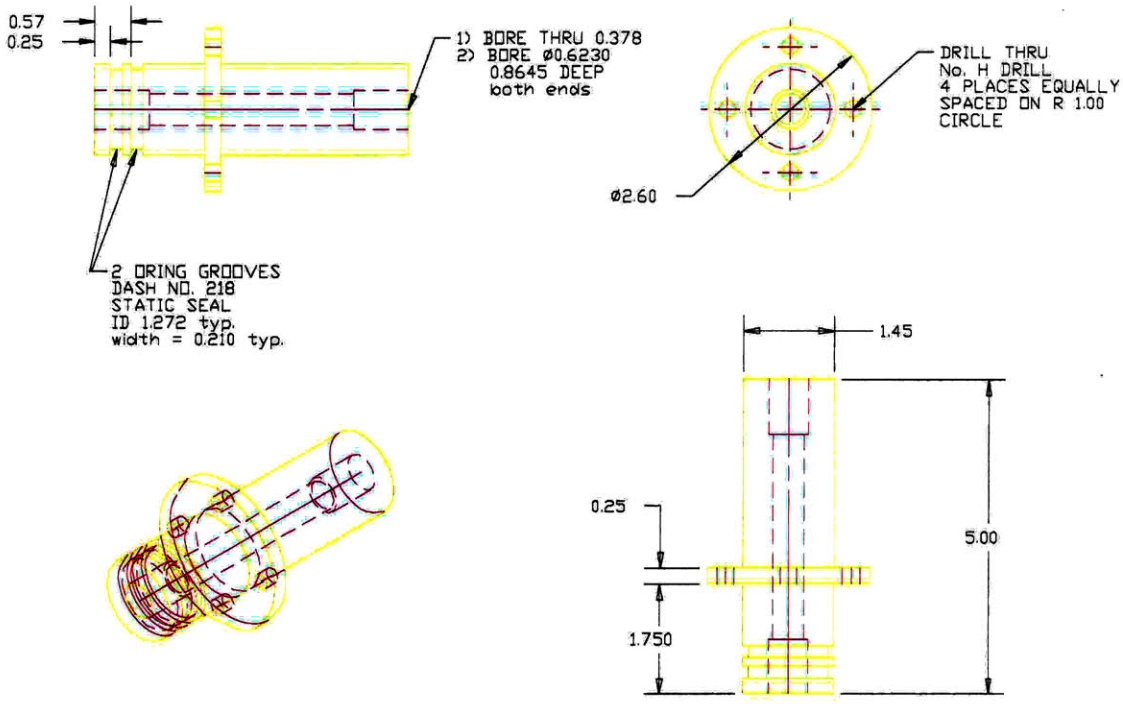

Figure 5-5: Drawing of the linear bearing housing. Clockwise from top left: side view A, top view, side view B (this is the actual orientation of the piece), and isometric view. The material is aluminum and the frelon lined bearings fit one at each end. The flange acts to secure the housing to the base plate. All dimensions are in inches.

The pistons are 5" apart and guided through the tunnel window by two Frelon lined linear bearings housed in an aluminum mount which seats into the aluminum window plate. The bearing housing, seen in figure 5-5, is machined with two o-ring grooves around the outside and seats for the linear bearings at each end. A circular flange is welded around the middle with four bolt holes evenly places around the flange. The flange acts to secure the bearing housing into the base plate and the four bolts must be tightened alternately such that the piston does not bind.

There is no seal around the piston itself. The only leakage experienced was the small amount of water that seeped out with the motion of the pistons through the bearings. This water amounted to a few teaspoons of water per day and was thus

not a concern. A small space under the bearing mount, machined in the base plate window, would allow for the insertion of an o-ring were it necessary. This o-ring was omitted in order to reduce the friction on each piston. Towards the end of the experiments the bearing lining began to wear and the leakage became greater, but the amount of water lost was never a concern.

The window itself is a two inch thick aluminum plate that was machined to fit exactly in the tunnel window opening (see figure 5-6). The aluminum window allows the eight pistons to pass through into the tunnel and also would make it easy to modify in the future if necessary. Any material could have been used here however aluminum was the easiest to machine and weight was not an object. It would have been ideal to have the window anodized before installing it into the tunnel to prevent corrosion, but this was not done.

Attached at the bottom of the pistons, inside of the tunnel section, is the mat. The rods are connected to the mat such that the mat will not be required to stretch over one cycle of motion. There is a cross rod, perpendicular to both the piston and the inflow, that has dual purpose to strengthen the mat and to allow angular rotation of the mat relative to the vertical piston. The cross rods and pistons are connected by a stainless steel welded tee which fits snugly on the end of the piston rod and has two Rulon-J bearings in which the cross-rod is allowed to rotate.

At either end of the cross-rod are two delrin sliders. These sliders allow the mat to change length as required by the motion. This change in length is dictated by simple geometry. As two adjacent pistons rise or fall, one out of phase with the other, the arc length of the section of mat between these two rods changes. Since there are

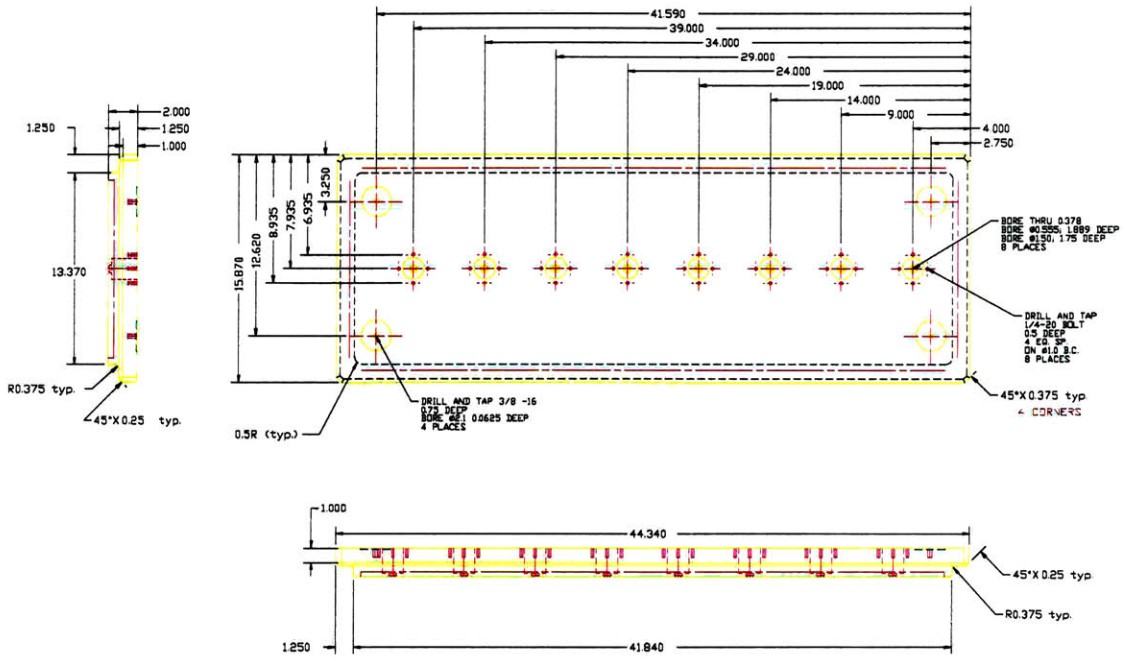

Figure 5-6: Machine Drawing for the mechanism base plate; top and side views. The master is a copy of the existing window design modified such that the eight bearing housings can be mounted and the top plate can be stabilized.

eight rods in synchronous motion, the arc length of the mat must also change with a cumulative effect from stem to stern. Thus the length of the slots change, get longer, from piston one to piston eight. The cross rods are guided in the slots by shoulder bolts and small stainless steel springs help the cross-rods return to a neutral position and allow the mat to move smoothly.

The actual mat is made from 1/4" thick, high-grade Neoprene sheeting. It is reinforced with square, hollow brass rods which are glued to the surface with compliant rubber cement. A close-up of the construction design is shown in figure 5-7. The bond is made more secure with a fillet of clear silicone RTV and a bolt at each end to prevent the rods tearing off. The bolts at the end are 100° flat head screw which are flush with the surface on the flow-side of the mat. Ultimately it might have been

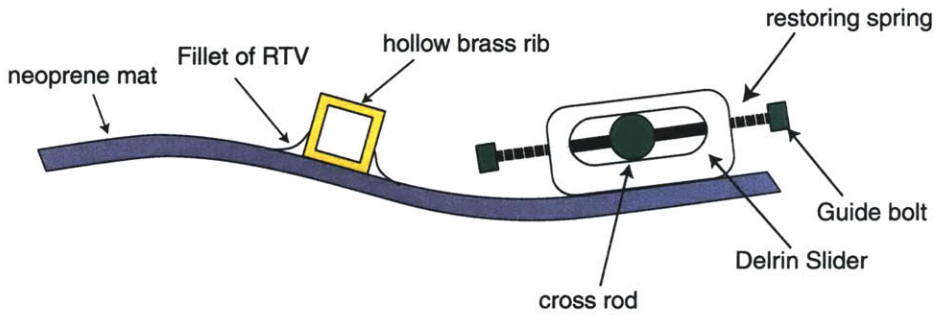

Figure 5-7: Mat construction includes 1/4" hollow brass square rods that are adhered to the neoprene mat and act to stiffen the mat transverse to the flow. The delrin sliders allow the mat to change length as it undulates.

wiser to use a thicker neoprene sheet, say 3/8" thick, as it might have lasted longer and lent more stiffness to the apparatus allowing higher testing speeds. Again this design was sufficient for the purpose of this investigation.

The leading edge of the rubber mat is attached to an aluminum support. This support is made from a half-inch thick, horizontal aluminum plate, with a rounded, smooth leading-edge, that spans the width of the test section. This bottom plate is welded to two NACA 0012 shaped, vertical foil sections and a smaller horizontal plate on top of the foil sections that has two tapped holes that allow the leading edge support to be firmly bolted into the test section with 1/2-13 hex head bolts. This allows for a five-inch, flat, smooth plate, with a rounded leading edge, to split the incoming flow just before the mat and zero motion at the leading edge of the rubber. Since the holes in the tunnel used to bolt the leading edge in securely are thru-holes, the bolt heads must be sufficiently covered in RTV to prevent the leakage of fluid through this opening. Often hasty attempts at sealing the bolts lead to excessive water leakage and required draining and re-caulking the bolts.

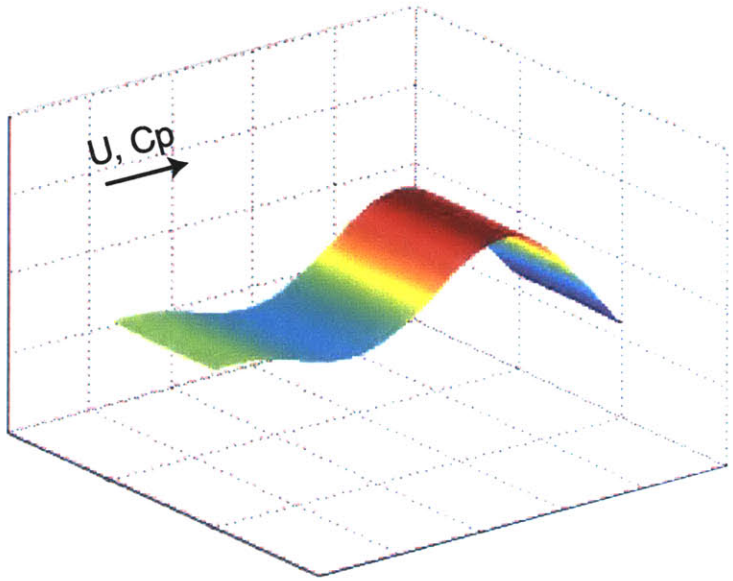

Figure 5-8: The waving plate moves as an increasing amplitude sinusoid.

5.2 Wave Mechanics

As discussed previously, the traveling wave shape is an increasing amplitude sinusoid. The traveling motion is created by an angle offset between each set of crank arms. Each crank arm is adjusted so that it is a set angle from the previous crank arm. This offset results in a wavelength, λ, that was 0.8 times the length of the mat, L ($L = 1.25 * \lambda$). Since the total length of the mat, including the leading edge plate and the trailing edge extension beyond the 8th piston, is 49" (or 1.25 meters), $\lambda = 1.0\ meters$. The motion of the mat, using the equation for the amplitude found in 5.2, is

$$y(x) = A(x) * \sin(k * x - \omega * t), \tag{5.3}$$

where k is the wavenumber, $k = 2 * \pi/\lambda$, ω is the piston frequency in radians, and x and t are the distance along the mat in meters and the time in seconds, respectively.

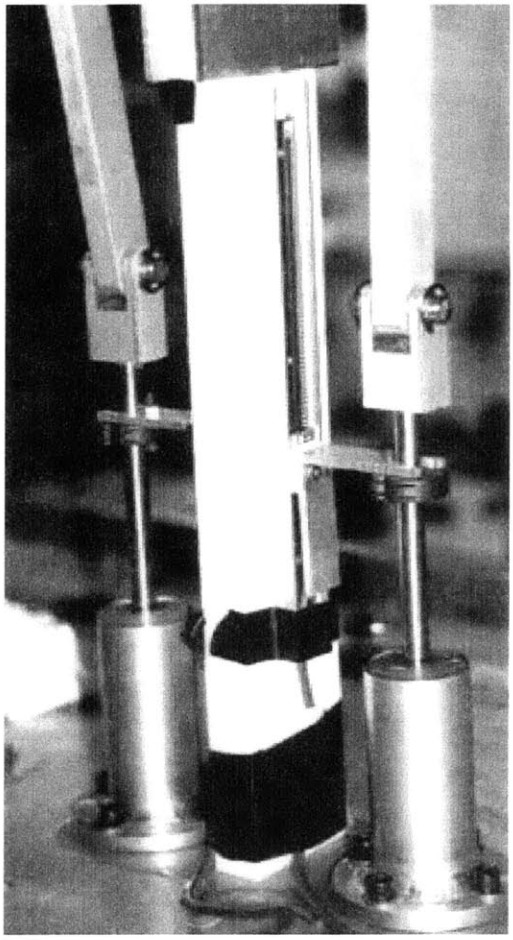

Figure 5-9: Linear motion potentiometers connected at pistons 5 and 6 measure the frequency and relative phase of the motion.

The phase speed, C_p, of the mat can be deduced from simple wave theory and written as

$$C_p = \omega/k = 2\pi f/2\pi/\lambda = f\lambda. \tag{5.4}$$

The frequency of the wave is dictated by the piston motion and thus is intrinsically linked to the speed of the motor. The addition of the linear motion potentiometers (LMP's) alleviated the need for a motor encoder to deduce the motion frequency (see figure 5-9). The frequency of the piston motion was recorded by the DasyLAB data

acquisition software on a Computer Boards DAS16 Jr. card wired to measure 16 channels single-ended. The LMP signals were processed in Matlab prior to each run to ensure repeatability in the motion. The frequency of motion was correlated with the motor controller potentiometer output voltage to ease setup. Frequencies were chosen based on the ratio of phase speed to free-stream flow. Five such ratios were chosen:

$$\zeta = C_p/U_o = 0.3, 0.6, 0.8, 1.2, 1.4. \tag{5.5}$$

Using equation 5.4 the requisite frequency is thus $f = \zeta U_o/\lambda$.

A discussion of the experimental setup and hydrodynamics tunnel characteristics are presented in the following text. The results from the LDV and PIV experiments are discussed in the following chapters.

5.3 Experimental Setup for LDV

At this point it would be advantageous to discuss the facility used for the waving plate experiments. Tests on the waving plate apparatus are performed in the MIT Hydrodynamics Lab. The lab has a re-circulating water tunnel that was designed originally to test propellers. It has a square test section that is 0.5 m x 0.5 m in cross section and 1.14 m long. The tunnel is capable of sustaining flow speeds up to 10 m/s (33 ft/s). Figure 5-10 illustrates the entire facility.

The tunnel spans the height of two floors with the holding tank for the water, and the impeller machinery, on the lower floor and the test section, and controls, on the

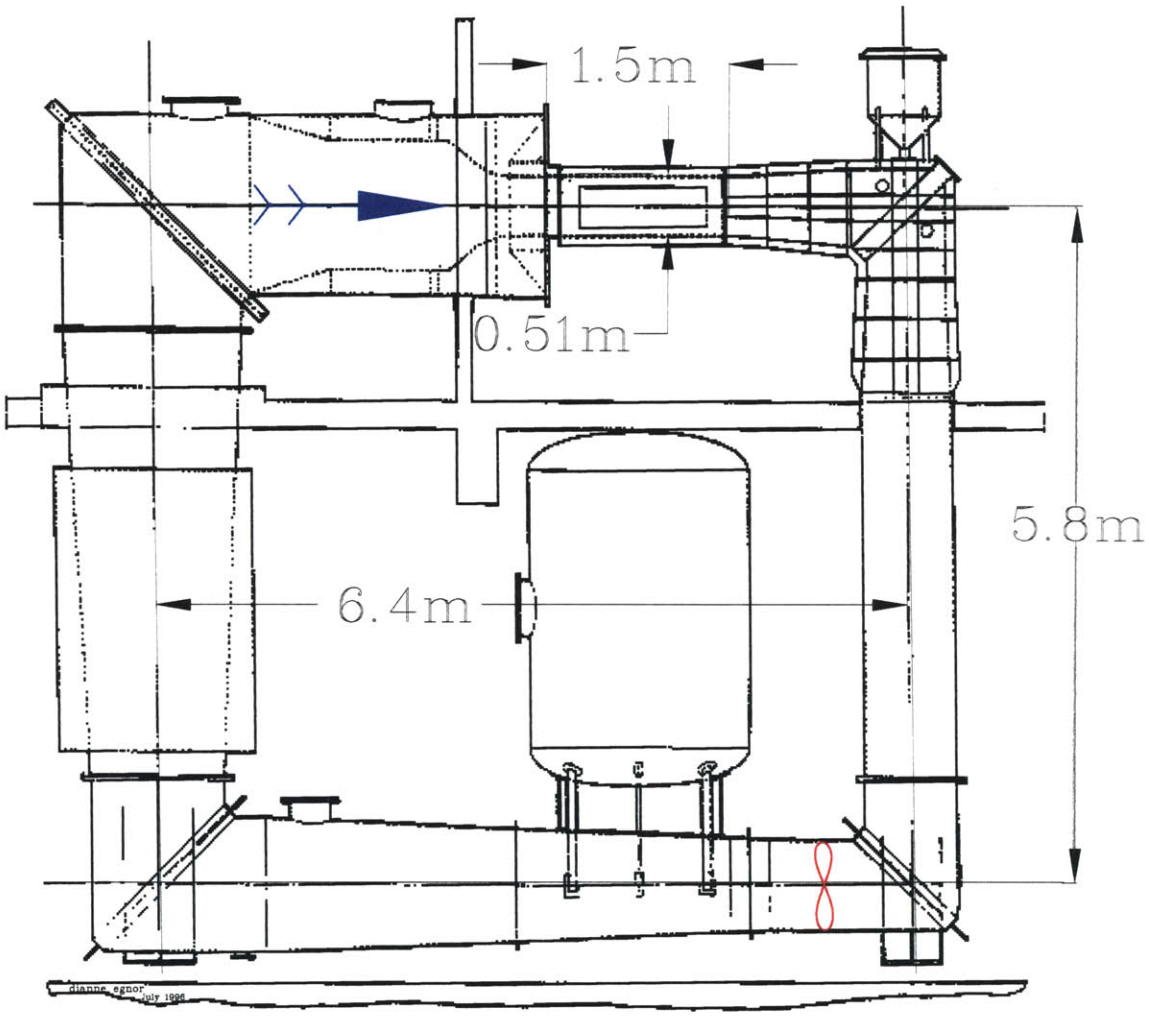

Figure 5-10: A schematic of the MIT hydrodynamics (propeller) tunnel. The tunnel spans the height of two floors with the holding tank for the water and the impeller machinery on the lower floor and the test section in lab on the upper floor. The test section is approximately at eye level.

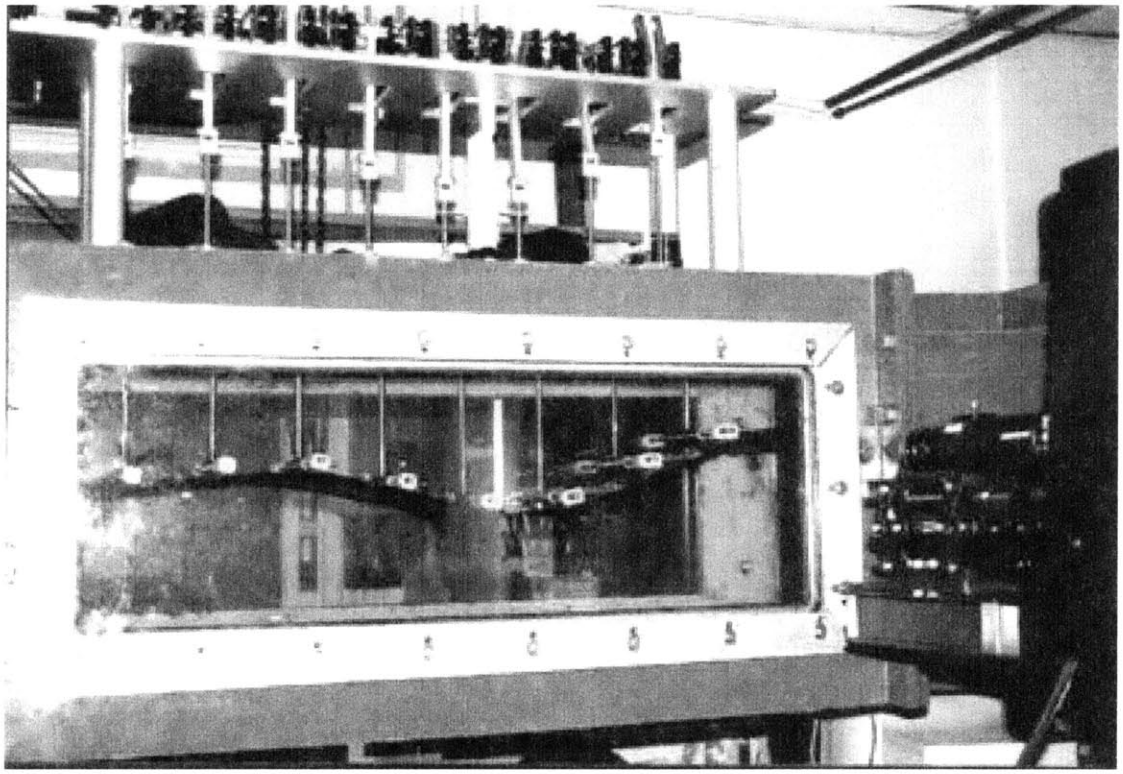

Figure 5-11: Photograph of the Waving plate apparatus atop the hydrodynamics tunnel. The waving mat can be seen through the side window. Flow in the tunnel is from left to right.

upper floor. The test section is approximately at eye level. The drain and fill controls are on the far side of the tunnel from the impeller speed controls. The flow direction is indicated by the arrow in figure 5-10 and is from left to right in the top section of the tunnel. A photograph of the apparatus atop the test section is shown in figure 5-11. On all four sides of the test section is a removable window that allows access to the inside of the tunnel. The top opening in the test section is fitted with the base of the waving plate apparatus. The bottom window is a clear, laser-quality (nearly perfect parallel faces with minimal scratches) polycarbonate window. The front window (on the traverse side) is another laser-quality window, and the rear window is covered on

the outside by thick black cloth to prevent the light from reflecting off the wall of the room and also for safety. It was found that minor scratches in the window could be easily avoided.

Chapter 6

Laser Doppler Velocimetry Measurements of the Flow About the Waving Plate

This chapter presents the results from Laser Doppler Velocimetry tests about the waving plate moving at different frequencies for speed $U = 1.0\ m/s$. The RMS turbulence in the tunnel at flow speeds of $1.0\ m/s$ are about 2-3%. Data was obtained for several mat wave speeds from $Cp = 0.3$ to 2.0 times the freestream velocity. The non-dimensional ratio, $\zeta = C_p/U_o$, is used most often to describe the wave speed parameter. LDV data reveals a significant reduction in turbulence intensities at some distance from the wall as phase speed ratios, $\zeta = C_p/U_o$, increased past 0.3 to 1.2; beyond $\zeta = 1.2$ the local turbulence intensity no longer decreased.

6.1 Laser Doppler Velocimetry Setup

Back-scattering Laser Doppler Velocimetry (LDV) was employed to capture phase averaged velocity measurements of the flow about the waving mat in the hydrodynamics tunnel. The existing LDV system consists of a 6-Watt Argon Ion laser and optics by TSI, Inc., and the optics are fixed on an optical table mounted on a traverse. This limits the orientation of the two beam pairs to horizonal and vertical planes, measuring U and V velocity in global (tunnel) coordinates. Here a modern fiber probe would have proved useful since we were limited to measuring the flow at some distance from the mat.

The data acquisition system from Dantec allowed for u- and v-velocity data to be recorded and ordered in angle bins averaged by phase over 360 degrees of mat motion for one fixed point. The system operated in burst mode at data rates up to 180 Hz and in dead time mode, used for the data presented here, the data rate reduced significantly to a maximum of 80 Hz. Data rates varied depending on the flow speed, almost doubling for the 1 m/s case over the 0.5 m/s runs. With both U and V channels active, the LDV system allowed for data to be acquired only at a time when both U and V components were deemed to be valid thus the significantly lower data rates than if only the U-component was measured. On average a data rate between 60 and 100 Hz was easily obtainable at sufficient distances from the mat (≈ 4 $mm+$ away from the mat). Data rates were significantly improved with denser seeding, as expected.

For the experiments at fixed x/λ, the laser was positioned at several points down-

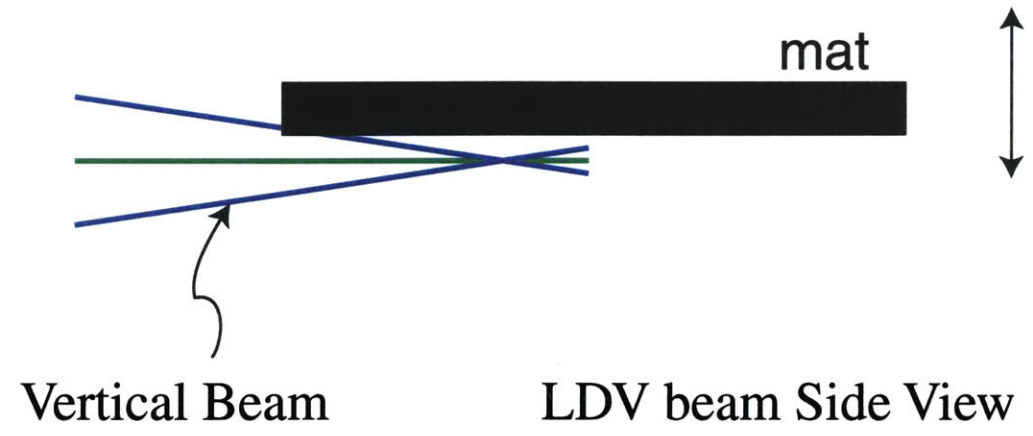

Figure 6-1: Clipping of the vertical LDV beam measuring the v-velocity component is shown. Beam crossing was located 1/3 distance in from side wall of the test section, well out-side the tunnel side-wall boundary layer.

stream of the leading edge. Data was taken along vertical cuts, from the top extreme of the mat to just beyond one *cm* below the mat's lowest point of travel, every few centimeters with U-component only and then again every 4 *mm* with U and V channels both turned on.

Since the V-component is measured at the intersection of two beams aligned in the vertical plane, there is significant clipping of the upper beam very near to the mat (see figure 6-1). The beam crossing was located 1/3 of the mat width in from the front wall, well outside of the tunnel boundary layer, in order to minimize the vertical distance of the measurement point from the waving mat. The closest possible distance from the boundary was 4 mm, figure 6-2. For the phase angles where the mat interferes with the vertical beam no data is acquired.

Data binning was aided by a inductance pick-up encoder attached to the drive shaft which indicated the start of a mat cycle by a short pulse ($< 0.5ms$ duration).

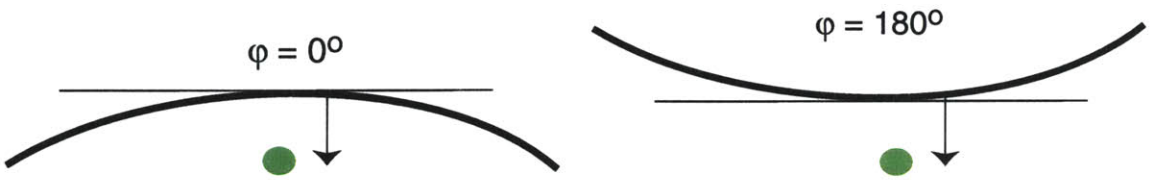

(a.) (b.)

Figure 6-2: Closest beam crossing point is located a distance away from the mat such that beam clipping is minimized. The closest measurement point is 4 mm. Data is obtained in the mat trough (a) and under the crest (b).

The Dantec software used the encoder pulses to order the raw data in angle bins from 0 to 360 degrees and then phase averaged over each bin. The total number of data samples was specified in order to obtain approximately 300 samples per bin. Both raw and processed data were retained. Later data processing was performed to remove data outliers beyond three standard deviations. The $x - y - z$ traverse allowed a vertical cut of data, at a fixed x and y position, to be taken at any point along the mat length and for the baseline velocity data a horizontal data cut at a fixed y and height z.

Data averaging was performed for data within one degree, for example bin 180 contains data from 180.00 to 180.99. Statistical means and variance was calculated, and outliers beyond 3σ were removed. The maximum number of available samples was used in each case. For the data sets presented, at least 200 samples are included in each average. From figure 6-3

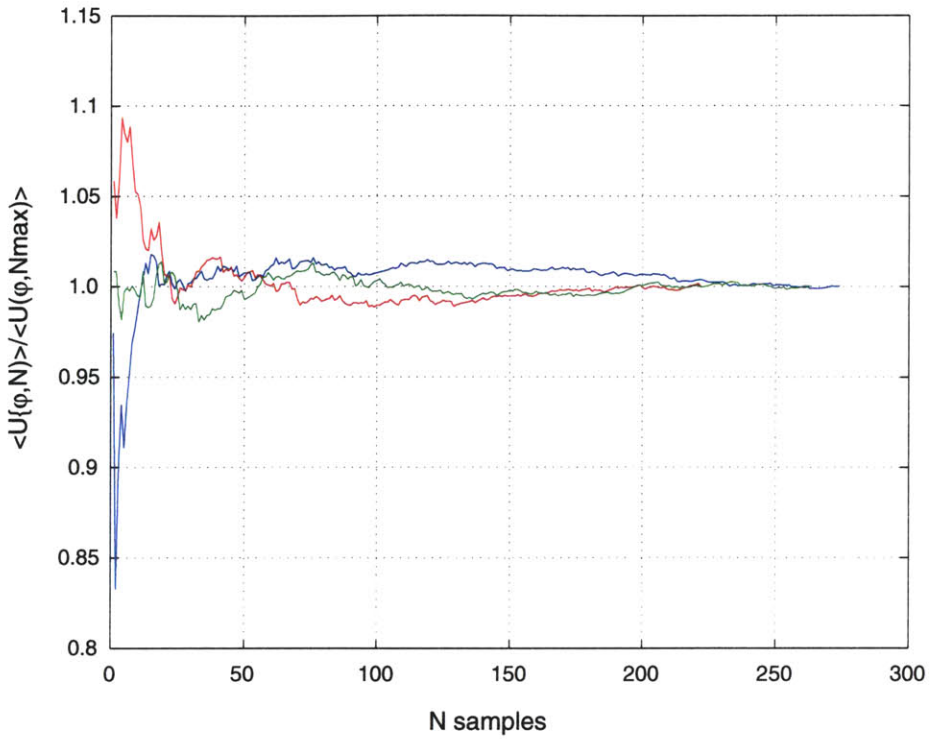

Figure 6-3: Effect of Sample size on LDV mean statistics. Three separate angle bins are shown for one case at $\zeta = 1.2$. Green is taken at the crest position for phase $\phi = 0°$, blue at the crest for phase $\phi = 180°$ and red at the trough for phase $\phi = 0°$. $< U(\phi, N) > / < U(\phi, N_{max}) >$ shows convergence to the average of the maximum sample size of $N_{max} = 250$.

6.2 Baseline Velocity Measurements

Flow data was obtained along the bottom of the test section using LDV with the mat moving. This data was acquired along a path located a set distance below the the waving mat at increasing distances from the leading edge of the mat. The LDV was located as near to the bottom edge of the clear window as possible. This was well outside of the tunnel boundary layer. The x positions were taken from 0.2 m to 1.0 m aft of the leading edge. Again, the phase bins are synched with the 5th piston such that $\theta = 0°$ is top dead center of piston 5 and $\theta = 180°$ is bottom dead center.

Two phase speed ratios, $\zeta = 0.6$ and 1.2, were measured for phase averaged

velocity data. The magnitude of the mean U component is plotted in figure 6-4 and the V component in figure 6-5. It is obvious here that the effect of the mat is still evident at the tunnel walls. The U velocity is highest at the point of maximum constriction and lowest at the point of maximum expansion as would be expected. However this effect is lower in magnitude and phase shifted aft for the higher phase speed case.

These baseline velocity measurements indicate a non-uniform pressure gradient present in the outer flow. The magnitude is lower for the higher phase speed, as if there was less effect due to the wave presence. This external pressure wave will effect the flow at the mat. This is caused by the close proximity of the mat to the tunnel walls. Since the mat spans the entire tunnel, and the seepage around the mat sides is minimal, the flow acts as if it is traveling through a series of constrictions and expansions.

Turbulence statistics are calculated from the baseline data to asses the phase dependence on these quantities. In figure 6-6 the normalized turbulence energies are plotted as a function of angle bin for the lowest frequency. These values result from the standard deviation of the velocity about the phase averaged value. Outliers beyond three standard deviations are neglected. These statistical quantities are phase averaged quantities, $\overline{u'^2}$ and $\overline{v'^2}$, divided by the squared inflow velocity. Note that there is little phase dependence on this data, unlike the average data shown in the previous plots. Here data is plotted corresponding to $x/\lambda = 0.4$ (left) and 0.7 (right).

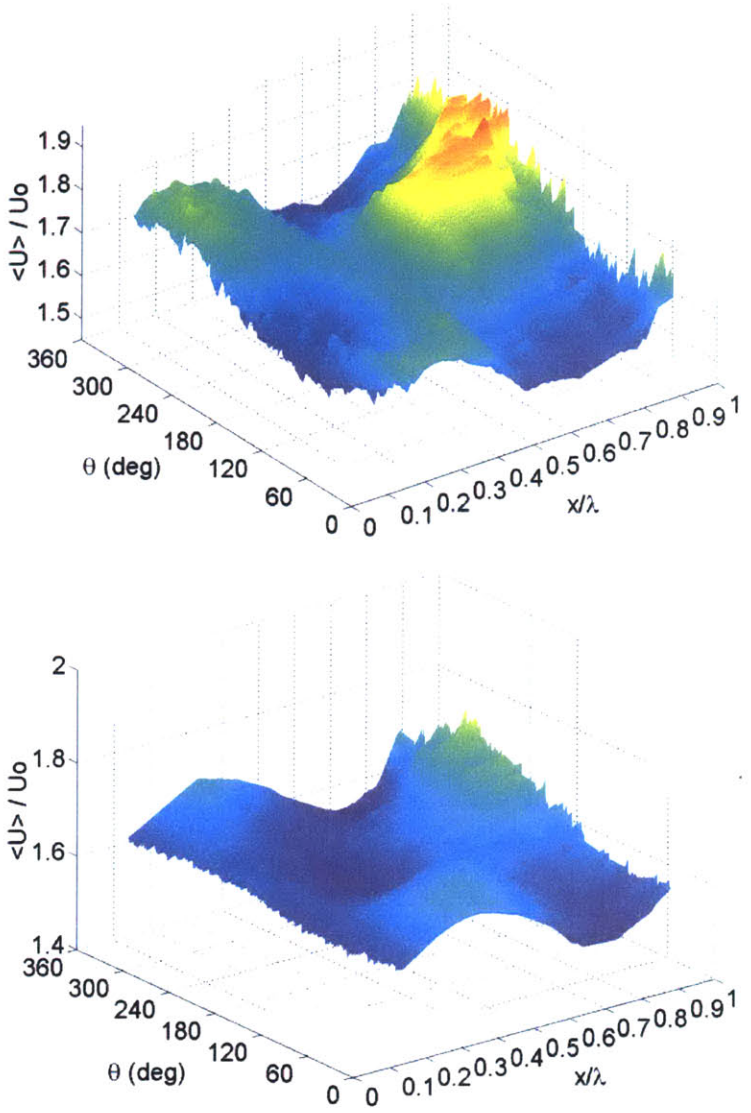

Figure 6-4: LDV bin averaged results for the U-component of velocity acquired. along the bottom of the tunnel, outside of the tunnel wall boundary layer. The phase angle corresponds to the position of piston #5. When $\theta = 0°$ a trough is located under piston #5, when $\theta = 180°$ there is a crest at piston 5. Red areas indicate high velocity and blue lower velocities. Many lengthwise stations (x/λ) were sampled.The top image is for $\zeta = 0.6$ and the lower figure for $\zeta = 1.2$.

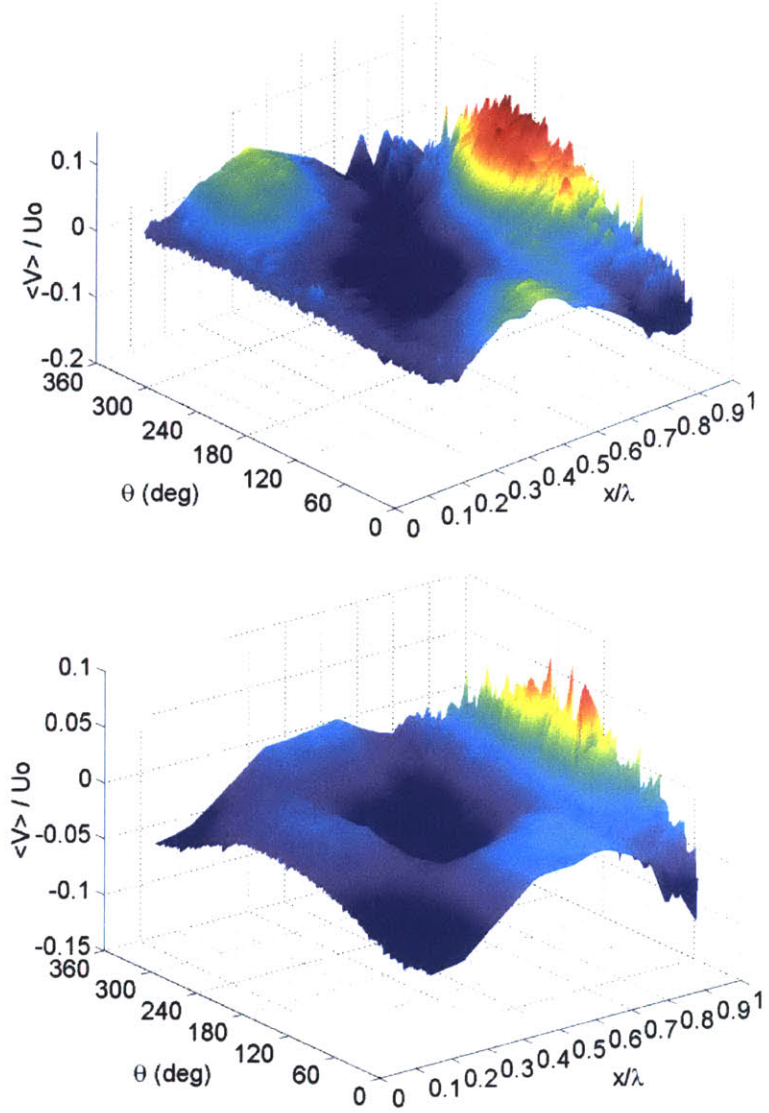

Figure 6-5: LDV bin averaged results for vertical velocity acquired along the bottom of the tunnel, outside of the tunnel wall boundary layer. The phase angle corresponds to the position of piston #5. When $\theta = 0°$ a trough is located under piston 5, when $\theta = 180°$ there is a crest at piston 5. Red areas indicate high velocity and blue lower velocities. Many lengthwise stations (x/λ) were sampled.The top image is for $\zeta = 0.6$ and the lower figure for $\zeta = 1.2$.

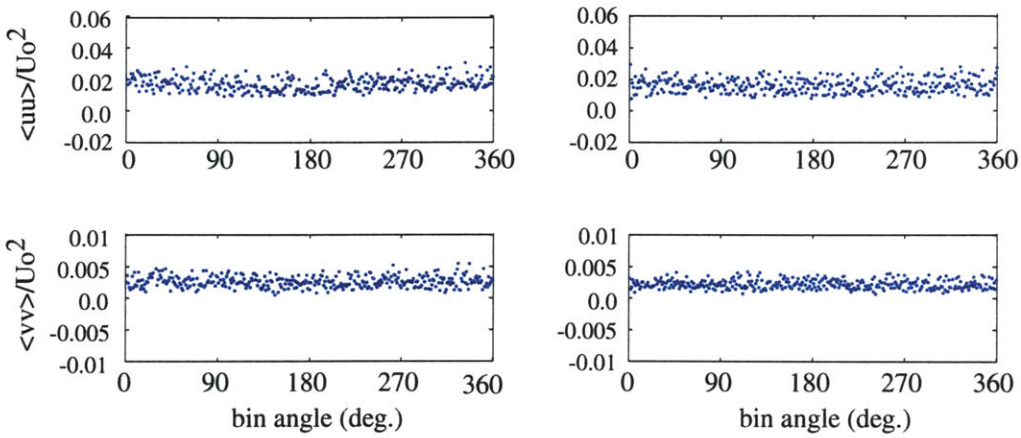

Figure 6-6: Turbulence statistics at two lengthwise baseline stations, $x/\lambda = 0.4$(left) and 0.7 (right), under the waving mat for $C_p/U_o = 0.6$.

6.3 Results of LDV Tests at $x/\lambda = 0.635$

Tests were first performed under piston #5 and the inductance pickup recorded a 0° phase angle when piston 5 was fully vertical (in other words, at top dead center) and a 180° phase angle when piston #5 was at bottom dead center, or its lowest excursion point. Since the flow is on the side of the mat opposite the pistons, at a phase angle of zero degrees ($\theta = 0°$) the mat boundary resembles a trough, or a valley, with concave curvature, whereas a phase of 180 degrees ($\theta = 180°$) resembles a wave crest with convex curvature. Phase 90 degrees is a downcrossing point and 270 degrees an upcrossing point.

Initially data was acquired for mat phase speeds between 0.3 and 1.4 m/s, and inflow speed 1 m/s. The individual runs were processed to determine the turbulence statistical data. The fluctuations in U and V were determined after outliers beyond 3σ were discarded. Then these fluctuations were correlated to obtain the turbulent quantities: $\overline{u'^2}$, $\overline{v'^2}$, $\overline{u'v'}$. Herein the phase averaged mean is often denoted by <>

instead of the overline, for example $\overline{U} =< U >$ or $\overline{u'v'} =< u'v' >=< uv >$. In the following figures the fluctuation quantities are notated by lowercase symbols omitting the prime symbol ($'$). The total velocity is $U =< U > +u' =< U > +u$.

Figure 6-7 shows the data acquired under piston #5, $x/\lambda = 0.635$, at 4 mm below the maximum and minimum excursion points (this is the vertical position closest to the mat at which the LDV probe was able to measure the vertical velocity component without beam clipping). Turbulence statistics $< u'^2 >$, $< v'^2 >$, and $< u'v' >$ are shown in the plots from from top to bottom. Red is data at phase angle zero degrees (trough) and blue is at phase angle 180 degrees (mat crest). The two different symbols represent independent runs for the same parameters. The observation of independent runs at the same position revealed high repeatability in the data.

The turbulent quantities are significantly reduced between the observed phase speeds. This is especially obvious in the region of concave curvature where the quantity $< uu >$ decreases at higher phase speeds (up to $\zeta = 1.4$) by over half the value at lower phase speeds ($\zeta = 0.3$). The data obtained at phase $\theta = 180°$ reveals a downward trend as well but not as significant as in the concave region.

The next step was to acquire data at several points away from the maximum excursion points. The traverse system was programmed to step in 2 mm increments starting 4 mm from the maxima, as in the runs previously discussed. This data is plotted in figure 6-8. Here a high degree of variation is seen in these quantities at lower phase speeds, especially in the concave region, than at higher phase speeds. LDV was unable to give a perfectly clear picture of the variation of these quantities away from the boundary, however PIV was performed to observe these effects more

clearly. PIV results are discussed in the next chapter. In this figure the decrease in turbulence is again noted up to phase speeds of 1.4 m/s, or 1.4 times the freestream ($\zeta = 1.4$).

6.3.1 LDV Results at $x/\lambda = 0.826$

As the wave travels down the length of the mat the amplitude of the mat motion increases and so does the local slope, ka. How this effects the separation and turbulence production is of interest since it is expected that for high wave slopes and zero motion flow separation will occur. The local slope of the previous station was $ka = 0.25$ and of this station $ka = 0.325$, thus we could anticipate greater separation at $C_p = 0$ and possibly even small non-zero phase speeds (eg. $C_p/U_o \approx 0.3$).

Again two runs were repeated and plotted for each case. Data was obtained at $\theta = 0°$ and $180°$ based on the average positions of pistons 6 and 7. This station was half way between these two pistons which corresponds to $x/\lambda = 0.826$ and a phase shift of $|\Delta\theta| = 68.7°$ from the first station, under piston 5. Here the data shows reduction in turbulence quantities on the order of the reductions seen at the previous station. This would indicate that the traveling wave motion is still effective in combating separation at this higher wave slope.

6.3.2 LDV at Higher Wave Speeds

Direct numerical simulations by Zhang [65] at lower Reynolds number indicate that as the phase speed increases towards $\zeta = 2.0$ separation appears on the back side of

the wave crest. This would imply an increase in turbulence production and a reversal in the trend reported between $C_p = 0.3$ and $1.4m/s$. However the LDV data up to $\zeta = 1.4$ does not indicate any increase in turbulence levels would exist if the reduction trend continued beyond this phase speed, so further tests were performed to investigate the higher phase speed region.

Tests were again conducted at station one, below piston 5. These tests were conducted for $\zeta = C_p/U_o = 1.6$, 1.8, and 2.0 for inflow speeds of 1 m/s. The resulting data is plotted in figure 6-10 in addition to the data points from the first tests which were shown in figure 6-7. Here it is clear the upward trend in the $\overline{u'^2}$ term as the phase speed passes beyond 1.4 U_o. Indeed evident in this plot is the increase in turbulence energy. The $< u'^2 >$ term clearly reverses its declining trend an becomes increasingly larger as C_p/U_o goes to 2.0.

Now there is also an upward trend noticeable in the data taken at the crest ($\theta = 180°$). While it is still to meet the levels of turbulence in the trough it is higher at $\zeta = 2.0$ than the value at $\zeta = 1.4$. It is good to reiterate the process of non-dimensionalizing the data. For all velocity terms the freestream inflow (calibrated from the tunnel impeller RPM) is used to normalize the data. However at the crest the *local* velocity is significantly higher than the inflow speeds (up to 1.4 U_o depending on phase speed) and in the trough regions the flow is significantly reduced. Again this is illustrated in the plots of baseline velocity data from section 6.2. To normalize with these local quantities would further confuse an already complicated picture.

6.4 Summary

LDV results show a clear change in turbulence levels as the phase speed of the waving mat increases. A region of reduced turbulence intensity exists around $\zeta = 1.0 - 1.4$. This finding is in agreement with numerical simulations. The upward trend in the turbulent energies occurs beyond $\zeta = 1.4$ indicating increased local turbulence at these swimming speeds. Numerical simulations at phase speed twice the inflow speed show separation reappears on the back of the crests which would increase the local turbulence levels. The numerical simulations also show an organization, and reduction, of the turbulence structures along the for increased phase speed. This organizing effect is a possible source for the local turbulence reductions reported herein.

Data of the near field velocity is obtained using PIV as a comparison with LDV. The average velocity profiles and turbulence data is presented in the following chapter.

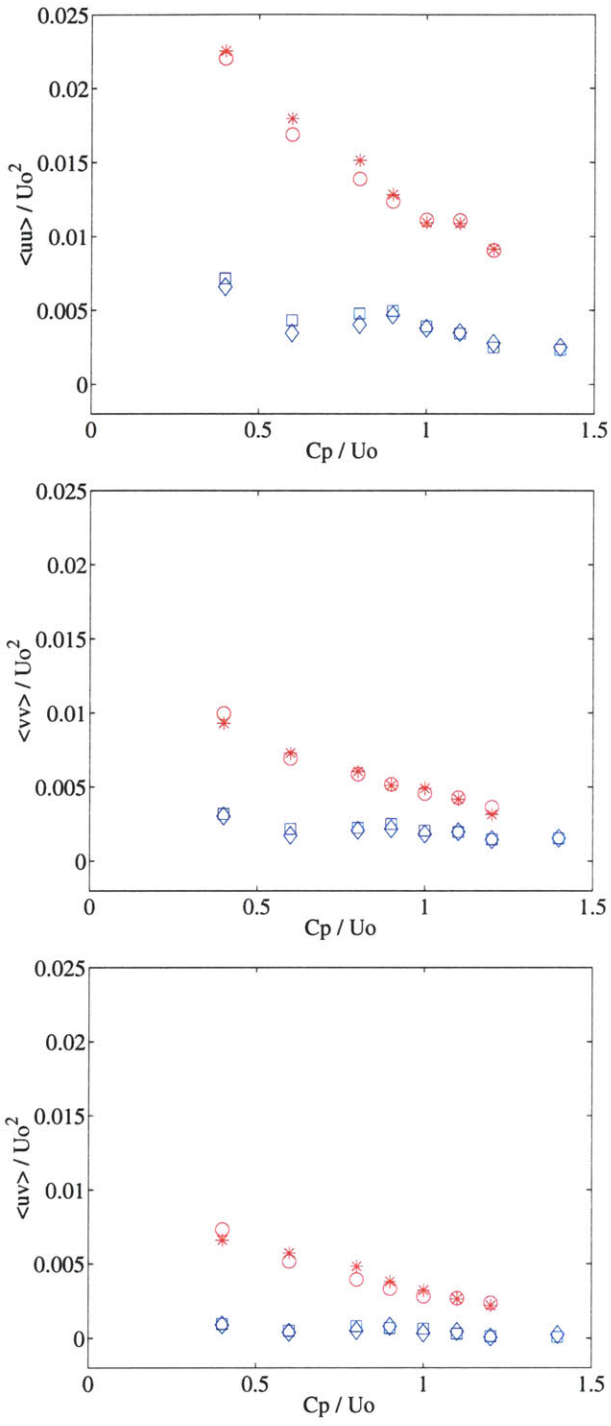

Figure 6-7: LDV bin averaged results acquired under piston #5 at the maximum and minimum excursion points. Turbulence statistics $\overline{u'^2}$, $\overline{v'^2}$, and $\overline{u'v'}$ are shown in the plots from top to bottom. Red is data at $\theta = 0°$ and blue is at $\theta = 180°$. The two symbols represent two independent runs for the same case.

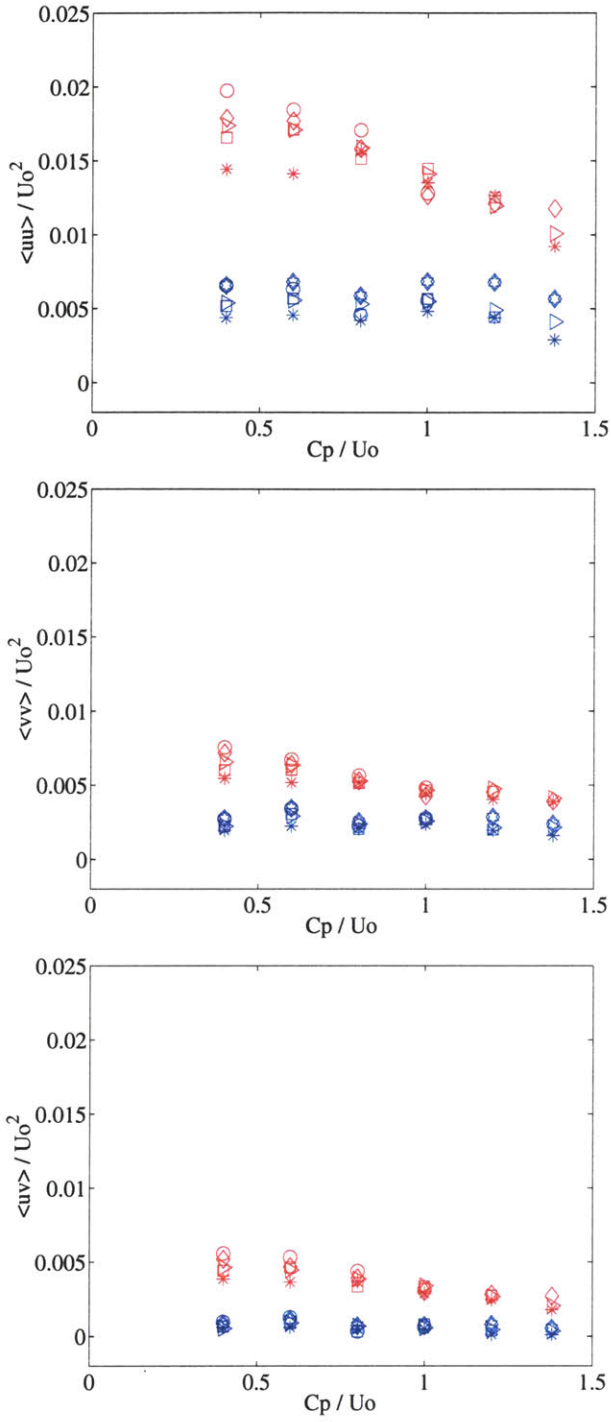

Figure 6-8: LDV bin averaged results acquired under piston #5 at several heights from the maximum and minimum excursion points. Turbulence statistics $\overline{u'^2}$, $\overline{v'^2}$, and $\overline{u'v'}$ are shown in the plots from top to bottom.Red is data at $\theta = 0°$ and blue is at $\theta = 180°$. Each symbols represents a different distance from the mat.

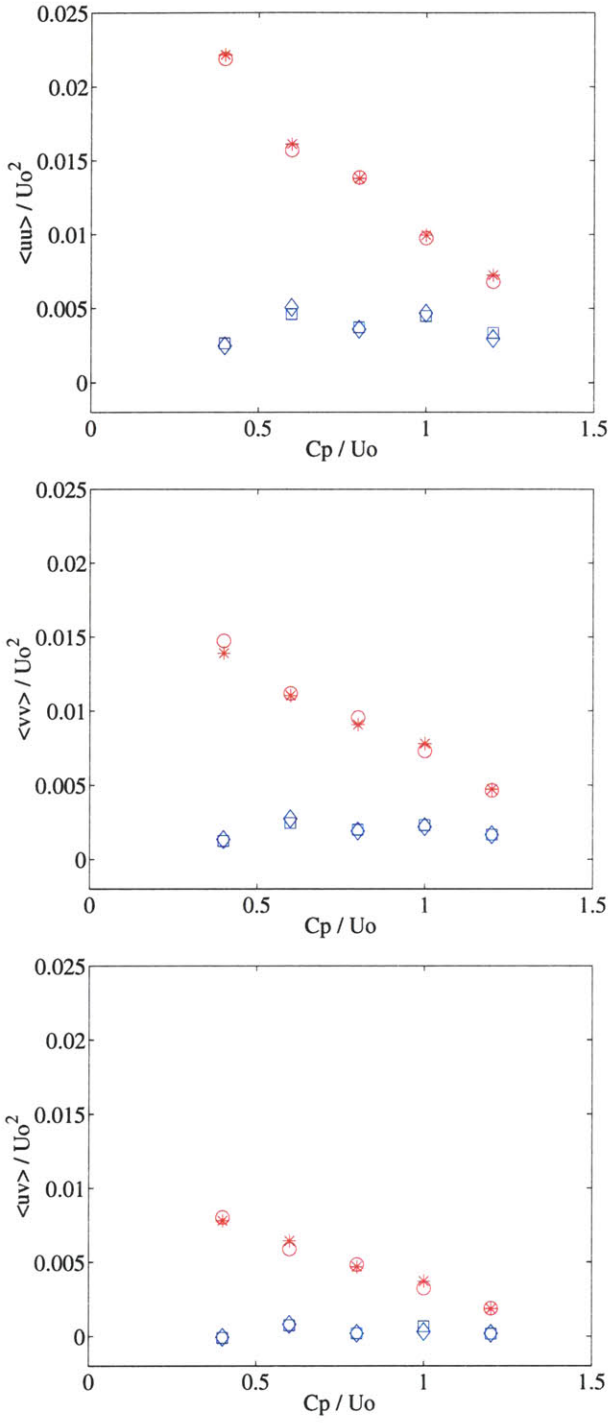

Figure 6-9: LDV bin averaged results acquired between piston #6 and #7 at the maximum and minimum excursion points. Turbulence statistics $\overline{u'^2}$, $\overline{v'^2}$, and $\overline{u'v'}$ are shown in the plots from left to right. Red is data at the trough and blue is at the crest. The two symbols represent two independent runs for the same case.

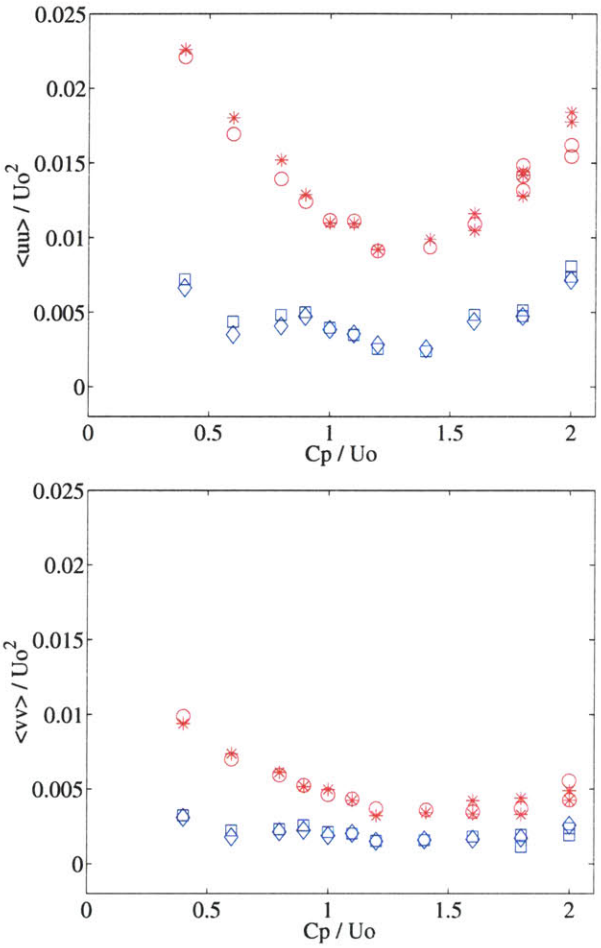

Figure 6-10: LDV bin averaged results acquired under piston #5 at the maximum and minimum excursion points. Turbulence statistics $\overline{u'^2}$, $\overline{v'^2}$are shown in the plots from top to bottom. Red is data at the trough and blue is at the crest. This represents the data shown in figure 6-7 and data taken at a later date for higher wave speeds. An increase in $< u'u' >$ is evident past $C_p/U_o = 1.4$.

Chapter 7

Particle Image Velocimetry of the Near Boundary Flow about the Waving Plate

In conjunction with the LDV tests particle image velocimetry (PIV) was performed on the waving plate for wave speeds $\zeta = C_p/U_o = 0.3,\ 0.6,\ 1.0,\ 1.2$. This chapter discusses the PIV experiments performed with the waving plate: the setup, processing and results are all included. Mean velocity profiles show acceleration of the flow beyond the inflow speed increasing with wave speed. Laminarization of the velocity profiles is indicated in agreement with numerical results and PTV from the *RoboTuna*.

7.1 Experimental Considerations for PIV Study

The MIT propeller tunnel has a rich history of flow measurement and visualization. The experiments on the waving plate presented here were the first digital particle image velocimetry experiments performed in this facility. Since the beginning of this thesis the PIV system has been widely and successfully used in several different experiments in the tunnel. The possibilities for future investigations are endless.

7.1.1 PIV setup for the Waving Plate Experiment

The PIV system was developed in a collective effort with Dr. Dana Dabiri, of CalTech. The image acquisition system was developed by General Pixels and then integrated with our existing laser and processing software. Several difficulties arose with the system integration, all associated with the timing system. These difficulties were circumvented by using an off-the-shelf timing box from Berkeley Nucleonics. A general picture of the total system setup is shown in figure 7-1.

The square test section made setup of the optical portion of the system straightforward. A New Wave ND:Yag laser, frequency doubled to 532 nm, was used to created the light sheet for the PIV tests. The Gemini PIV-120 is a compact, dual-cavity pulsed laser that delivers the light in 9 ns bursts of 120 mJ at a rate of 15 Hz from each head. The two laser heads are powered by separate power supplies and are controlled individually. A motorized light attenuator is capable of reducing the intensity of the output beam.

In order to capture the vertical velocity plane, parallel to the front window, the

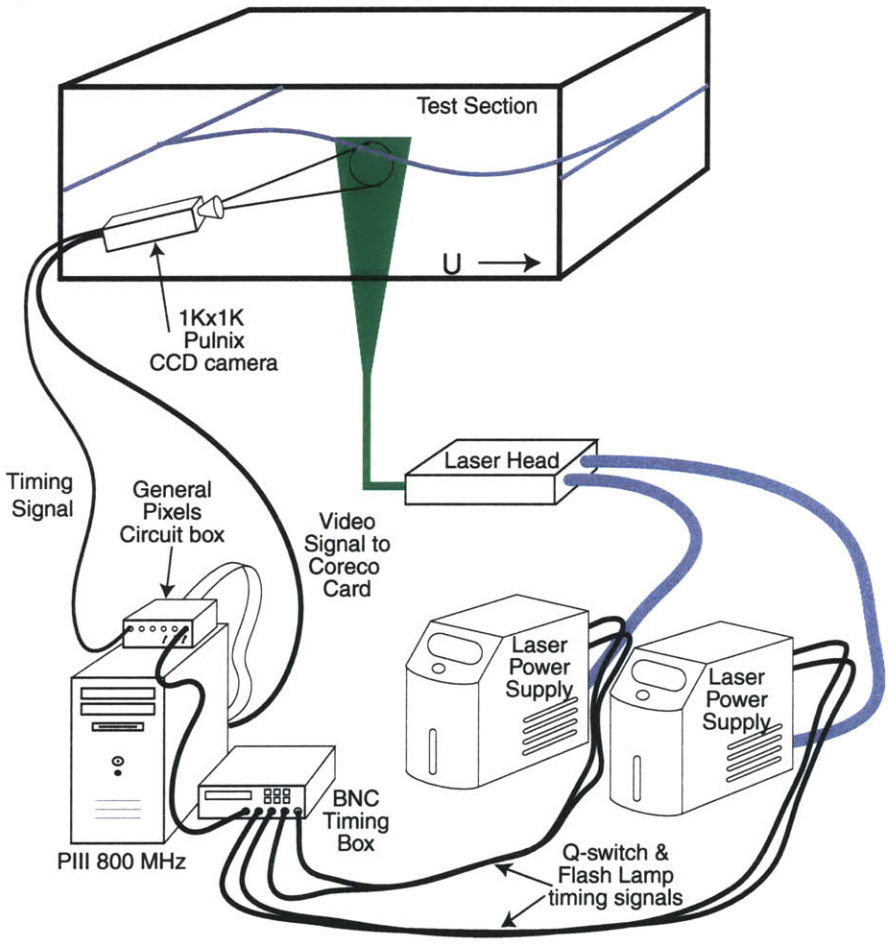

Figure 7-1: PIV setup at the MIT Propeller Tunnel for the waving plate experiment. The laser sheet enters from the test section bottom window, and the camera, mounted on the X, Y, Z-traverse, images the flow from the side.

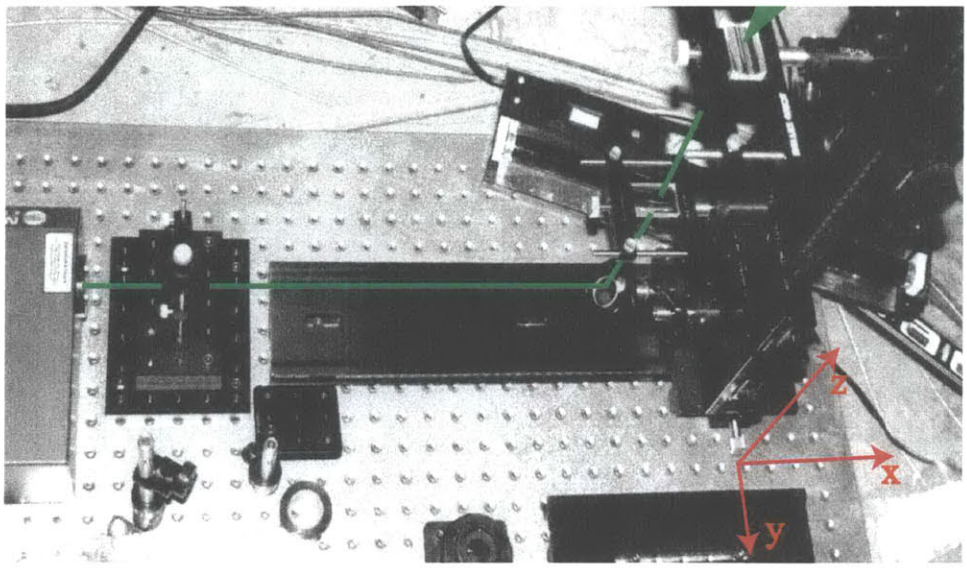

Figure 7-2: The optics for PIV are mounted on a breadboard below the tunnel test section. The New Wave laser head steers the beam through a series of optics. The green line represents the 532 nm beam which is formed into the PIV light sheet. The vertical optics are mounted on a rail which allows positioning at any point along the test section.

laser head was located below the test section. It was situated on a breadboard in line with optics arranged to steer the beam up into the tunnel and to create the light sheet. Figure 7-2 shows the beam path and optics arrangement.

First the beams exit the head of the New Wave Gemini:PIV laser and travel through a convex lens to collimate the beam. Next the beam reflects off the 45° first surface mirror that steers the horizontal beam vertically. The beam now passes through a convex lens that focuses it to a thin line and then through another convex optic, positioned 90° to the second optic, which spreads the thin line to a thin sheet. The light sheet is aligned in the direction of the flow and illuminates the mid-plane of the waving mat.

With the increased free stream flow speed and reduced field of view used to visualize the near-boundary flow, accurate timing of the laser pulses was important.

The image acquisition system from General Pixels included a National Instruments timing card that was controlled by the image processing software and an external timing circuit. Due to technical difficulties, however, this system had to be altered to generate the appropriate signal for the lasers. Thus an external timing box from Berkeley Nucleonics, Co. (BNC) was used in addition to the General Pixels timing box. Ultimately the composite video signal from the Pulnix camera was input to the General Pixels timing circuit which in turn passed a shifted frame marker to the BNC timing box. The BNC box was adjusted such that it output the requisite signals to the laser Q-switches and flash lamps.

The illuminated flow field was imaged by a Pulnix TM-1040 1K x 1K CCD digital camera mounted on a x, y, z traverse (seen at the right in figure 7-3) which allowed for accurate positioning, and re-positioning, of the field of view. The traverse accuracy is $+/-0.1mm$. Video is stored in 356 Mb of computer memory and transferred to hard drive. Image sequences were analyzed by PIV software developed by Dr. Sean McKenna of Woods Hole Oceanographic Institution [37].

PIV at a resolution of $1K$ x $1K$ presented an interesting data storage and processing problem. There was close to 100 GB of data acquired, something that would have been very expensive only a few years ago and was still daunting today. Processing the images was also a time consuming task. Ultimately, it would have been to our advantage to be able to synch the data acquisition with the mat motion, but we save this development for another thesis.

The rear window on the test section is fitted with a 3/8" shaft that has a ruler, attached to the end inside the tank, used to calibrate the PIV images. The ruler

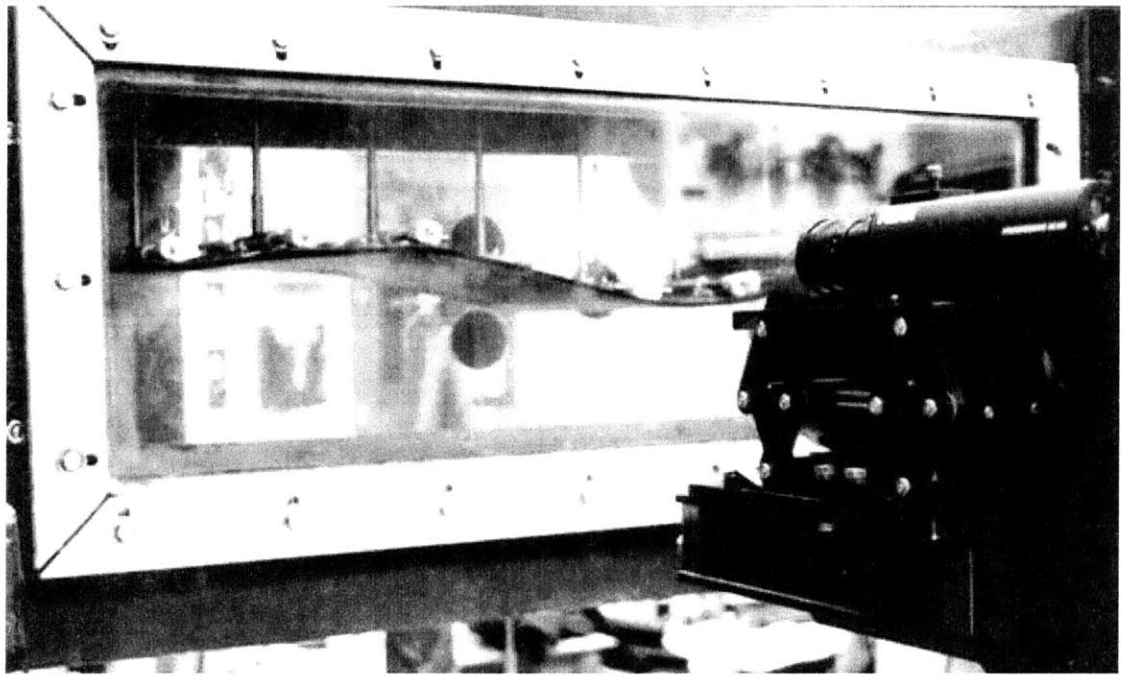

Figure 7-3: Close-up view of the waving mat through the tunnel window. At right is the X,Y,Z traverse and the CCD camera used in PIV. Adjacent to the camera is the LDV system.

remains inside of the test section, flush to the walls during testing. When a calibration image is taken, the ruler is moved into the plane of the laser sheet and digitized in both a horizontal and vertical direction. Calibration was performed each time the camera was moved or refocused. Ultimately no calibration was needed so long as the focus was not touched, nor the camera moved in or out of the laser sheet. Sideways and vertical movement of the traverse did not change focus.

7.1.2 Data Processing

Once the images were stored to the computer hard drive, they were analyzed for processing. The initial runs were 8 *cm* square and the final set were 2 *cm* square. It was found that the larger FOV (field of view) was insufficient in resolving the

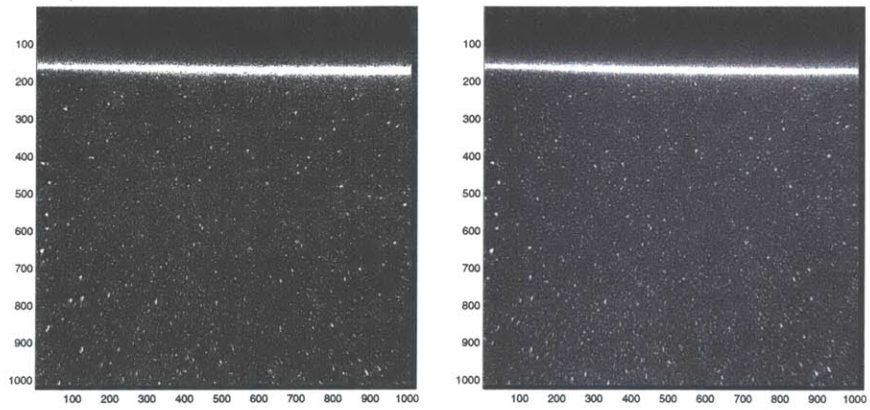

Figure 7-4: Typical image pairs the white line at the top of the image represents the body boundary. The axis are dimensioned in pixels. 1024 *pixels* represents approximately 2 *cm*.

boundary layer or any turbulence statistics, thus the second round of tests were performed. The processed images were phase averaged in similar fashion to the LDV data. The areas of interest were the extreme points of the mat motion.

The McKenna PIV code was used to process the data with a hybrid FFT (fast Fourier transform)/cross-correlation method. The first run data was obtained by the traditional FFT routine and then reiterated using the cross-correlation method. This yields high accuracy in the data and is discussed in detail in [37, 38].

The images were filtered to remove the presence of the boundary reflection before processing. Typical images are seen in figure 7-4. After processing, all data on the back side of the mat was annihilated. The mat was located both manually and by a median filtering of the image. Both processes were similar in effect and ultimately a combination of each was employed to avoid blind errors and double boundaries that occasionally arose with the automatic filtering.

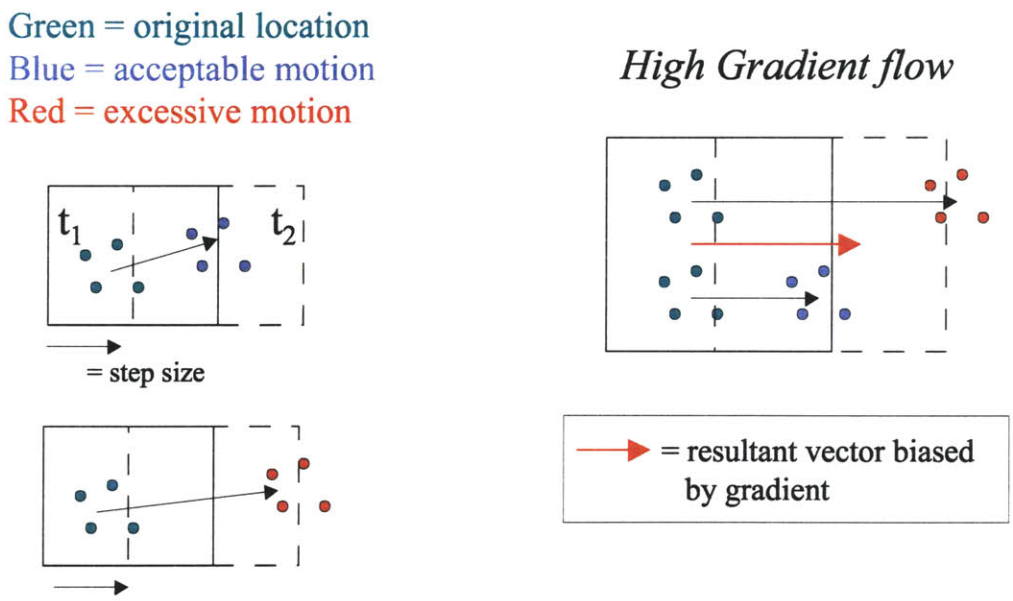

Figure 7-5: PIV considerations in high gradient flows. The solid line box indicates the original interrogation region, and the dashed box the stepped interrogation box. The green particles represent the original location, the blue an acceptable motion and red excessive particle motion that cannot be captured with the given box and step sizes. On the right we see how an interrogation box including particles that both move acceptable and excessive distances can result in a vector which is essentially an average value of the particles' motion.

7.1.3 High Gradient Flow Considerations

For flows with high gradients PIV processing techniques can run into trouble if the interrogation region is too large. In the case of near boundary flow with boundary layer thickness on the order of the interrogation box it can be near impossible to obtain accurate velocity measurements therein.

Figure 7-5 shows, in general, what can occur when the gradient is too large or interrogation window too small. If the interrogation region includes a high gradient the resulting vector is an average of the highest and lowest speeds. If the low speed is near zero and the upper velocity near free stream, as in an interrogation box that

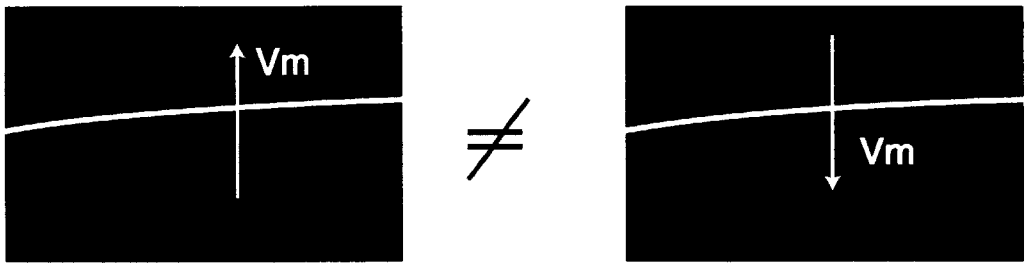

Figure 7-6: Requirement for phase averaging is both a coincident boundary location and identical sign mat velocity. The example illustrated in this figure would not be acceptable since the mat is moving in opposite directions despite the identical shape.

spans a boundary layer, the resulting vector is biased to the free stream.

One possible way to improve upon this is to reduce the size of the interrogation region, however we are limited in size for several reasons, including particle seeding and actual particle motion in pixels. Another option is to magnify the field of camera view which can also require smaller particles for seeding. In this set of experiments we opted to reduce our FOV from 8 *cm* to 2 *cm* square and use smaller particles than typically employed in our tests. These particles were not fluorescent but were smaller diameter silver coated glass spheres which are highly reflective.

7.1.4 PIV phase averaging

In choosing the images to phase average, care was taken not to choose images pairs in which the boundary matched solely in location but also in direction of motion. For example, it would not be appropriate to average a data set in which the mat had just passed an extreme with a data set in which the mat had not yet reached that extreme. In these cases the predominate mat velocity would be opposite in sign (figure 7-6).

Results from the PIV experiments on the waving plate will be presented in the

next section. The focus will be on the phase matched average data and the statistics that arise from this averaging. As discussed above the phase matching was a tedious process but was successful in obtaining average velocity data for the mat crest and trough cases. The body boundary for the average mat location, within one pair, is determined and the velocity vectors are decomposed into the normal and tangential velocity components. Once the tangential and normal components were determined it was straight forward to obtain the velocity profiles.

For each run, particle velocity fields obtained from PIV image pairs were phase averaged to obtain flow averages and turbulent statistics. For each velocity field the average field was subtracted leaving the fluctuations in u and v-velocity, or u' and v'. Using the fluctuations of the instantaneous velocities, the turbulence intensities, $\overline{u'^2}$, $\overline{v'^2}$, $\overline{u'v'}$, were determined again by averaging at a constant phase, ψ. The resulting data available, in addition to the instantaneous whole field velocity data U and V, were the phase average velocities $\overline{u}$ and $\overline{v}$, the instantaneous fluctuations in flow from each individual data set u' and v', and the phase averaged turbulence statistics. All velocity data is normalized by the inflow velocity, U_o, unless otherwise specified.

7.2 Phase averaged velocity profiles

Phase average velocity files are determined from the PIV data sets as discussed in the previous section. In addition to the phase averaging, a local average was taken over five degrees, $\theta = \frac{180}{\pi}kx$, where x is the length down the mat, centered at $\theta = 251°$.

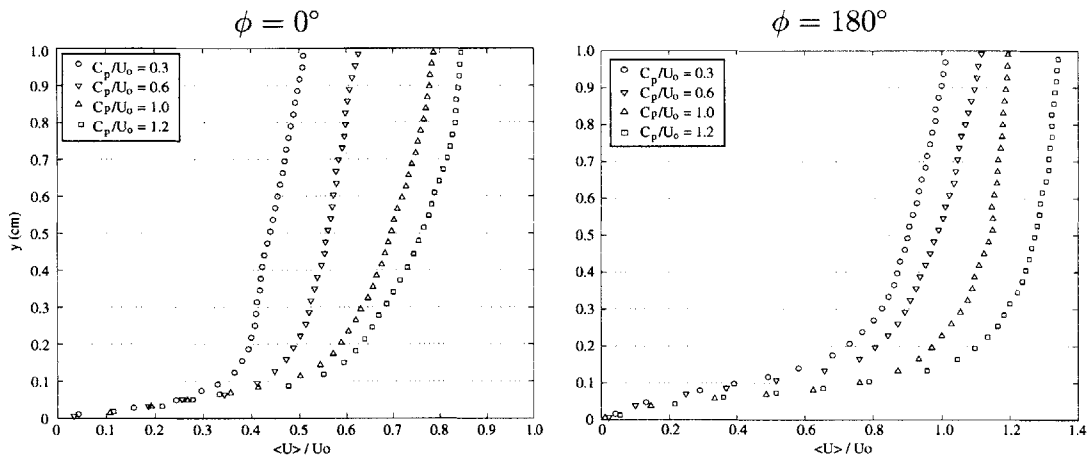

Figure 7-7: Phase averaged velocity profiles for $U_o = 0.5\ m/s$ ($R_\lambda = 500,000$). Four phase speed cases $\zeta = 0.3$, 0.6, 1.0, and 1.2 are shown for the two mat positions TDC, $\phi = 0°$, (left) and BDC, $\phi = 180°$, (right).

Care was taken to assure that this region did not present significant local curvature or slope in the body boundary.

Figures 7-7 and 7-8 show the average velocity profiles for the two Reynolds number cases, $5x10^5$ and 10^6. The four phase speed ratios,

$$\zeta = C_p/U_o = 0.3,\ 0.6,\ 1.0,\ \text{and}\ 1.2,$$

are represented by the four different symbols labelled in the plot legends. The average velocity profiles from the zero and 180 degree phase cases are shown in each figure, on the left and right plots respectively. Again $\phi = 0°$ is a trough location with concave curvature and $\phi = 180°$ is a crest location with convex curvature in the same fashion as discussed in chapter 6.

At both Reynolds numbers, the phase averaged u-velocity profiles were significantly different for the two extreme phases, $\phi = 0°$ and 180°. For both flow speeds

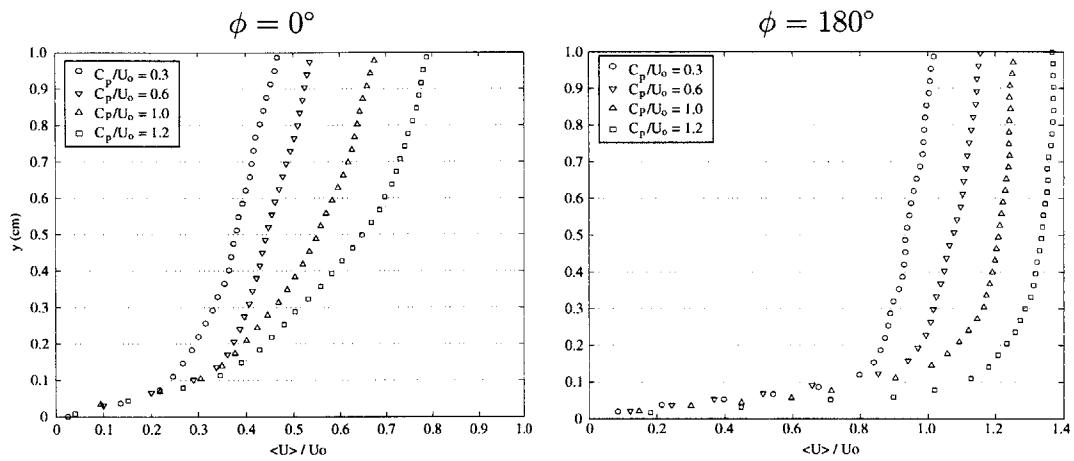

Figure 7-8: Phase averaged velocity profiles for $U_o = 1.0\ m/s$ ($R_\lambda = 1,000,000$). Four phase speed cases $\zeta = 0.3$, 0.6, 1.0, and 1.2 are shown for the two mat positions TDC, $\phi = 0°$, (left) and BDC, $\phi = 180°$, (right).

in increase in phase speed corresponds to an increase in velocity away from the wall with respect the next lower phase speed case.

In the trough region, the flow is significantly decelerated from the inflow velocity, U_o, which is consistent with the idea of mass conservation. It is also evidenced in the average vertical velocity profiles shown in figure 7-9 for inflow speed 0.5 m/s ($Re = 5 \times 10^5$). Since the mat is moving vertically and the "no-slip" condition must be applied there must be a non-zero velocity at the mat boundary except at points where the mat is precisely at the top or bottom of its trajectory where the mat velocity is zero. Depending on the phase instance that the averages were taken at the mat did have a vertical velocity. Every attempt was made to obtain the exact crest and trough, however the mat motion was not directly synched with the camera's frame rate.

In the velocity profiles corresponding to $\phi = 0°$, the average v-velocity is negative throughout which is this case is indicative of fluid moving away from the boundary or

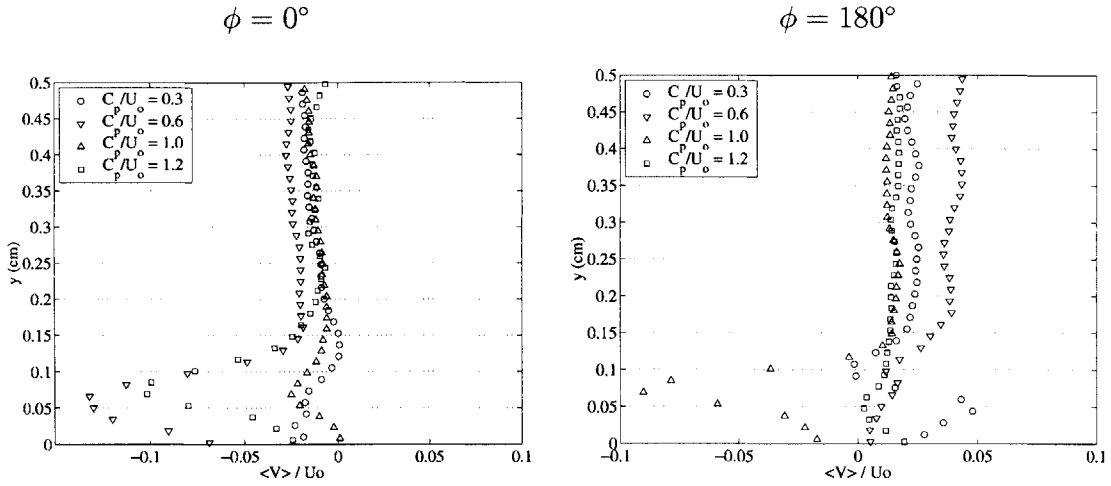

Figure 7-9: Mean Vertical Velocity profiles for $U_o = 0.5\ m/s$. Symbols correspond to those in figure 7-7.

momentum "leaking" from the boundary layer which would cause deceleration. This is the opposite at the crest where the fluid was moving up towards the mat. It would be good to note here that in the actual experiments that the measured flow was on the underside of the boundary and that negative v-velocity indicated flow in a normal direction away from the mat. In all profiles the values of y were taken positive away from the mat for clarity.

Looking back to the average u-velocity profiles for all four phase speeds, and both inflow velocities, the tangential fluid velocity approaches or exceeds the inflow velocity. In the slowest wave speed case, the flow reaches the value $U/U_o = 1.0$. The outer flow regions show accelerated flow beyond free stream increasing with phase speed. This acceleration requires some influx of fluid which is also confirmed by the vertical velocity component.

The average velocity profiles reveal slight differences between the two Reynolds number cases. At the crest phase, $\phi = 180°$, the averaged velocity profiles show a

steeper velocity gradient near the wall than in the trough cases. This gradient is higher at the Reynolds number 10^6 than at $5x10^5$. This gradient is indicative of high wall shear stress and tends to increase with increased wave speed. Also at the higher Reynolds number runs the profiles at $\phi = 180°$ the boundary layer thickness is reduced from the lower speed cases at this phase.

One significant difference between the two Reynolds number cases is the shape of the profiles for the $\phi = 0°$. At the higher inflow speed, the outer flow measured within the PIV field of view does not reach freestream values and appears to have a lower wall friction, or velocity gradient, than the lower Reynolds number case.

7.3 Averaged Velocity Profiles in a Moving Reference Frame

The relative velocity of the fluid compared to the traveling wave speed can be explored in a reference frame moving with the mat crest (or trough) at the wave speed, C_p. First the following transformation is performed on the phase averaged velocity fields to observe the flow fields in the moving frame:

$$\frac{U_r}{U_o} = \frac{U - C_p}{U_o} \tag{7.1}$$

The plots in figure 7-10 show the various cases in the moving reference frame. The data is taken at the same spanwise phase, $\theta = kx$, as in the averages plotted in figures 7-7 and 7-8 and again is averaged over 5 degrees. If the flow was moving a

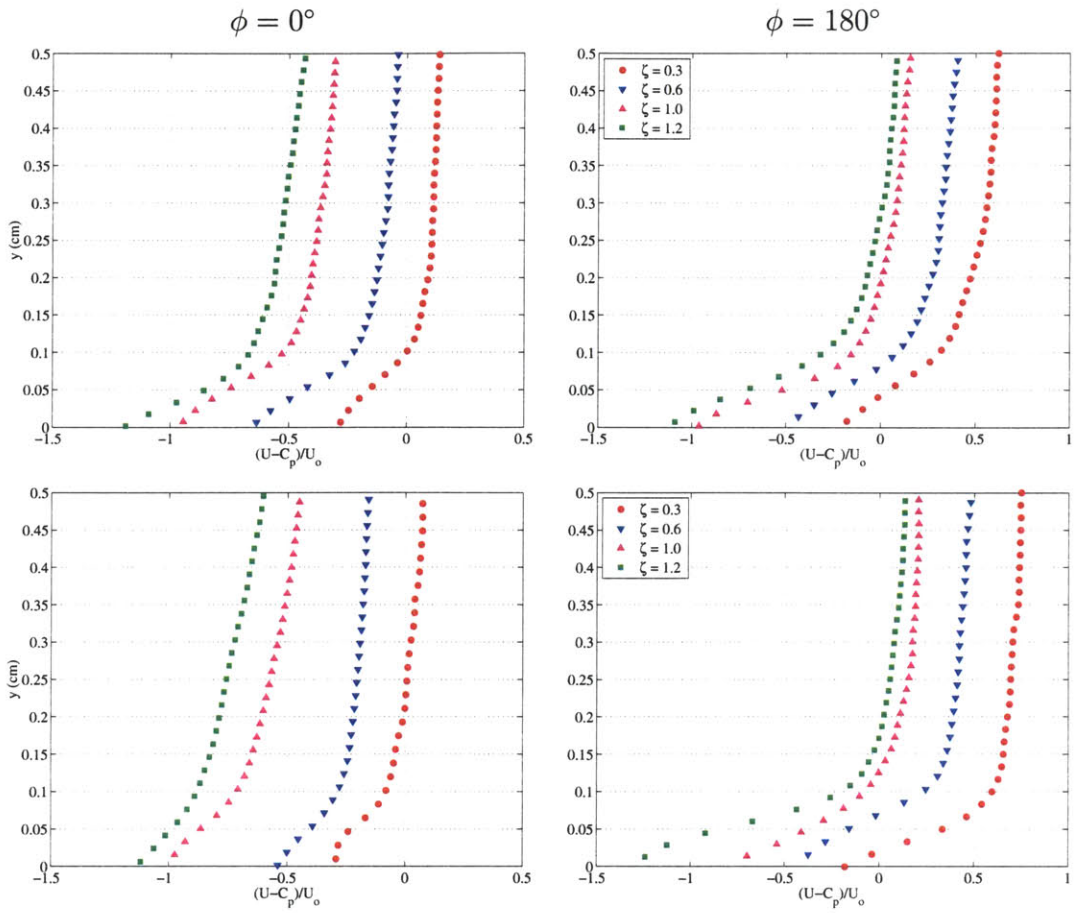

Figure 7-10: Relative velocity fields at Reynolds number 5x10^5 (top) and 10^6 (bottom), in the reference frame moving at phase speed C_p. Phase $\phi = 0°$ is the trough location and $\phi = 180°$ is the crest. Negative data indicated flow moving slower than the phase speed and positive data faster than the phase speed.

speed faster than the phase speed, these plots would show positive forward velocities. When the flow is slower than the phase speed negative velocities arise. The data where the flow speed nearly matches the phase speed the velocities are very small. Non-dimensionalization of the data by the inflow speed allows us to compare the two Reynolds number cases.

For the cases at $\phi = 180$, with convex curvature, that for both speeds, the outer flow at the appears to be accelerated further beyond the *phase* speed for all traveling

wave speeds in the outer regions and slower than phase speed nearest to the wall.

The trough cases are a different story however. The only case seeing acceleration beyond the phase speed is the lowest phase speed case. The other three cases indicate flow slower than the phase speed. The magnitude of this relative decrease in outer flow increases with $\zeta = C_p/U_o$. Recall, in all trough cases the flow speed is less than the inflow speed as shown in figures 7-7 and 7-8.

Looking back at figure 2-7 for convex curvature, if the fluid flow at some distance away from a sliding boundary is moving slower than the mat then it is unstable and if the flow is moving faster it is stable. The relative velocity between the flow and the mat is defined as $U_r = U - C_p$ where U is the average flow velocity and C_p is the mat speed. In figure 7-10 the relative velocity is non-dimensionalized by the inflow speed which does not effect the sign of the arrows in these plots. If the velocity is negative then the tangential velocity, U, is less than the mat speed and if positive the flow is greater than the phase speed.

Following figure 2-7, the Taylor-Görtler stability criteria for concave and convex curvature, though not conclusive for unsteady flows, is tabulated below, where $U_r = U - C_p$ is the relative velocity plotted in here in figure 7-10.

	CONCAVE	CONVEX
	$\phi = 0°$	$\phi = 180°$
STABLE	$V_r < 0$	$V_r > 0$
UNSTABLE	$V_r > 0$	$V_r < 0$

Referencing this table we can look at the vector fields to assess the stability of the

different speeds and mat phases.

Figure 7-10 shows, at the trough, as wave speed increases the relative velocity is increasingly negative, or stabilizing, whereas at the crest this trend is not observed. The flow in the outer region, however, is accelerated beyond C_p for all wave speeds. The time scale at which alternating curvature arises is shortened with increased phase speed limiting the time the flow has to recover from the previous geometry. As seen in steady convex curvature, the flow is slow to recover to its initial, pre-curvature, state after the curvature is removed. As a result of the increasingly rapid changing curvature, flow has less time to recover as traveling wave speed increases and the stabilizing effects, turbulent reducing effects, of the traveling wave will persist in crests and troughs.

7.4 Logarithmic velocity profiles

In order to better understand the effects of the traveling wave motion, the data is compared to the log-law profile for a turbulent boundary layer. Again it is important to note that this profile is valid for a flat plate and is changed with curvature and added pressure gradients. This problem introduced additional pressure gradient terms and boundary conditions not accounted for in the flat plate boundary layer log-law.

When the horizontal velocity data, normalized by the free stream, is plotted in a semilog plot versus the y coordinate, as it is in figure 7-11, for $U_o = 1.0\ m/s$, we immediately see a distinct difference between the crest and trough cases. For the crest the profiles resemble the shape of the plots we are familiar with for turbulent

boundary layers with a relatively linear region near the wall and a logarithmic layer some distance from the wall. As phase speed increases this log region extends to higher velocity which is consistent with what is shown in the average profiles (figures 7-7 and 7-8) in the cases at $\phi = 180°$ where the flow is accelerated beyond the inflow speed, compared with the cases at $\phi = 0°$ where the flow still has not reached $u/U_o = 1.0$ at several centimeters from the mat.

Next the near wall data is analyzed to obtain the values for the velocity slope $\partial U(y)/\partial y$ in order to calculate the frictional velocity defined as

$$u^* = \sqrt{\frac{\tau_w}{\rho}} = \nu \left. \frac{\partial U(y)}{\partial y} \right|_{y \to 0} \tag{7.2}$$

where τ_w is the shear stress at the wall. The frictional velocity can then be used to transform the data into wall coordinates, u^+ and y^+, found as

$$u^+ \equiv \frac{\overline{u}}{u_*} \; and \; y^+ \equiv \frac{u_* y}{\nu}, \tag{7.3}$$

where u_* is the frictional velocity and ν is the kinematic viscosity. The log-law for the flat plate is plotted as

$$u^+ = y^+ \tag{7.4}$$

through $y^+ = 10$ and

$$u^+ = \frac{1}{\kappa} ln y^+ + C \tag{7.5}$$

beyond $y^+ = 10$, with constants $\kappa = 0.41$ and $C = 5.5$.

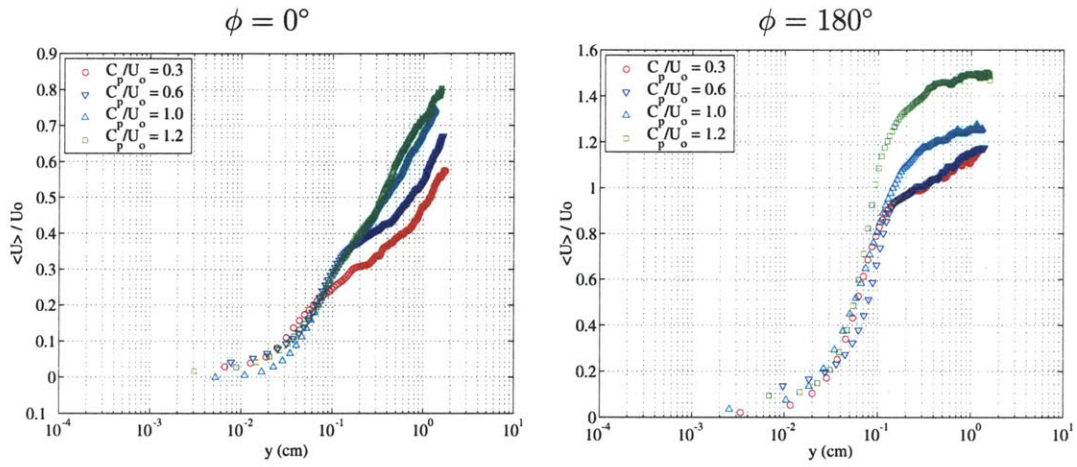

Figure 7-11: Mean Velocity profiles for $U_o = 1.0\ m/s$ plotted in semilogx scaling U by outer variable, U_o.

Figure 7-12 shows the profiles plotted in wall coordinates again for $U_o = 1.0m/s$. The solid black line in these plots represents the theoretical curves for a turbulent boundary layer given by equations 7.4 and 7.5. At $\phi = 180°$ we see an extension of the laminar region as the phase speed increases beyond the inflow speed. The logarithmic layers persist however. This laminarization can be explained in part by the change in pressure gradient with traveling wave speed. In contrast, for the region of concave curvature, $\phi = 0°$, the logarithmic region is no longer apparent at $\zeta = 1.2$—it is only for $\zeta = 0.6$ and lower, that we see a region resembling the log region of flat plate boundary layer profiles. These changed can be contributed in part to the pressure gradient effects and are indicative of boundary layer laminarization.

7.5 PIV Turbulence Statistics

Turbulence statistics obtained through phase averaging of PIV data sets were calculated and plotted versus distance from the mat. Only data with more than 50

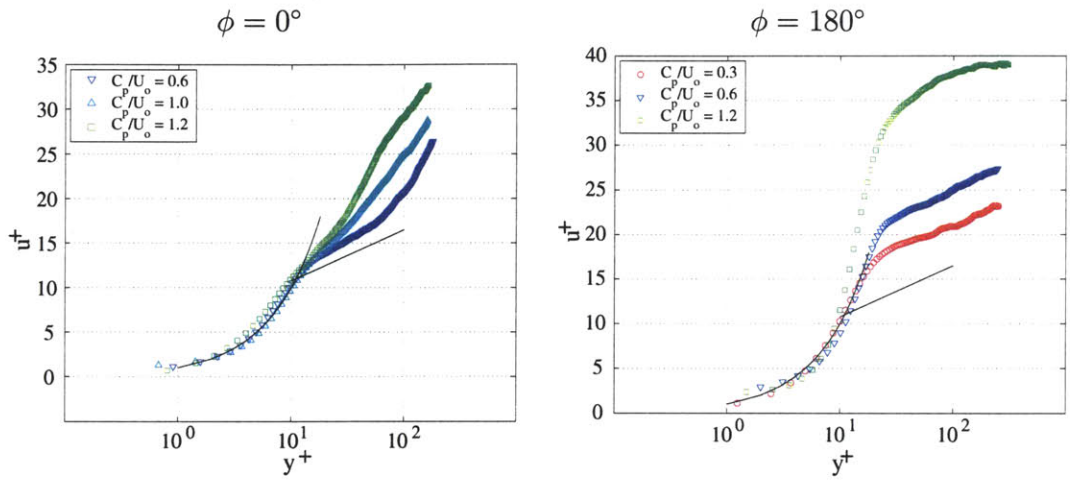

Figure 7-12: Mean Velocity profiles for $U_o = 1.0\ m/s$ plotted in semilogx scaling U by inner variable, u^*. Solid line represents the theoretical curves for the log-law from equations 2.14 and 2.18.

samples are shown herein. Data for Reynolds number 1,000,000 includes greater than 75 samples. It is important to note that outside of the boundary layer the accuracy of the turbulence fluctuations, as calculated from the PIV data, decreases due to interrogation box size, timing and the flow speed. In order to keep consistent the same basic processing method was used for all cases.

An advantage of PIV in this problem is the ability to obtain data very near to the boundary. The LDV system is limited by the incident angle of the vertical laser beams and the distance into the tunnel. PIV could be obtained at any spanwise location into the tunnel. The PIV field of view was 2 *cm* square and the seeding sufficient to allowing significant data within 2 *mm* of the boundary. Outside of this distance the accuracy of the PIV is reduced compared to the LDV since the pixel displacement is greatly increased with respect to the near-wall velocities and the box size remains fixed. The number of PIV images acquired for phase averaging resulted in accurate averages, in other word more data sets did not change the average data,

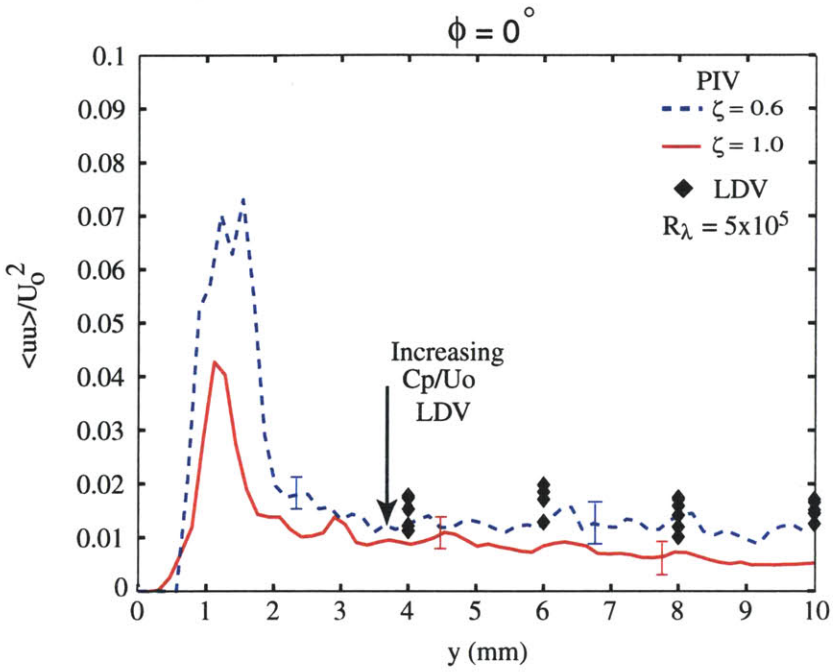

Figure 7-13: Phase averaged statistical profiles from PIV at TDC ($\phi = 0°$) under piston #5. Data is normalized by inflow velocity. LDV data, plotted in figure 6-8 is superimposed at the respective heights for multiple phase speeds up to $C_p/U_o = 1.2$. LDV data at each height decreases with increasing phase speed.

but there were changes in the statistical data yielding an error around 10%. In several cases this makes the relative values of the intensities difficult to evaluate. However the regions near the wall where the intensities peak the data is more accurate.

Again the different phase speed cases are shown on the same plot for one Reynolds number and phase location. Figure 7-13 shows data from $R_\lambda = 5\text{x}16^5$ and figure 7-14 for $R_\lambda = 10^6$. Near the mat there is an increase in streamwise turbulence levels noted in the profiles show in figures 7-13 and 7-14. The streamwise turbulence intensity was less for the increased phase speed cases especially near the wall. This is in keeping with the LDV results presented in chapter 6.

Figure 7-13 shows the PIV statistics from flow in the trough, $\phi = 0°$, at the lower

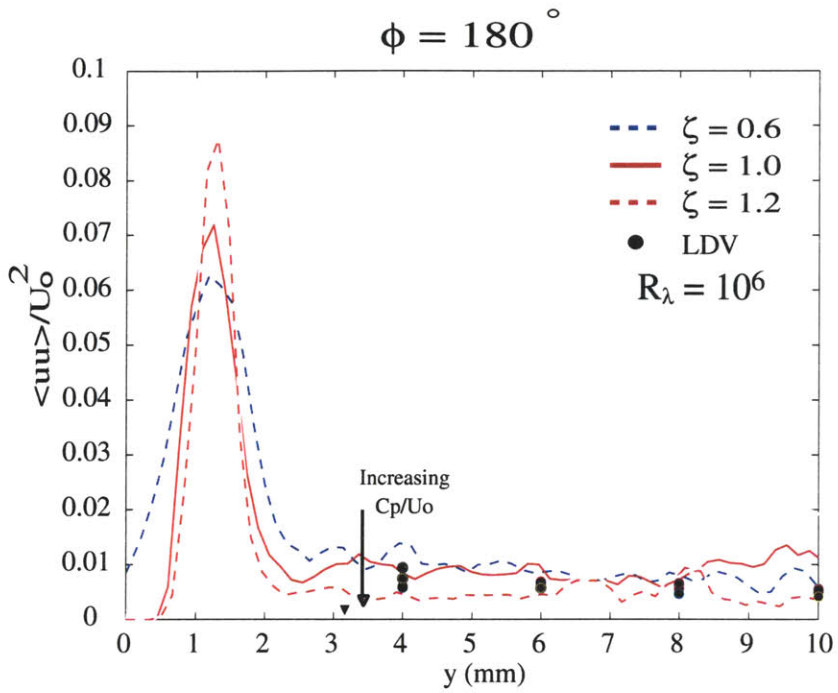

Figure 7-14: Phase averaged statistical profiles from PIV under piston #5 at BDC ($\phi = 180°$). Data is normalized by inflow velocity. LDV data, plotted in figure 6-8 is superimposed at the respective heights for multiple phase speeds up to $C_p/U_o = 1.2$. LDV data at each height decreases with increasing phase speed.

inflow speed with results from the LDV data superimposed. The LDV data is plotted with the same symbol for different phase speed are not changed as this is merely used to show general comparisons. As wave speed increases up to $C_p/U_o = 1.2$, LDV shows decreased streamwise intensities – the diamone symbols shown at each height are, from higher to lower intensity, increasing in C_p/U_o. Only two phase speeds are shown for the PIV data since the alternate phase speed cases contained less than 50 samples. For the higher wave speed $\zeta = 1.0$ the intensity level is decreased over the height of the profile with respect to the lower wave speed case. For both phase speeds there exists a maximum near the boundary before the intensity collapses to a constant value.

In figure 7-14 data plotted at the crest, $\phi = 180°$, is for Reynolds number 1,000,000 with LDV again superimposed in the same fashion as the previous plot. At this speed, and phase location, there is a closer agreement between LDV and PIV data. This is contributed in part to two factors, PIV sample size being larger than 75 and increased data rate for LDV at the higher speed. As C_p/U_o increases the local turbulence reduces non-homogeneously again peaking near the boundary.

Figure 7-15 shows non-dimensional vertical intensity at Reynolds number 1,000,000 from PIV compared with direct numerical simulations at Reynolds number 6,000. Similar trends persist for both cases suggesting that the persisting mechanism for turbulence modification exist at higher Reynolds numbers.

7.6 Summary

The results from the PIV tests on the waving plate were presented for the fours phase speed cases. Agreement with numerical simulations and LDV results are encouraging. Logarithmic velocity profiles show laminarization of the flow with increasing phase speed at the crest locations. This data is again comparable with the PTV data from the RoboTuna in chapter 4 and numerical simulations by Zhang [65]. At the crest phase the log-profile region is highly modified and not apparent in the highest phase speed case, $\zeta = 1.2$.

Average velocity profiles show heightened acceleration, beyond the freestream speed, and also the wave speed, for increased traveling wave speeds at the crest phase. In the trough region, the flow does not quite reach freestream within the

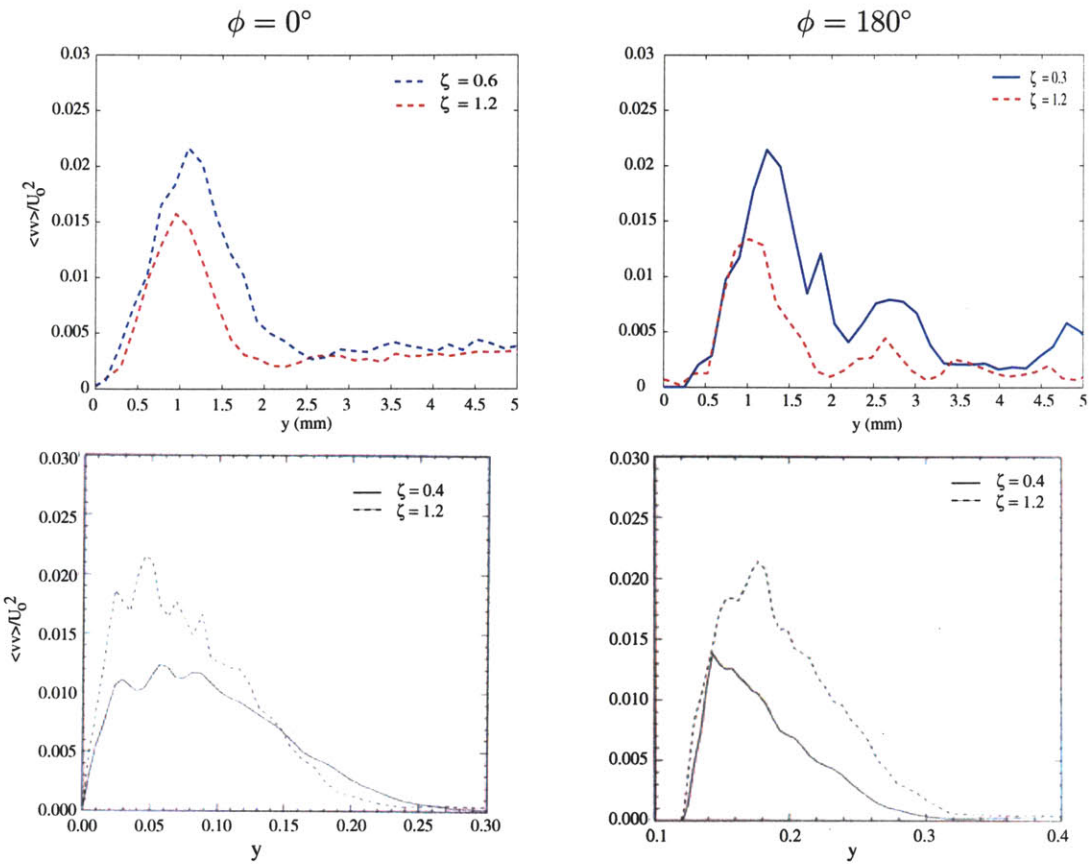

Figure 7-15: Phase averaged vertical energy profiles from PIV at $Re = 10^6$ (top) and CFD at $Re = 6000$ (bottom) at $\phi = 0°$ (left) and $\phi = 180°$ (right).

PIV field of view, however for the lowest phase speed case the flow beyond a certain height from the wall surpasses phase speed. In part the accelerations effects by the travelling wave at the crest are augmented by the phase dependent pressure gradient which coincides with the baseline velocity fields presented in figure 6-4. These effects also change the shape of the velocity profiles.

In general the average $< u'u' >$ profiles show an increase very near the wall before collapsing to a freestream value. These results show that the intensity is reduced for higher flow speeds and is maximum at different distances from the wall. The vertical intensity profiles compare well with numerical simulations by Zhang [65].

Chapter 8

Extensions for Further Study

This thesis has looked at the fundamental hydrodynamics of a traveling wave motion on the surrounding fluid flow. With the existing device, future work can extend the problem to higher Reynolds numbers to confirm benefits persist at engineering Reynolds numbers. Attempts to capture evolving structures, such as Λ-vortices, in the boundary layer can be achieved with modified experimental setups such as using a moving camera synched to the mat motion or looking directly at the mat surface using laser induced fluorescence.

The two techniques, LDV and PIV, are powerful flow measurement and visualization tools. However they are both limited in some way. While the PIV was tedious to obtain highly accurate turbulence statistics (with more that 100 samples), the LDV system was less time consuming and subjective. In this instance PIV both succeeded and struggled. The LDV setup as used in this thesis precluded obtaining data very close to the body boundary. Implementation of a fiber optic probe on LDV will add greater flexibility and allow measurement of velocities very near the wall (avoiding

beam clipping) and also in the third dimension.

In PIV testing particle sizing, seeding density, field of view, and light pulse separation are parameters that must be optimized for the specific task at hand. In the case of high gradient flows, specifically near wall, the task of choosing the appropriate setup and timing becomes difficult. One set of parameters might work well for the very near wall flow and another for outer flow, indicating that advanced processing, such as multi-grid methods, could be warranted.

Ultimately, it is the applications of such flow modification devices are of interest to commercial and military operations. How the waving plate might be used for drag reduction or wake modification is interesting. Steering away from drag reduction applications, deploying a waving surface aft of a traditional propulsor to modify the wake signature could be useful for masking underwater vehicles from being detected.

The waving plate studied here is only a two-dimensional swimming body, however aquatic creatures and underwater vehicles are three-dimensional in shape. The RoboTuna data suggests that the mechanisms seen on the flat traveling wave wall are present at least along the midline of the swimming 3D body. How this extends to more revolved bodies is an area for further exploration.

Fish are not the only aquatic creatures that use undulatory motion as their method of propulsion. Sea snake and eels both swim using a traveling wave body motion. Study of this motion on three dimensional models of such animals can yield further insight into the problem of aquatic locomotion. Since most sea snakes are poisonous by nature, it is essential to model the snakes behavior in order to better understand it. This can be done by replicating the geometry, to an extent, of a snake such as

Figure 8-1: Photograph of a preserved sea snake *Astrotia stokesii.* The bottom image shows the paddle shaped tail.

the preserved sea snake, *Astrotia stokesii*, photographed figure 8-1. Sea snakes have interesting geometry, with a cross sectional shape that includes a keel and also a paddle shaped tail. The presence of this paddle tail is arguably similar in use to the tail fin on a fish.

A model snake is molded from flexible polyurethane and attached to the same apparatus used to undulated the waving mat. A isometric view of the assembly can be seen in figure 8-2. This apparatus is equipped with a force sensor and hot-wire

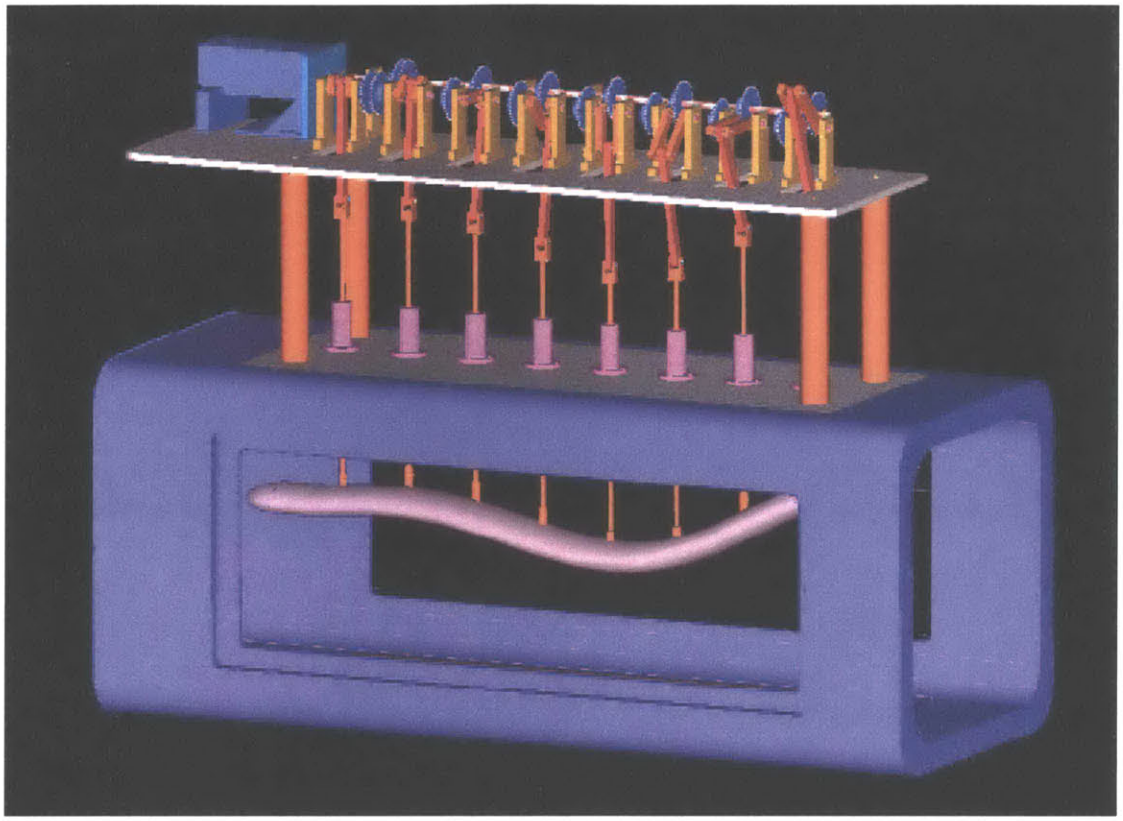

Figure 8-2: Isometric view of the molded, flexible polyurethane sea snake attached to the waving plate mechanism.

probes. These measurements in conjunction with LDV and PIV will hopefully lead to a clearer understanding of how snakes and eels harness the traveling wave motion to attain such graceful propulsion.

The evolution of modern technologies such as artificial muscles give way to opportunities to design novel propulsive and maneuvering devices that have no mechanical parts. Combined with a good understanding of unsteady hydrodynamics, these technologies excite novel applications to biomimetic underwater vehicles and propulsion mechanisms. The confirmation of turbulence reduction and flow laminarization illustrates the complexity of evolution in nature and the elegant simplicity that exists therein.

Chapter 9

Conclusions and Contributions

This thesis examined the near–boundary flow modification by fish-like swimming motion. Two different experimental devices were studied: the MIT *RoboTuna* and the two-dimensional waving plate mechanism. Data obtained in both cases revealed similar features and extended the current knowledge base to higher Reynolds numbers, up to 10^6 based on wavelength of the mat. Thesis contributions and conclusions are summarized below.

Data from the swimming *RoboTuna*showed indications of turbulence reduction at $R_L = 8x10^5$. The *RoboTuna* PTV data reveals that the traveling wave body motion at Cp/Uo = 1.14 tends to laminarize velocity profiles at several phases of swimming motion compared to the straight towed case at Reynolds number 800,000.

A robust mechanism was designed, constructed and tested in the propeller tunnel to study swimming motions at Reynolds numbers up to 1,000,000, with the potential for higher Reynolds number studies. Results with the waving plate apparatus show that the oscillating mat reduces and ultimately eliminates separation up to $R_\lambda = 10^6$

as C_p/U_o approaches unity and conclusively showed the non-homogeneous reduction of turbulence at $R_\lambda = 5x10^5$ and 10^6 for C_p/U_o up to 1.2. Intensities reach a minimum at $C_p/U_o = 1.2$ and above 1.4 start to rise again. Despite this turbulence reduction, frictional drag is increased for the higher phase speed on crest. Frictional drag is lower in trough region than at crest and increases with phase speed at $R_L = 5x10^5$.

This turbulence reduction is connected with an apparent laminarization of average velocity profiles shown in the PIV data from both the Waving plate and the *RoboTuna.* Phase average velocity profiles for the waving plate progressively laminarize as C/U increases to 1.2. In the RoboTuna, velocity profiles for c/U=0, non-swimming, has the characteristic shape of a turbulent profile; but for the swimming case it has largely laminarized. In agreement with the Robotuna data and numerical simulations, PIV and LDV results compare with complementary region of boundary layer showing consistent trends. These results compare well with numerical simulations at $R_l = 6000$ [65].

Bibliography

[1] R. J. Adrian. Multi-point optical measurements of simultaneous vectors in unsteady flow: A review. *International Journal of Heat Fluid Flow*, 7:127–145, 1986.

[2] R. J. Adrian. Particle-imaging techniques for experimental fluid mechanics. *Annual Review of Fluid Mechanics*, 23:262–304, 1991.

[3] R. J. Adrian. Dynamics ranges of velocity and spatial resolution of particle image velocimetry. *Meas. Sci. Technol.*, 8:1393–1398, 1997.

[4] B. Ahlborn, S. Chapman, R. Stafford, R. Blake, and D. Harper. Experimental simulation of the thrust phases of fast-start swimming of fish. *Journal of Experimental Biology*, 200:2301–2312, 1997.

[5] B. Ahlborn, D. Harper, R. Blake, D. Ahlborn, and M. Cam. Fish without footprints. *Journal of Theoretical Biology*, 148:521–533, 1991.

[6] A. E. Alving, A. J. Smits, and J. H. Watmuff. Turbulent boundary layer relaxation from convex curvature. *J. Fluid Mech.*, 211:529–556, 1990.

[7] E.J. Anderson, W.R. McGillis, and M.A. Grosenbaugh. The boundary layer of swimming fish. *Accepted J. Exp. Bio.*, 2001.

[8] J. Anderson. *Vorticity control for efficient propulsion.* PhD dissertation, Massachusetts Institute of Technology and the Woods Hole Oceanographic Institution, Department of Ocean Engineering, 1996.

[9] J. Anderson, K. Streitlien, D. Barrett, and M. Triantafyllou. Oscillating foils of high propulsive efficiency. *Journal of Fluid Mechanics*, 360:41–72, 1998.

[10] P. Bandyopadhyay and A. Ahmed. Boundary layers subjected to multiple curvatures and pressure gradients. *J. Fluid Mech.*, 24:503, 1993.

[11] D. Barrett. The design of a flexible hull undersea vehicle propelled by an oscillating foil. Master's thesis, Massachusetts Institute of Technology, Department of Ocean Engineering, 1994.

[12] D. Barrett. *Propulsive efficiency of a flexible hull underwater vehicle.* PhD dissertation, Massachusetts Institute of Technology, Department of Ocean Engineering, 1996.

[13] D. Barrett and M. Triantafyllou. The design of a flexible hull undersea vehicle propelled by an oscillating foil. In 9^{th} *International Symposium on Unmanned Untethered Submersible Technology*, 1995.

[14] V. Baskaran, A. J. Smits, and P. N. Joubert. A turbulent flow over a curved hill. part 1. crowth of an internal boundary layer. *J. Fluid Mech.*, 182:47–82, 1987.

[15] V. Baskaran, A. J. Smits, and P. N. Joubert. A turbulent flow over a curved hill. part 2. effects of streamwise curvature and streamwise pressure gradient. *J. Fluid Mech.*, 232:337, 1991.

[16] H. H. Bruun. *Hot-wire Anemometry: Principles and signals analysis.* Clendon, Oxford, 1995.

[17] E. Coustols and A. M. Savill. Turbulent skin friction drag reduction by active and passive means. Technical report, VKI, Brussels, Belgium, 2-6 March 1992.

[18] P. Domenici and R. Blake. Review: The kinematics and performance of fish fast-start swimming. *Journal of Experimental Biology*, 200:1165–1178, 1997.

[19] R. Fairman. Master's thesis, Massachusetts Institute of Technology, Department of Ocean Engineering, Cambridge, MA, 1998.

[20] J. Ffowcs-Williams and B. Zhao. The active control of vortex shedding. *Journal of Fluids and Structures*, 3:115–122, 1989.

[21] M. Gharib, E. Rambod, and K. Shariff. A universal time scale for vortex ring formation. *Journal of Fluid Mechanics*, 360:121–140, 1998.

[22] J. Gillis and J. P. Johnson. Turbulent boundary-layer flow and structure on a convex wall and its redevelopment on a flat wall. *J. Fluid Mech.*, 135:123–153, 1983.

[23] R. Gopalkrishnan, M. Triantafyllou, G. Triantafyllou, and D. Barrett. Active vorticity control in a shear flow using a flapping foil. *Journal of Fluid Mechanics*, 274:1–21, 1994.

[24] H. Gortler. On the three-dimensional instability of laminar boundary layers on concave walls. *Tech. Mem. Nat. Adv. Comm. Aero. Wash.*, 1940.

[25] J. Gray. Studies in animal locomotion: VI. The propulsive powers of the dolphin. *Journal of Experimental Biology*, 13(2):192–199, 1936.

[26] J. Gray. *Animal locomotion.* Weidenfield and Nicolson, London, 1968.

[27] P. H. Hoffmann, K. C. Muck, and P. Bradshaw. The effect of concave surface curvature on turbulent boundary layers. *J. Fluid Mech.*, 161:371–403, 1985.

[28] H. Huang, D. Dabri, and M. Gharib. On errors of digital particle image velocimetry. *Meas. Sci. Technol.*, 8:1427–1440, 1997.

[29] J. M. Kendall. The turbulent boundary layer over a wall with progressive surface waves. *J. Fluid Mech.*, 41(2):259–281, 1970.

[30] R. M. Kirby, T. C. Warburton, S. J. Sherwin, A. Beskok, and G.E. Karniadakis. The nektar code: Dynamic simulations without remeshing. *Proc. Second Intern. Symp. Computational Technologies for Fluid/Thermal/Chemical Systems with Industial Applications ASME*, 1999. August 1-5, Boston.

[31] J.M. Kumph and M.S. Triantafyllou. Fast starting and maneuvering underwater vehicles by robopike and robomuskie. *Proc. 11th Inter. Symp. Unmanned Untethered Submersible Technology (UUST99)*, 1999. August 22-25, Durham, New Hampshire.

[32] G. Lemonis and T. Dracos. Determination of 3-d velocity and vorticity vectors in turbulent flows by multi-hotwire anemometry. *In Three dimensional Velocity and Vorticity Measuring and Image Analysis Techniques*, pages 1–42, 1996.

[33] M. Lighthill. *Mathematical Biofluiddynamics.* Society for Industrial and Applied Mechanics, Philadelphia, Pennsylvania, 1975.

[34] H. Liu, R. Wassenberg, and K. Kawachi. The three-dimensional hydrodynamics of tadpole swimming. *Journal of Experimental Biology*, 200:2807–2819, 1997.

[35] Z.-C. Liu, C. C. Landreth, R. J. Adrian, and T. J. Hanratty. High resolution measurement of turbulent structure in a channel with particle image velocimetry. *Exp. Fluids*, 10(6):301–312, March 1991.

[36] B. Lüthi. Boundary layer investigation of the mit robotuna by means of flow visualization and dptv. Master's thesis, ETH Zurich, 1999.

[37] S. P. McKenna. The influence of surface films on interfacial flow dynamics. Master's thesis, Massachusetts Institute of Technology/Woods Hole Oceanographic Institution, 1998.

[38] S. P. McKenna. *Free-surface turbulence and air-water gas exchange.* PhD thesis, Massachusetts Institute of Technology/Woods Hole Oceanographic Institution, 2000.

[39] S. P. McKenna and W. R. McGillis. Performance of digital image velocimetry processing techniques. *Accepted Exp. in Fluids*, 2001.

[40] K. C. Muck, P. H. Hoffmann, and P. Bradshaw. The effect of convex surface curvature on turbulent boundary layers. *J. Fluid Mech.*, 161:347–369, 1985.

[41] R. J. Adrian R. D. Keane and Y. Zhang. Super-resolution particle imaging velocimetry. *Meas. Sci. Tech.*, 6:754–768, 1995.

[42] D. Rockwell. Vortex-body interactions. *Annual Rev. Fluid Mech.*, 30:199–229, 1998.

[43] M. Rosenfeld, M. Gharib, and E. Rambod. Circular and formation number of laminar vortex rings. *Journal of Fluid Mechanics*, 376:297–318, 1998.

[44] F. Scarano and M. L. Reithmuller. Iterative multigrid approach in piv image processing with discrete window offset. *Exp. Fluids*, 26(6):513–523, 1999.

[45] H. Schlichting. *Boundary Layer Theory.* McGraw-Hill, New York, USA, 1960.

[46] R.M.C. So and G.L. Mellor. Experiment on convex surface curvature effects in turbulent boundary layers. *J. Fluid Mech.*, 60:43, 1973.

[47] S. Taneda. Visual observations of the flow past a circular cylinder performing a rotary oscillation. *Journal of the Physical Society of Japan*, 45:1038–1043, 1978.

[48] S. Taneda and Y. Tomonari. An experiment on the flow around a waving plate. *Journal of the Physical Society of Japan*, 36(6):1683–1689, 1974.

[49] Tennekes and Lumley. *A First Course in Turbulence.* The MIT Press, Cambridge, MA, 1972.

[50] P. Tokumaru and P. Dimotakis. Rotary oscillation control of a cylinder wake. *Journal of Fluid Mechanics*, 224:77–90, 1991.

[51] G. Triantafyllou, M. Triantafyllou, and M. Grosenbaugh. Optimal thrust development in oscillating foils with application to fish propulsion. *Journal of Fluids and Structures*, 7:205–224, 1993.

[52] M. Triantafyllou, D. Barrett, D. Yue, J. Anderson, M. Grosenbaugh, K. Streitlien, and G. Triantafyllou. A new paradigm of propulsion and maneuvering for marine vehicles. *Transactions of the Society of Naval Architects and Marine Engineers*, 104:81–100, 1996.

[53] M. Triantafyllou and G. Triantafyllou. An efficient swimming machine. *Scientific American*, 272(3):64–70, 1995.

[54] M. Triantafyllou, G. Triantafyllou, and R. Gopalkrishnan. Wake mechanics for thrust generation in oscillating foils. *Physics of Fluids A*, 3:2835–2837, 1991.

[55] M. S. Triantafyllou, G. S. Triantafyllou, and D. K. P. Yue. Hydrodynamics of fish-like swimming. *Annual Review of Fluid Mechanics*, 32, 2000.

[56] Y. Tsuji and Y. Morikawa. Turbulent boudnary layer with pressure gradient alternating in sign. *Aero. Q.*, 27:15, 1976.

[57] M. VanDyke. *An Album of Fluid Motion.* Parabolic Press, Stanford, CA, 1982.

[58] J. Videler. *Fish Swimming.* Chapman and Hall, London, U.K., 1993.

[59] D. R. Webster, D. B. DeGraff, and J. K. Eaton. Turbulence characteristics of a boundary layer over a two-dimensional bump. *J. Fluid Mech.*, 320:53–69, 1996.

[60] D. Weihs. A hydrodynamical analysis of fish turning manoeuvres. *Proceedings of the Royal Society of London* **B**, 182:59–72, 1972.

[61] F. M. White. *Viscous Fluid Flow.* McGraw-Hill, New York, USA, 2nd edition, 1991.

[62] C. E. Willert and M. Gharib. Digital particle image velocimetry. *Exps. Fluids*, 10:181–193, 1991.

[63] M. Wolfgang, J. Anderson, M. Grosenbaugh, D. Yue, and M. Triantafyllou. Near-body flow dynamics in swimming fish. *Journal of Experimental Biology*, 1999. *Sub judis.*

[64] M. Wolfgang, S. Tolkoff, A. Techet, D. Barrett, M. Triantafyllou, D. Yue, F. Hover, M. Grosenbaugh, and W. McGillis. Drag reduction and turbulence control in swimming fish-like bodies. In *Proceedings of the International Symposium on Seawater Drag Reduction*, pages 463–469, Newport, RI, July 1998. ONR, NSSC, DARPA, NSWC, ASME, and NUWC.

[65] Xiang Zhang. *I. Surfactant effects on the interaction of a three-dimensional vortex pair with the free surface; II. Turbulent flow over a flexible body undergoing fish-like swimming motion.* PhD thesis, Massachusetts Institute of Technology, 2000.